The Effects of Nitrogen doping on Chemical, Optical and Electronic properties of Carbon Dots

Mostafa Esmaeili

School of Engineering and Built Environment

Queensland Micro- and Nanotechnology Centre

Griffith University

Submitted in fulfilment of the requirements of the degree of

Doctor of Philosophy

October 2021

Statement of Originality

This work has not previously been submitted for a degree or diploma in any university. To the best of my knowledge and belief, the thesis contains no material previously published or written by another person except where due reference is made in the thesis itself.
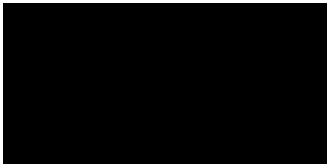
Mostafa Esmaeili

16 October 2021

<u>**The paper included is co-authored**</u>

Acknowledgement of papers included in the thesis

Section 9.1 of the Griffith University Code for the Responsible Conduct of Research ("Criteria for Authorship"), in accordance with Section 5 of the Australian Code for the Responsible Conduct of Research, states:

To be named as an author, a researcher must have made a substantial scholarly contribution to the creative or scholarly work that constitutes the research output, and be able to take public responsibility for at least that part of the work they contributed. Attribution of authorship depends to some extent on the discipline and publisher policies, but in all cases, authorship must be based on substantial contributions in a combination of one or more of:

- conception and design of the research project

- analysis and interpretation of research data

- drafting or making significant parts of the creative or scholarly work or critically revising it so as to contribute significantly to the final output.

Section 9.3 of the Griffith University Code ("Responsibilities of Researchers"), in accordance with Section 5 of the Australian Code, states:

Researchers are expected to:

- Offer authorship to all people, including research trainees, who meet the criteria for authorship listed above, but only those people.

- accept or decline offers of authorship promptly in writing.

- Include in the list of authors only those who have accepted authorship

- Appoint one author to be the executive author to record authorship and manage correspondence about the work with the publisher and other interested parties.

- Acknowledge all those who have contributed to the research, facilities or materials but who do not qualify as authors, such as research assistants, technical staff, and advisors on cultural or community knowledge. Obtain written consent to name individuals.

- Included in this thesis is a paper in *Chapters Four, Five, and Six* which are co-authored with other researchers. The bibliographic details for these papers including all authors, are:

- Zhiqing Wu

- Amandeep Singh

- Prashant Sonar

- Dechao Chen

- David Thiel

- Qin Li

Acknowledgements

Table of Contents

List of figures

List of abbreviations

CA	citric acid
CD	carbon dots
CND	carbon nanodots
CQD	carbon quantum dots
EDA	ethylenediamine
FET	field effect transistor
FTIR	Fourier transform infrared
GCD	graphitic carbon dots
GQD	graphitic carbon dots
HCN	hydrogen cyanide
HOMO	highest occupied molecular orbital
LED	light emitting diode
LUMO	lowest unoccupied molecular orbital
NIR	near infrared
PV	photovoltaic
rGO	reduced graphene oxide
TEM	transmission electron micrsocope
TCSPS	time correlated single photon counting
UV	ultraviolet
VOC	volatile organic compound
XPS	X-ray photoelectron
ZCIS	zin copper indium sulphide

Abstract

Photoluminescent carbon dots have received significant research interest in recent years owing to their extraordinary optical properties, biocompatibility, and versatile functionalities. Nitrogen-doping is a widely used strategy for enhancing the photo-electronic functionalities of carbon dots. However, there is a lack of systematic study on the composition and concentration-dependency emission behaviour of N-doped carbon dots in the literature. In this study, multicolour carbon dots (CDs) having different degree of nitrogen doping were synthesized by varying the molar ratio of citric acid to urea in the precursor via hydrothermal treatment. The effects of nitrogen doping on chemical, optical, and electronic properties of CDs were characterized using various techniques including transmission electron microscopy (TEM), X-ray photoelectron spectroscopy (XPS), Fourier-transform infrared (FTIR); fluorescence and absorption spectroscopy; fluorescence lifetime and Hall effect measurements. Three main emissive centres were recognized in concentration-dependent fluorescence study of N-CDs which can be ascribed to molecular type of fluorescence, core emission, and mid-gap nitrogen states on the edge/surface of CDs. A plausible mechanism in relation to the obtained results is proposed. This work provides insights on the opto-electro-tunability of CDs via N-doping.

Chapter 1 Introduction

1. 1. Motivation

To fabricate portable, wearable, and printable electronic devices on flexible large area substrates for real-world applications, inexpensive and solution-processable materials are on demand. Inorganic nanocrystals, aptly named quantum dots for their quantum size effect, are currently in the centre of researchers' attention because they offer many advantageous properties to serve this purpose. However, the synthesis of semiconductor QDs is time-consuming and relies on heavy toxic metals necessitating a sustainable replacement. Carbon-based fluorescent nanoparticles namely carbon dots, graphene quantum dots show similarity with QDs in terms of optical properties. The green nature, easy accessibility, cost-effectiveness, and photoluminescence of C-dots are the properties that makes them a promising candidate to substitute the role of QDs.

1. 2. Research objectives

The primary objective of this research plan was to address the question of whether CDs are capable of functioning the role of cutting-edge QDs in electronic and optoelectronic devices. However, the tortuous path of this journey took us to perform a systematic study on the effects of nitrogen doping on properties of carbon dots. Herein, we studied how the increase of nitrogen doping can change chemical composition, optical characteristics, and electronic properties in CDs. The obtained information from the characterization of N-CDs in this thesis can shed a ray of light on practicality of these materials to substitute the role of QDs in real-world applications, especially that we attempted to address the controversy over the fluorescence origin in CDs [1-3].

1. 3. Significance of research

In semiconductor quantum dots, the wavelength of fluorescence emission can be tuned by the size of nanocrystals which has significant applications in bioimaging, light-emitting diodes, photovoltaic and many other electronic devices [4-6]. However, QDs generally contain heavy metals, and some of these metals are rare and have limited resources. Alternatively, carbon dots are carbogenic nanoparticles typically smaller than 50 nm. As a new member of luminescent nanomaterials, CDs can offer various advantages compared to inorganic quantum dots including environment-friendliness, low cost, surface functional tuneability and scalable production [7-9]. Although size-controllable synthesis of CDs is not as straightforward as that of QDs, there are various ways to tune their chemical, optical and electronic properties namely surface functionality, heteroatom doping or even aggregation [10, 11].

Heteroatom doping is a powerful approach for tailoring the intrinsic properties of CDs such as surface structure and electron distribution. However, heteroatom doping may not be a feasible approach unless the incorporation of dopant into carbon lattice is energetically favourable. Due to the high dissociation energy of covalent C–C bonds, successful heteroatom doping has been realized with only a few elements such as less nitrogen and sulphur [12]. Among various metallic and non-metallic heteroatoms, nitrogen is the most favourable and attractive choice of dopant for researchers of CDs. High electronegativity, size compatibility, availability of five electrons in the valence band of nitrogen, in addition to the facile nature of doping this element into carbon are some of the major reasons behind the extensive number of reports on nitrogen doped CDs [13, 14]. Nitrogen can serve as n-type impurity endowing carbon with excess electrons shifting the Fermi level, which may result in modified emission of CDs [15]. Interestingly, redshifts in the emission of CDs due to the increase of nitrogen content

is observed in a few studies [16, 17]. Moreover, nitrogen may not only passivate the surface of CDs causing suppression of non-radiative recombination but also creates trap states which enhances the probability of emissive electronic transitions that finally leads to improvement of quantum yield [13].

The electronic properties of the CDs thin films are less explored in comparison to their optical properties. The generation of a voltage difference across an electrical conductor under the application of a magnetic field perpendicular to the flowing current is called Hall effect. Combined Hall and longitudinal resistance measurements can determine carrier mobility, carrier concentration, conductivity type and resistivity [18]. Though initially developed for bulk material characterisation, Hall measurement can still be employed to study intrinsic electronic properties of novel nanomaterials. For instance, the occurrence of Hall effect in QDs is indicative of band-gap like charge transport similar to conventional semiconductors [19]. Nevertheless, only a few studies on novel nanomaterials have tapped into Hall measurements to investigate their electronic properties [20, 21]. Our recent study has found that hair-derived N-CDs not only form a highly effective emissive layer in the organic light emitting diode, but also function as the hole-transporting material [20].

This study is aimed to provide a systematic investigation on the effects of nitrogen doping on the optical and electronic properties of CDs. We employed a simple N-doping method of CDs by hydrothermal treatment of citric acid and urea with systematically varied molar ratios. Physiochemical structures, photoluminescence and electronic properties of the resultant N-CDs were investigated.

Chapter 2 Literature review

2. 1. Literature review on concentration dependent emission of carbon dots

Varying reaction conditions in chemical synthesis of CDs is proved to be efficient in control of size, carbonization degree and surface functional groups of the final products and, accordingly their optical characteristics. Changing the pH value [22], the type of solvent [23], the ratio of the constituents of precursors and reaction temperature [24] in chemical synthesis of CDs have been attempted as the tuning factors to work out multi-colour emission. Gel electrophoresis [25], ultrafiltration [26] and column chromatography [27] are the post-synthesis approaches that have been employed to separate CDs of different colours.

The odd one out of the approaches for multi-colour CDs is exploiting the readily available control of concentration to tune the fluorescence emission. A few research groups have undertaken studies on this enlightening prospect to fundamentally explain the concentration dependency of fluorescence in CDs. Mu et al. suggested that aggregation of CDs in high concentration results in formation of clusters that facilitate energy transfer between emitting centres, which redshifts the emission [28]. Chen et al. introduced the inner filter effect responsible for the *pseudo-multicolour emission* in CDs as this effect may quench the fluorescence of the blue-region in high concentrated suspensions [29]. Meng et al. upheld the notion that the presence of different kinds of surface energy traps that capture electrons from excited states is the reason for excitation dependent fluorescence in CDs [30]. Moreover, they discussed that the decrease of inter-particle distance when increasing the concentration can reduce the surface electric potential, the driving force to transfer excited electrons to

the surface, which finally leads to the opening of alternative long wavelength recombination routes from structural defects (Figure 2.1).
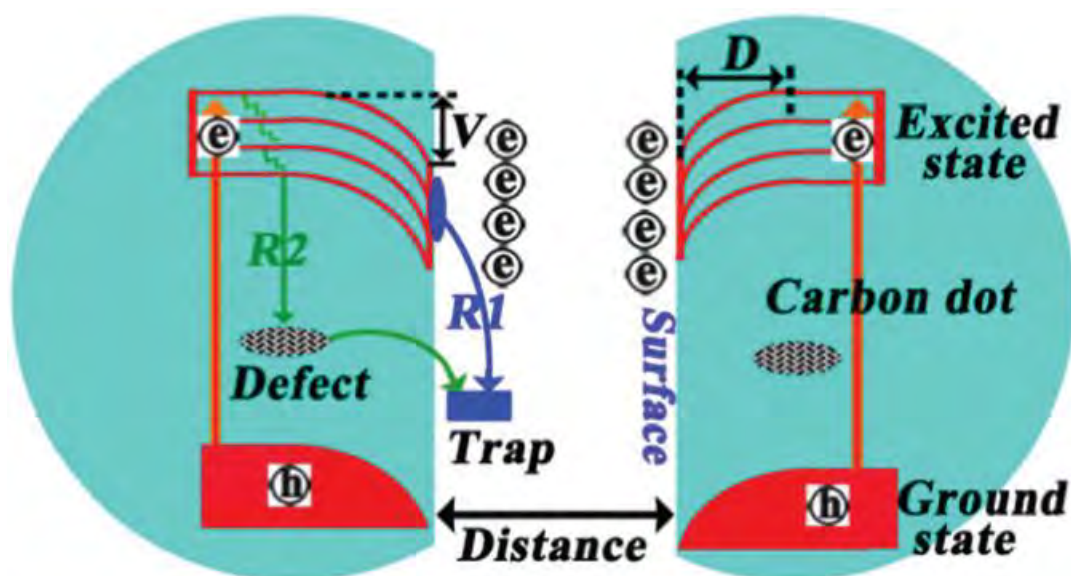
Figure 2.1. Proposed photoluminescence mechanism of CDs tuned by concentration. Reprinted with permission from reference [30].

Wang et al. concluded from their experiments that size distribution and composition of chemical groups on the surface of N-CDs do not play considerable roles in concentration dependency emission [31]. Instead, they argued that self-absorption was accountable for the tendency of CDs to redshift and decrease in fluorescence at high concentrations. In Chen and co-workers' study of concentration induced multi-colour N-CDs, triple fluorescence centres originated from core, edge and N surface states were recognized as the blue, green and orange emitters [32]. They proposed that after dilution of CDs in DMF, hydrogen bonding effect can polarize the crystalline field of CDs changing the core and surface electronic structure, which finally causes a blue shift of the orange fluorescence centre. Adequate addition of DMF subsides the non-radiative relaxation from higher energy states to N surface states resulting in migration of fluorescence from the orange centre to the blue one. Moreover, non-radiative cross-relaxation between fluorescence centres at high concentration were

thought as the cause of lower photoluminescence intensity in the longer wavelengths. Figure 2.2 illustrates the fluorescence mechanism proposed in their work.
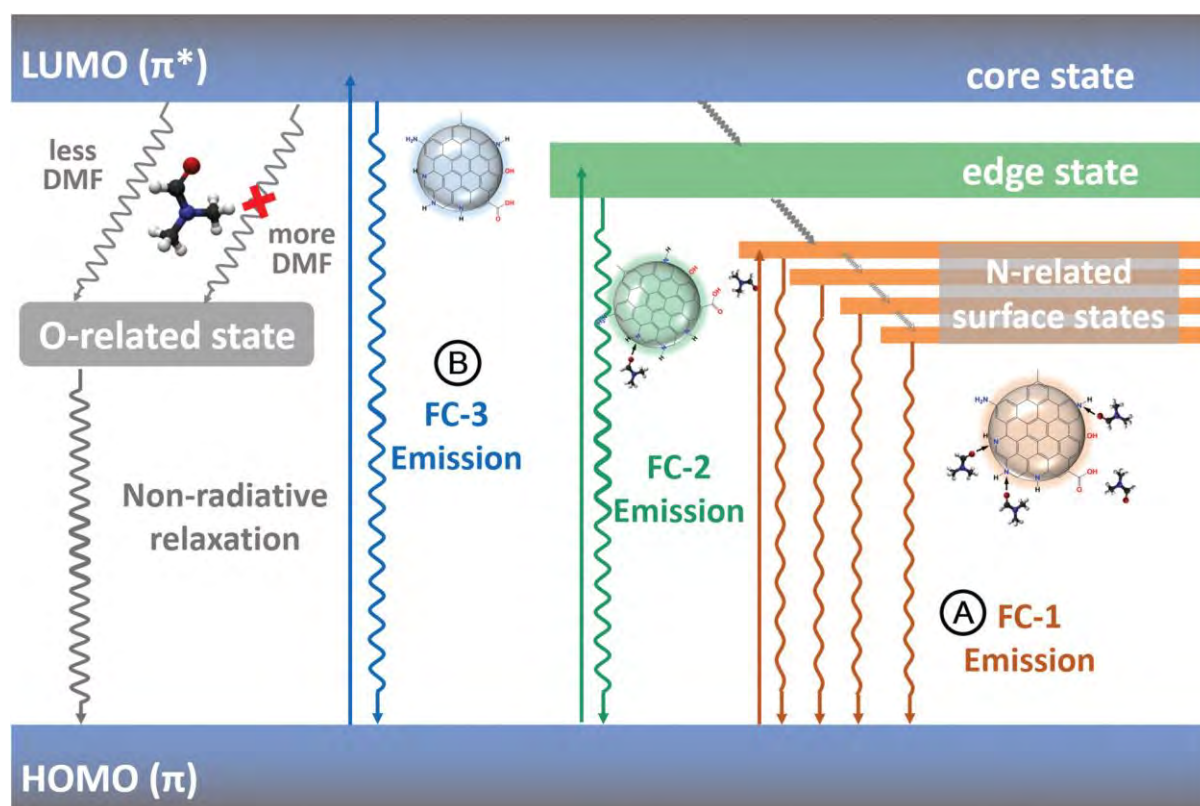
Figure 2.2. The Proposed photoluminescence mechanism for the three fluorescent canters of carbon dots. Reprinted with permission from reference [32].

Wang et al. performed time-correlated single photon counting measurements on CDs of varied concentrations [33]. The results showed that with increasing the concentration of CDs, the share of fluorescence lifetime which belongs to surface states, shortens at first and then lengthens; with the initial increase of the concentration more functional groups interact with each other and new energy levels appear, with further increase non-radiative relaxation are more probable to occur. The redshift was attributed to the transfer of energy from smaller particles to larger ones in formation of aggregates when concentration increases. The results from Su and co-workers' comparative study between CDs and Zirconium doped CDs of varied concentrations showed that with increasing the concentration, the emission of CDs

redshifts and their bandgap decreases, whereas the existence of Zirconium complex on the surface of Zr-CDs prevents CDs from aggregation from a certain point, keeps the bandgap constant and suppresses the redshift [34]. Thus, aggregation was recognized as the facilitator for energy transfer between CDs which induces multi-colour emission. In the very recent comprehensive study of Lai and co-workers on concentration- and excitation dependency of GQDs, several fluorescence centres were specified and attributed to their corresponding types of electronic transition [35]. The conclusion of this scheme of research introduced self-aggregation and competition between the fluorescence centres as the underlying mechanisms for multi-colour emission in GQDs.

2. 2. Literature review on application of carbon dots in device fabrication

Since the serendipitous discovery of CDs in 2004 [36], more than 3500 publications have emerged discussing their synthetic development and widespread utilization [37]. The synthetic approaches for the formation of CDs are generally categorized into two divisions: top-down and bottom-up approaches. The former method includes arc-discharge [36], laser ablation [38], and electrochemical routes [39] through them macroscale carbon sources are cleaved into tiny particles, resulting in CDs. The latter approach consists of thermal [40], hydrothermal [41], and microwave assisted [42] routes through them the CDs assembled from molecular precursors.

Sun and co-workers reported that laser-ablated, acid-oxidized CDs functionalized with PEG_{1500N} shows bandgap like electronic transitions typically found in semiconductor QDs [43]. Some other reports have confirmed that such bandgap like transition exists and can be tuned by controlling the carbon core size [11, 26, 44] or surface functionality of CDs [11, 26, 45, 46]. Theoretical studies of electronic structure and

bandgap tunability of GQDs corroborates that these properties can be modified by altering their size and surface functionalities [47-49].

There exists an arbitrary nomenclature of classification for CDs in the literature. To avoid confusion, let us introduce the terminology proposed by Cayuela and co-workers in their featured article [50]. They suggested that only the three names of graphene quantum dots, carbon quantum dots, and carbon nanodots are appropriate for naming these materials. The presence or absence of quantum confinement and the crystallinity of the carbon core determines how to categorize them. Therefore, a nano-sized carbonaceous particle with an amorphous core that does not show quantum confinement is a carbon nanodot (CND). Alternatively, a particle with crystalline, graphitic like carbon core that exhibits quantum confinement can be classified as carbon quantum dot (CQD) or graphene quantum dot (GQD). To draw a distinction between these two, quasi-spherical nanoparticles being comprised of multiple layers of graphitic sheets are CQDs, whereas GQDs consist of only a single layer of nano-sized graphene. Figure illustrates the structure of semiconductor quantum dots (SQDs), GQDs, CQDs and CNDs (Figure 2.3). For the sake of simplicity, CNDs and CQDs are specified as carbon dots (CDs) in this literature review, especially that recognition of such distinction between the two based on the information provided in the cited references is not practical.

Not only CDs benefit from major advantageous characteristics of QDs such as bright photoluminescence and good photostability, they are heavy metal free and readily water-soluble [43]. Thanks to these alluring properties, they are considered as auspicious candidate to replace the role of QDs in electronic and optoelectronic devices. This review is intended to encompass the role of CDs in device fabrication,

and it does not include other areas of applicability such as bio-imaging, drug delivery, chemical sensing, and photo-catalysis.
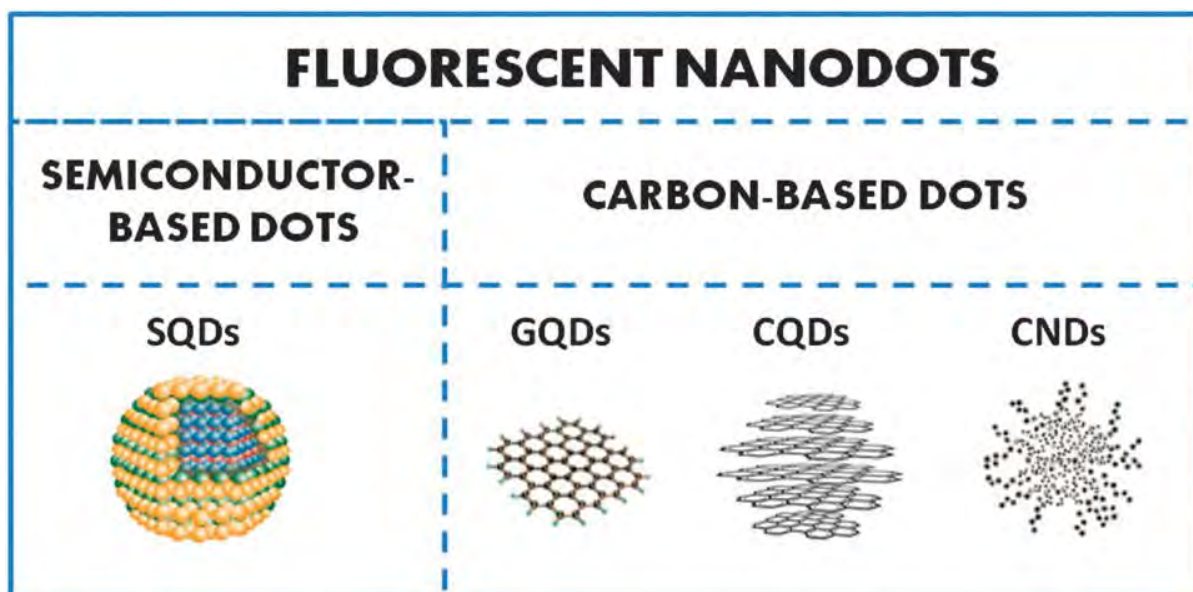
Figure 2.3. Configuration of semiconductor and carbon-based fluorescent nanodots. Reprinted with permission from reference [50].

2. 2. 1. Photovoltaic devices

The optical absorption of carbon dots largely overlaps with much of the visible light spectrum, making them a conceivable sensitizer in dye-sensitized solar cells [51, 52]. Besides, owing to the large π electron network within crystalline CQD/GQD, they can function as electron acceptors/donors, conducting media for electron transfer, or heterojunction forming charge dissociation sites.

2. 2. 1. 1. Sensitized metal-oxide based photovoltaic devices

In the cutting-edge dye-sensitized solar cells, Ru-metals are employed as the centre of sensitizer presenting good performance, but they are scarce, costly and time consuming to synthesize [53]. Intriguing optical properties of CDs present them as a good candidate to replace Ru-based dyes. However, appropriate band alignment is a necessity to ensure that charge carriers flow in the desired direction within the device

architecture. Many research groups have reported an appropriate band alignment [54-56] and efficient charge separation/electron injection [26, 57] for CDs and GQDs within a variety of photovoltaic device architectures.

A generic device architecture of dye-sensitized solar cells consists of five components: (1) a mechanical support coated with transparent conductive oxides; (2) the semiconductor film, usually TiO_2; (3) a sensitizer adsorbed onto the surface of the semiconductor; (4) an electrolyte containing a redox mediator; (5) a counter electrode capable of regenerating the redox mediator like platinum [58]. The working mechanism can be briefly discussed as follows. The absorption of photons excites the sensitizer leading to the injection of electrons to the conduction band of the semiconductor. Then, the injected electrodes are transported through semiconductor until they reach the counter electrode. Finally, the oxidized sensitizer accepts electrons from the electrolyte leading to regeneration of the ground states.

Mirtchev et al. reported one of the first applications of CDs as sensitizer in a TiO_2 based solar cell [59]. The solution-phase synthesis of their CDs allows them to be functionalized to TiO_2 photoanode through carboxyl groups. The authors attributed the low short circuit current density of their device to 1) emissive trap states on the surface of CDs, which may act as recombination centres for photogenerated charges, 2) inferior charge transport properties of CDs. In another effort to explore CDs as the green material for the role of sensitizer in dye-sensitized solar cells, Wang and co-workers synthesized N-doped CDs through pyrolysis of citric acid and ammonia [17]. They achieved power conversion efficiency of 0.79% by adjusting the extent of N-doping by controlling mass ratio of the precursor. Power conversion efficiency of a photovoltaic device is the percentage of the solar energy shining on a PV device that is converted into usable electricity. Evidenced by greater characteristics of the device,

the N-doping has introduced new energy levels and trap states, leading to extension of the absorption tail and subsequent injection of photoexcited electron into TiO_2.

Li et al. synthesized nitrogen-enriched CDs of 1 to 3 nm in a one-pot reaction between melamine and glycerol. The CDs were used as the sensitizer in a dye-sensitized solar cell and showed the capability to convert near infrared photon energy into electric current. This capability of the dots was attributed to charge transfer induced by two-photon excitations and upconversion fluorescence. Zhao and co-workers also reported on utilization of N-doped CDs as the sensitizer in a dye-sensitized solar cell configuration with aqueous I^-/I^{-3} electrolyte. The I^-/I^{-3} blocks the recombination of photogenerated carriers by quenching CDs fluorescence in addition to the conventional role of redox mediator. The low power conversion efficiency was attributed to the low quantum yield of photoexcited electrons [60]. Fang et al. synthesized acid oxidized, PEG passivated GQDs and employed them as co-sensitizer in conjunction with N179 [61]. Their results demonstrated that with the introduction of the optimum concentration of GQDs, not only they act as the sensitizer, injecting hot electrons into TiO_2 but also considerably influence the dye uptake by TiO_2, resulting in improved performance of the device.

Extraction of hot carriers before they lose enough energy to cool to the band edge is a common phenomenon in quantum dot devices. When the absorbed radiation within the quantum dot is in excess of the bandgap, it creates highly excited states for the transport of hot carriers. If these electrons are not extracted rapidly and effectively, the absorbed energy will be released within phononic processes, resulting in lower device efficiency compared to its theoretically anticipated performance. According to Mueller and co-workers, GQDs benefit from features that could reduce the hot carrier relaxation rate [62]. Yu et al. reported fast electron transfer from CDs to graphene

oxide with a time constant of 400 fs, introducing CDs-GO nanocomposite as a promising candidate for hot carrier solar cells [63]. Aiming to exceed the theoretical maximum power conversion efficiency of solar cells by harvesting quasi-equilibrium hot carriers, Williams and co-workers probed hot electron injection and charge recombination dynamics for GQDs anchored to the TiO_2 surface [64]. They observed ultrafast injection from photoexcited GQDs to the TiO_2 conduction band.

A thin film of platinum deposited onto a transparent conductive oxide coated glass substrate is the most common configuration for a counter electrode in dye-sensitized solar cells. Although Pt yields some of the finest photovoltaic performances owing to its high catalytic activity, it is the most expensive component of dye-sensitized solar cells, calling for an economical substitute. Recently, some efforts have been made to replace Pt thin film with conductive polymers. However, they suffer from relatively high charge transfer resistance, restricting their real-world applications. Doping the conductive polymer with a more conductive material can improve charge transfer, as recently shown by Chen and co-workers [65]. They synthesized GQDs from carbon black via chemical oxidation and then added them to pyrrole solution in various mass ratios. The solutions were electrochemically deposited on fluorine-doped tin oxide glasses to produce GQD doped PPy film. Increasing the GQD doping up to 10% enhances all the performance characteristics of the device, while further increase of the dopants would affect the polymerization process resulting in decrease of the reactive sites at the counter electrode and higher charge recombination at the photoelectrode. The enhanced performance of the device is attributed to the higher porosity of the film as the more porous counter electrode increases the number of active centres and facilitates the diffusion of reactants for better electrode kinetics. This porosity, described as nano-island by the authors, is formed due to the

interactions between negatively charged GQD and positively charged N group on the pyrrole.

2. 2. 1 .2. Bulk heterojunction organic photovoltaics

Thanks to the exciting properties of bulk heterojunction organic photovoltaic devices; flexibility, low-cost, large-scale mass production through roll-to-roll printing, they have shown promise for the next generation of photovoltaics. These devices conventionally consist of a bulk heterojunction film with the layers of electron donating material, typically P-type conjugated polymers such as P3HT, and electron accepting material, typically N-type fullerene derivatives such as PCBM.

Because charge carriers have diffusion lengths of a few nanometres in a typical organic semiconductor, the thickness of these devices is limited, resulting in inadequate light harvesting and low power conversion efficiency. Incorporation of semiconductor QDs as the electron accepting materials within organic layer matrices is a recent approach to overcome these issues, but due to the lower abundance and toxicity of QDs, all other prospects should be considered. Alternatively, CDs benefit from analogous physical and electronic properties, while possessing narrow size distributions and functional groups nominates them as a promising green candidate for substitution of QDs in such devices. Incorporation of CDs into the photoactive, hole extraction and buffer layers of PV devices has already shown performance enhancement.

While most reports in the context of bulk heterojunction photovoltaic applications describe CDs having electron accepting nature [66-68], few studies emphasize on their electron donating capability [69]. Their role as electron acceptors can be divided into two subcategories; one in which CDs are blended into the active layer of the device, the other they fully replace the fullerene derivative layer.

Experimental and theoretical results from Feng et al. underlines the applicability of their low temperature hydrothermally synthesized CDs passivated with ethylenediamine as an electron acceptor material within bulk heterojunction device [70]. They showed that the bandgap energies of CDs allow for efficient charge transfer at the P3HT-CD interface and that the HOMO and LUMO of P3HT are larger than the binding energy of an exciton, which is required for the generation of electron-holes at the interface. Privitera and co-workers showed that N-doped CDs functionalized with thiophene-containing groups act as electron donors to PCBM in both solution and solid blends [69]. Contrarily, Kim et al. reported on electron accepting properties of GQDs in their fabricated photovoltaic device.

Wang et al. reported that the insertion of the optimum ratio of GQDs into the active layer of their device architecture results in several positive effects [71]. The occurrence of longer optical path length, which is due to light scattering with GQDs, improves light absorption and charge conductance of GQDs reduces the charge transport resistance. The combination of these factors improves the characteristics of the device. Utilizing a one-step pyrolysis approach, Moon and co-workers synthesized N-doped graphitic carbon dots (N-GCDs) with fumanitrile precursor [72]. To demonstrate the electro-optical behaviour of N-GCDs, they fabricated an inverted type of polymer solar cell. The authors attributed the improvement of power conversion efficiency to increased light absorption in the photoactive layer and enhanced electron transport due to the presence of N-GCDs.

GQDs have shown the potential to fully replace the fullerene derivative typically employed in bulk heterojunction device architecture in a handful of reports. Huang et al. synthesized organo-soluble GQDs via a microwave-assisted pyrolysis approach and consolidated them as a thin film beneath the P3HT layer to fabricate a conceptual

PV device [66]. They proved the concept that GQDs in the structure of ITO/GQD/P3HT function as electron donors, which is of great significance because these materials are much more cost-effective and manufacturable than fullerene derivatives. However, their device exhibited threefold lower photocurrent, which could be enhanced by further optimization.

A layer for extraction of holes is usually employed within the architecture of bulk heterojunction devices to facilitate charge separation and prevent interfacial recombination. PEDTO:PSS is the most commonly used hole extraction layer, but they suffer from strong acidity and hygroscopicity [73, 74]. The use of inorganic semiconductors as the hole extraction layer would enhance power conversion efficiency without having deteriorating effects on stability of the device, but this approach increases manufacturing cost as they need to be vacuum deposited. Carbon nanomaterials can act as the hole extraction layer as they address both these issues. Lim and co-workers incorporated GQDs prepared from oxidation of carbon nanofibers into PEDOT:PSS film [75]. With the addition of isopropyl alcohol during the organogel formation process, electrostatic interactions between PEDOT:PSS ions are disrupted, resulting in GQD@PEDOT. Since the unsatisfactory electrical properties of neat PEDOT:PSS arises from the insulating nature of PSS counterion chains, the formation of GQD@PEDOT core-shell structure in the film morphology leads to better charge hopping pathways and therefore enhanced electrical conductivity.

Full replacement of the PEDOT:PSS hole extraction layer with GQDs has been reported in a few publications. Wan, Chen and co-workers proved this concept by substitution of acid oxidized, carbon nanofiber synthesized GQDs for the hole extraction layer in both polymer solar cells and small-molecule solar cells [74]. In both

cases, thickness optimization of the GQD film resulted in similar photovoltaic parameters in comparison with the PEDOT:PSS based devices.

Inverted polymer solar cells are another architectural type of bulk hetero junction devices. The bias across these devices is reversed, and the charges are extracted in the opposite direction. Typically, a buffer layer, sometimes called electron transport layer, is embedded between the cathode and the polymer film in order to reduce the cathode work function and sustain separation and extraction of charge carriers. The conventional composition of buffer layers are metal oxides such as ZnO or TiO_2, but Cs_2CO_3 has recently drawn attention owing to good electron injection and simplicity in fabrication. However, weak hole blocking and diffusion of Cs^+ ions into the polymer layer led to a higher rate of charge recombination and device instability, respectively. Impregnation of the buffer layer with GQDs may offer solutions to both these issues. Yang et al. employed hydrothermally synthesized GQDs as an additive to the cathode buffer layer in an inverted polymer solar cell [76]. Due to energy level matches between GQD-Cs_2CO_3 buffer and PCBM, the buffer exhibited good hole blocking and electron transfer capabilities, leading to enhancement of all photovoltaic parameters. Qin et al. incorporated GQDs as the buffer layer between TiO_2 and P3HT to form a cascade energy level architecture [77]. The addition of GQDs provided better channels for charge carrier transport and hindered unfavourable recombinations, which finally led to a considerable enhancement of power conversion efficiency.

2. 2. 1. 3. Solid state solar cells

Although solid state solar cells offer nonpareil photovoltaic performances compared to other device architectures, they suffer from high cost to power ratio and use of environmentally hazardous materials. However, their outstanding stability and unrivalled reliability attracted many researchers to look for inexpensive environment-

friendly materials such as CDs to replace the toxic elements. A handful of reports have explored CDs properties to serve as light absorber, charge transfer media, and energy down-shifting layers in solid state solar cells.

CDs have shown the potential to be employed as the sensitizer in solid state devices, likewise, metal oxide devices. Duttal and co-workers impregnated a vertical array of ZnO nanowire network with hydrazine reduced, GO derived GQDs as the sensitizer to fabricate a solid state solar cell [78]. A comparison between photoluminescence spectra of GQD, ZnO and ZnO Nanowires-GQDs showed broad photoluminescence emission of GQDs, whereas the emission of combined ZnO Nanowires-GQDs was fully quenched, indicating the establishment of new pathways through which more interfacial charge separation occurs. IV characterization confirmed improved photovoltaic performances of GQD-ZnO device compared with ZnO control. Briscoe et al. solvothermally synthesized three types of CDs and utilized them as the sensitizer for ZnO-nanorod-based solid state solar cells [79]. In all cases, the photovoltaic performances were enhanced when compared to the uncoated device. However, the inadequate correlation between light absorption and current density implies that the resultant photocurrent is determined more by the structural nature of the CD coated layer than light absorption characteristics of CDs.

CDs and GQDs have also been applied as efficient charge carrier separation and blocking layer within various solid state solar cells device architectures. Gao et al. hydrothermally synthesized GQDs from pre-oxidized graphene sheets and deposited them between Si and Au layers, of a typical architecture of solid state silicon solar cells [80]. The GQD layer functions as the charge separator by suppressing anodic carrier recombination. Their results showed drastic improvement of all photovoltaic parameters in GQD incorporated devices compared to the control device. These

improvements were attributed to appropriate band alignment of GQDs with Si lowering interfacial recombination, and built-in electric field at the Si/GQD heterojunction separating charge carriers efficiently.

Xie and co-workers fabricated a silicon nanowire array@CDs core_shell heterojunction photovoltaic device [81]. With optimization of the heterojunction, two beneficial effects were derived: efficient suppression of recombination activities due to more appropriate band alignment, and improved absorption in the near-UV light region, which overall leads to enhanced performance of the device.

Conventional silicon solar cells convert only photons with energy close to the silicon bandgap because of the mismatch between the incident solar spectrum and spectral absorption properties of the material. On the one hand, photons with energy smaller than bandgap are not absorbed. On the other hand, the energy of the photons larger than the bandgap is not converted effectively due to electron thermalization. Implementation of an energy down-shifting layer within the structure of silicon solar cells assists in down-converting higher energy photons (e.g. UV) to obtain higher power conversion efficiency. Lee et al. synthesized GQDs through acidic, ultrasonic treatment of GO and deposited them onto silicon solar cells via kinetic spraying [82]. All performance parameters of their device were improved by optimizing the thickness of the layer. These improvements can be explained by strong UV absorption and subsequent visible fluorescence of GQDs, which leads to extra photon absorption closer to the bandgap of silicon. Shen and co-workers arrived at the same conclusion in their work [83]. They hydrothermally synthesized CDs and mixed them with PVA solution, and in the next step, the obtained solution was spin-coated onto Si nanowire array that had been etched onto one side of a silicon wafer. Pelayo et al. electrochemically synthesized CDs, dispersed them in PMMA matrix, and applied the

matrix on commercially available silicon solar cells [84]. Depending on the applied current for the synthesis of CDs, the down-shifting effect increased 2-5% enhancement in power conversion efficiency compared to devices without an energy down-shifting layer.

High power conversion efficiency of the recently emerged perovskite sensitizer based solar cells have drawn significant attention within a broad range of configurations. Nevertheless, charges injection times in perovskite have been measured to be several orders of magnitude longer than hot carrier cooling, meaning that the energy of large amounts of photons are lost to thermalization or carrier trapping. To obviate this, a few groups have employed CDs as electron/hole extraction layers, facilitating charge transport. Zhu et al. sandwiched an ultrathin layer of electrochemically synthesized GQDs between perovskite sensitizer and TiO_2 nanoparticles as a fast electron tunnel to enhance charge transport [85]. The introduction of GQDs significantly enhanced power conversion efficiency that can be attributed to two possible reasons; GQDs may function as electron acceptors, extracting charge carriers, or they may act as a bridge enhancing the charge injection from the perovskite to TiO_2 without capturing the flowing charges. Contrarily, Paulo and co-workers proved the concept that CDs could act as a hole extraction layer within a perovskite sensitized solar cell [86]. However, the incorporation of CDs led to an increase in power conversion efficiency.

2. 2. 2. Field effect transistors

Soon after the discovery of the quantum size effect in quantum dot semiconductors [87], they were used for optoelectronic applications. Size tuneable bandgap, small exciton binding energy and high photoluminescence quantum yields are of the advantages that QD offers for optoelectronic devices such as solar cells and light emitting diodes [88, 89]. However, measurements on QD film in field effect transistors

have shown that their charge transport properties lag behind silicon technology or even organic FETs.

Unlike band-like transport we see in crystalline inorganic semiconductors such as silicon, charges transport in a localized manner in QD films due to scattering by phonons or impurities. Long chain ligands on the surface impede inter-dot coupling, resulting in moving of charge carriers by tunnelling or thermally assisted hopping between QDs. Therefore, the field effect mobility of QD films is affected by the inter-dot distance, temperature and distribution of trap states [88]. Characterization of FETs with different QD materials has demonstrated that the electrical conductivity of untreated QD films is extremely low. This low conductivity is mainly attributed to two factors: 1. long-chain dielectrically isolating molecules used for the synthesis of QDs that increase the inter-dot spacing 2. dangling bonds of unpassivated surface atoms, which trap charge carriers in mid-gap states, hampering their smooth transport [90-92]. Annealing, ligand exchange and chemical doping have been proved as the effective strategies to improve charge transport in quantum dots [88].

The mobility improvement strategies for QDs may also be applicable for CDs to enhance their charge transport properties. Rhee and co-workers' study on mobilities of ligand exchanged CDs is the only report in this vast literature to prove this concept [93]. In their work, hexamethylenediamine-capped CDs were synthesized through a micelle assisted route, and then the ligands on the CDs were exchanged with a few amine ligands of various lengths. The electron and hole mobility measurements of ligand exchanged CDs on FET platforms demonstrated that the carrier mobility increases exponentially with the decrease of ligand length. This notion was previously introduced in experimental studies of charge transport in inorganic nanocrystals [88]. The ambipolar transport of CDs FETs was revealed by changing their gate voltage

with electron mobilities 2-4 times larger than the hole mobilities. This was attributed to higher density of states for electrons.

Zhu and co-workers fabricated a composite film of GQDs and ZnO on a bottom-gate FET platform of heavily P-type Si substrate, ZrO_x dielectric, Al contacts, via magnetron sputtering [94]. To understand the effects of GQDs on the electrical properties of the ZnO thin film, a pure ZnO thin film transistor was also fabricated. The ZnO incorporated GQDs transistor exhibited higher mobility and lower threshold voltage compared to the bare ZnO one. The authors attributed this enhanced performance to better crystallinity of GQD-ZnO composite film, which leads to less grain boundary scattering when charge carriers transport.

Park et al. demonstrated that field-induced charge trapping and exciton dissociation occurs at pentacene/GQDs interface using bottom-gate FETs [95]. Sweeping the gate voltage of pentacene and pentacene/GQD FETs in the dark, a strong hysteresis for the bilayer channel was observed, that indicates carrier trapping in GQD layer. Upon illumination in the forward scan, more electrons are available to transfer to GQDs due to the generation of photoelectrons in pentacene film leading to significant increase of threshold voltage. Such characteristics can be potentially employed for photoelectric memories. Tada et al. fabricated an organic thin film transistor memory with CDs incorporated into a pentacene/oxide interface by means of focused ion beam-chemical vapour deposition technique [96]. The role of CDs in this configuration is to trap charge carriers to generate memory effect. Seo and co-workers fabricated a memory thin film transistor on a flexible substrate using reduced graphene oxide quantum dots as the active layer [97].

2. 2. 3. Light emitting diodes

The potential applications of light emitting diodes in full colour displays and next generation of lighting sources have brought them into the limelight of researchers. The emerging quantum sized CDs seem to be an interesting alternative to replace the rare-earth expensive phosphors and toxic metal-based semiconductor QDs in LEDs due to their tuneable fluorescence emission, low cost, and non-toxicity.

Based on the excitation type of CDs, their application in LEDs can be divided into two categories; one is the optical excitation which is typically used for conversion of blue light into a wider spectrum, the other is direct electrical excitation, typically utilized the emission layer.

2. 2. 3. 1. LEDs based on the electroluminescence of carbon dots

Gupta and co-workers were the first group to demonstrate the applicability of CDs as the electrically driven emission layer in LEDs [98]. Different weight ratios of methylene blue functionalized GQDs blended with MEH-PPV were employed as the active emission layer, and further tests were performed under the optimized concentration. The turn-on voltage of the device for pure MEH-PPV was about 6 V and decreased to about 4 V for MEH-PPV/MB-GQDs (1%), indicating that GQDs provided more electrical transport paths. However, at higher concentrations, agglomeration of GQDs caused charge trapping that increased the turn-on voltage. Wang et al. were the first to prove the concept of utilizing CDs alone as the active emission layer for a white light emitting diode [99]. They sandwiched CDs between PEDOT:PSS hole injection layer and TPBI electron transport layer. The relatively high turn-on voltage of the device (6 V) was attributed to the insulating nature of the passivating agent on the surface of CDs. The largest external quantum efficiency (0.083%) was obtained at current density of 5 mA cm^{-2}. External quantum efficiency is the ratio of the number of photons

emitted from the LED to the number of electrons passing through the device. In other words, it shows how efficient the device converts electrons to photons.

Rhee et al. employed amidative cutting of tattered graphite approach to synthesize GQDs of varied sizes by regulating the amine concentration [100]. It was demonstrated that increasing the size of GQDs narrows down the energy gaps showing colourful photoluminescence from blue to brown. Finally, they fabricated organic light emitting diodes with different concentrations of GQDs within a device architecture. Their results showed that although the larger GQDs have lower photoluminescence quantum yield they exhibited the brighter white electroluminescence implying that energy transfer from the host is the most important factor to achieve bright luminescence. The largest external quantum efficiency of their best device was 0.1% which is quite inferior to the state-of-the-art OLEDs and QDs based LEDs. The authors attributed such performance to the relatively low quantum yield (about 10%), decreased contact area with host molecules, too much deep highest occupied molecular orbital levels, and bulky ligand molecules hindering efficient charge transfer.

Zhang and co-workers fabricated LEDs with CDs as the active emissive layer the colour of which can be tuned from blue to white by controlling the driving current [101]. The fabricated devices are comprised of a CDs emissive layer sandwiched between an organic hole transport layer and an organic or inorganic electron transport layer made by solution-based processes. By controlling the current density injection via varying the applied voltage and tuning the architecture of the devices, they arrived at multicolour emission from the same CDs. Sonar and co-workers synthesized high quantum yield CDs from biowaste of human hair and demonstrated fabrication of rigid and flexible organic LEDs using CDs in two device architectures [102]. The turn-on

voltage for both devices was recorded 4.2 V, but the highest luminescence of the rigid device was twice as the flexible one. To preserve the emission, CDs were organized in long range self-assembled 2D arrays embedded in perovskite. This layer serves two purposes of hole transport and emission.

Although the development of CDs-based electroluminescence LEDs is still in its infancy, their tuneable fluorescence emission, low cost, and environment-friendliness warrant more in-depth studies to catch up with high performance QD LEDs. On this way, there are two major cHallenges to defeat: 1) development of CDs with high quantum yield and good charge transport properties in the solid state or thin film 2) engineering of the band energy levels through optimization of electron or hole transport layers.

2. 2. 3. 2. LEDs based on the photoluminescence of CD

The LEDs based on the photoluminescence of CDs are usually fabricated by application of fluorescent CDs powder on UV or blue chips. The CDs are used as phosphors to convert blue light into a wider spectrum. One major complication for this application of CDs is that they tend to agglomerate when consolidated into a thin film, which leads to weaker fluorescence due to aggregation induced quenching. To circumvent this, many groups have demonstrated that incorporation of CDs into solid matrices such as borax [103], silicone [104-106], starch [107], cellulose nanofiber [108], resin [109-112], and ionic salt [113] can preserve the fluorescence.

Tang et al. were probably the first to demonstrate the capability of GQDs to convert blue light into white light [114]. Exciting the coated GQDs with 410 nm weakens the intensity of the blue light, and a broadband emission centred at 510 nm appears, hence converting the blue light to white light. Li et al. embedded citric acid derived CDs within salt crystals of NaCl, KCl, KBr to preserve the luminescence intensity of

the dots and thermally stabilize them against the environment. The salt capsulated CDs were mixed with silicone rubber, then deposited on a UV LED chip for light conversion. NaCl capsulated LED retained 77% of luminescence intensity while the other LEDs lost almost all of their photoluminescence emission after a week of operation [113]. In another work from the same author [115], blue excitable yellow emitting CDs functionalized with tethered imidazolidinones were synthesized in a one-pot reaction, drop-cast on a glass slide and surface mount LED and dried. The prepared CDs on the glass slide can be peeled off from the slide after a week at room temperature. The obtained solidified CDs were proved to be flexible, transparent, freestanding films.

Chen and co-workers prepared CDs with pyrolysis of PS@PGMA photonic crystals at temperatures of 200 ºC, 300 ºC, and 400 ºC and realized blue, orange and white emission respectively under a single UV wavelength excitation [116]. The prepared CDs were encased in superglue and coated on a UV chip of 370 nm for this purpose. Rhee et al. synthesized CDs via emulsion-templated carbonization of polyacrylamide, then fabricated a luminescent film of CDs by incorporating them into a PMMA matrix [117]. The polymer functions not only as the mechanical support but also disperse CDs to avoid solid state quenching. In the last step, a white LED was realized by combining the film with a blue LED of 400 nm, and cool white light emission was obtained. Sun and co-workers combined blue emissive CDs with green and red emissive zinc copper indium sulphide (ZCIS) core/shell QDs to achieve white LEDs [118]. Throughout this study, it was demonstrated that the broadband emission of ZCIS can be employed to cover up the emission of CDs in yellow and red regions for production of white LED.

Although the incorporation of CDs into solid matrices is proved to be a good strategy to prevent fluorescence quenching, the introduction of a thick matrix layer may suppress the luminescence from chips and increases the cost. Therefore, realization of high-quality luminescence in the solid state from CDs and their direct deposition as phosphor in LEDs is desirable. Li et al. reported the synthesis of inter-crossed carbon nanorings with pure hydroxy surface states enabling them to overpower aggregation induced quenching and to emit stable luminescence in both colloidal and solid states [119]. Thereafter, carbon nanorings were deposited on blue LED chips to realise white LEDs with colour coordinates near to pure white light.

Liu and et al. developed self-quenching-resistant CDs via the hydrothermal treatment of PVA and EDA, as carbon and nitrogen sources, respectively [120]. If the fluorescence of CDs emanates from surface fluorophores and graphitizing cores, the self-quenching-resistant mechanism was attributed to surface nitrogen doping and control of inter-particle spacing because the steric hindrance of the PVA chains keeps the aggregates within an appropriate interval between its inner particles. Thereafter, a transparent film of CDs/PMMA was realized for conversion of blue light into white light. Rhee and co-workers prepared CDs via solvothermal carbonization of citric acid and chemically modified their surface with a series of para-substituted anilines to endow them exhibition of long wavelength PL in a narrow spectral width [121]. The synthesized CDs were then incorporated into PMMA to fabricate a solid thin film for conversion of UV light into a variety of colours.

From comparing the performance of the-current-state-of-art QDs and CDs LEDs it can be inferred that quantum yield of CDs in the long wavelength emission is way lower than QDs, however CDs LEDs are in a younger stage of development. Therefore,

development of new synthesis methods for large scale production of CDs with high quantum yield in long wavelength emission is still a cHallenge to be surmounted.

2. 2. 4. Chemo-resistive gas sensors

CDs carry a reputation for bioimaging and fluorescence sensing [122] and are barely investigated for chemo-resistive gas sensing, yet there are a limited number of studies discussing the role of CDs in conductometric gas sensors.

Zhang et al. prepared CDs through electrochemical ablation of graphite followed by dialysis against pure water [123]. Oxygen functionalized CDs were also prepared from candle soot. Comparing the change in conductivity of the two thin films against different values of relative humidity demonstrated that oxygen contained groups on the surface play a crucial role in sensing mechanism. When the CDs film is exposed to humidity, oxygen contained groups on the surface can form hydrogen bonds with water molecules facilitating the electron migration which leads to the increase of electrical conductivity. Hatamie and co-workers prepared a flexible humidity gas sensor with hydrothermally synthesized GQDs as the sensing film and Kapton as the substrate [124]. The sensor was selective to humidity against the tested gases and responded exponentially from 0% to 100% relative humidity.

Taher and co-workers prepared GQDs through pyrolysis of citric acid followed by hydrazine reduction [125]. Thereafter, the obtained powder was drop cast on interdigitated electrodes to fabricate a gas sensor. The sensor exhibited the highest sensitivity to HCN compared to several analytes tested. The presence of oxygenated functional groups on the surface of GQDs facilitates HCN adsorption. However, this occurs only in the absence of water molecules because in a humidified atmosphere, water molecules strongly interact with populated oxygen containing groups on the surface hindering the HCN adsorption. Such influence on the performance of the

sensor should be seriously considered as at the relative humidity value of 43%, the response of GQDs to HCN is completely lost. Taromi et al. combined PEDTO:PSS with hydrothermally synthesized nitrogen doped GQDs to make the sensing material for detection of volatile organic compounds at room temperature [126]. They observed that the highest sensitivity of the nanocomposite is towards methanol. The resistance change of the N-GQD polymer was explained based on two possible mechanisms; (1) when methanol molecules are adsorbed on the surface of the nanocomposite by physiosorption, the holes on the surface interact with electrons that methanol donates. This not only delocalizes the conjugated π-electrons of the sensing film but also decreases the number of charge carriers, resulting in lowering the electrical conductivity. (2) the observed swelling of the conductive polymer while detecting volatile organic compounds may also contribute to decline of conductivity. When the film is swelled, the distance between PEDOT interchain increases and the embedded N-GQDs, which act as pathways for electrons hopping, stay apart, leading to conductivity decrease of the film.

Fardindoost and co-workers chemically synthesized GQDs and evenly distributed them in WO_3 sol. Thereafter, palladium chloride salt was dissolved in the sol as the catalyst to make the sensing material more sensitive [127]. It was shown that the sensor can operate at low temperature of 120 ºC and exhibited the highest response to H_2 in selectivity test. The sensing mechanism of Pd/GQD/WO_3 film is as follows; GQDs function as the bridge between WO_3 grain boundaries shortening the transport pathways, which improves the poor electrical properties of tungsten oxide. Moreover, Pd acts as a catalyst to reduce the activation energy required for dissociation of H_2 molecules on WO_3 particles. When the film is heated at environmental air, oxygen molecules (O_2) are chemisorbed on WO_3 grains with negative charges (O^-) and extract

electrons from the N-type semiconductor. Exposing to H_2, the gas interacts with surface adsorbed oxygen, and some quantity of electrons proportional to the concentration of the target gas are released to the conduction band of WO_3, resulting in the decrease of the resistance of the film.

Chu et al. prepared SnO_2/GQDs nanocomposite via a solvothermal method. Comparing the gas sensing properties of SnO_2/GQDs and pure SnO_2 films at 275 ºC demonstrated that the composite is remarkably selective to acetone [128]. In another work from the same author, the gas sensing properties of hydrothermally synthesized ZnO/GQDs nanocomposite were investigated [129]. It was shown that the addition of GQDs to ZnO enhances gas response of the film to all tested VOCs. The defects and functional groups on the surface of GQDs act as active sites that could increase the adsorption of gas molecules. Besides, the GQDs/ZnO interface forms a forward-biased Schottky barrier leading to easy migration of electrons. Zhang et al. prepared two dimensional reduced graphene oxide-carbon dot (rGO-CD) hybrid in which reduction of GO is accompanied by in situ generation of CDs [130]. This all-carbon nanoscale heterostructure enhanced the gas response 3.3 times compared to bare rGO. This improvement was attributed to the number of active sites at the grain boundaries that the heterostructure provides for NO_2 molecules absorption.

2. 2. 5. Photodetectors

Tang and co-workers synthesized N-doped GQDs via a microwave-assisted route [131]. The N-GQDs exhibited notable broad absorption covering UV, visible and near infrared range. According to the authors, the UV absorption is ascribed to transitions in C=C, C=N and C=O bonds, the visible absorption is due to extended partial conjugated π electrons in the graphene layer, and the near infrared absorption is attributed to more extensive π-electron delocalization. To implement a photodetector,

the N-GQDs were drop cast on a glass substrate with gold interdigitated electrodes patterned on it. To derive a constant current, it was required to increase the bias voltage. This was attributed to the domination of photoinduced trap states, which restricted the transport of charge carriers in the film. Cheng et al. fabricated an all-carbon phototransistor composed of GQDs on a single layer of graphene supported by Si/SiO$_2$ substrate [132]. Conducting carbon paste was used to make the drain and source contacts. It was shown that the photocurrent dramatically increases with dispersion of GQDs on the graphene layer as the sample without GQDs exhibited a negligible current under illumination. Therefore, it is the high absorptivity of GQDs that determines the behaviour of the photodetector. Rapid photoluminescence quenching of GQDs is another evidence to demonstrate successful charge transfer to graphene. Tam and co-workers presented a photoconductive device based on reduced graphene sheet decorated with GQDs and contacted by two gold electrodes [133]. In this configuration, GQDs act as the light-absorbing material for generation of charge carriers and, rGO serves as the charge transporting medium. The photoresponse of the device was attributed to the transfer of photogenerated electrons at the GQDs/rGO junction that passes through rGO to Au electrodes. Kim et al. fabricated a broadband carbon-carbon hybrid photodetector by sandwiching GQDs in between two layers of graphene [134]. Two Ag electrodes were evaporated onto the top and bottom graphene layers, and a Si/SiO$_2$ wafer served as the substrate. It was observed that the photoresponse of the detector became bias dependent at high intensities. This bias dependency was ascribed to charge carrier extraction of the top and bottom graphene layers, which occurred due to the difference in their barrier heights.

2. 2. 6. Lithium-ion batteries

Chao and co-workers' electrophoretic deposition of GQDs on VO_2 nanobelt to act as the cathode material for Li-ion and Na-ion batteries is the first presentation of CDs in this application [135]. The role of GQDs in this configuration is to separate VO_2 nanobelts to avoid agglomeration as well as minimizing the dissolution of active materials. This method of protecting unstable materials with GQDs was applied on CuO/Cu triaxial nanowire composite by the same research group to function as the anode material in lithium-ion batteries [136]. A comparison between the performance of unprotected CuO/Cu nanowire electrode and GQD protected one demonstrated that protection of GQDs greatly enhances surface conductivity and stability of the structure that results in long-term cyclability. Ji et al. coated CDs on Mn_3O_4 via an alternating voltage electrochemistry approach and utilized the yielded composite as the anode material for Li-ion batteries [137]. The coated sample showed five times enhancement in reversible discharge capacity after 50 cycles at current density of 100 mA/g compared to pure Mn_3O_4. This enhancement was attributed to the formation of octahedral structure of Mn_3O_4 due to introduction of CDs. Craig and co-workers synthesized nitrogen-doped TiO_2 nanorods decorated with CDs via a hydrothermal reaction process and utilized the composite as the anode material for Li-ion batteries [138]. The role of CDs in this configuration is to improve electrical conductivity and charge transfer reaction.

Chapter 3 Materials and Methods

3. 1. Synthesis

The N-CDs were synthesized via hydrothermal method using precursors of citric acid (CA) and varied amounts of urea as the carbon and nitrogen sources, correspondingly. Both CA and urea are sourced from CSA Scientific. For the synthesis of samples A to G, 5.25 g of CA were added to 25 mL of deionized water under vigorous stirring, then 0.82 g, 0.69 g, 0.59 g, 0.47 g, 0.32 g, 0.164 g, 0.082 g of urea were added to the solutions, respectively, which is representative of CA/urea molar ratio of 2, 2.375, 2.75, 3.5 ,5 ,10 ,20 (

Table 3.1). After 10 minutes that the solutions cleared, they were transferred to 100 mL Teflon autoclaves and sealed for 10 hours under heat treatment at 180°C. Thereafter, once the autoclaves were naturally cooled down to room temperature, the samples were collected. To sieve the large particles out of the samples, they were passed through syringe filters of 0.22 µm. Finally, the filtered products were freeze-dried to obtain solid-state N-CDs. The solution and freeze-dried N-CDs samples under natural and ultra-violet light are shown in Figure 3.1.

Table 3.1. The ratio of the constituents of the prepared precursors for synthesis of the N-CDs samples.

	A	B	C	D	E	F	G
Citric acid	5.25 g						
Urea	0.89 g	0.69 g	0.59 g	0.47 g	0.32 g	0.164 g	0.082 g
CA/Urea molar ratio	2	2.375	2.75	3.5	5	10	20

Figure 3.1. The N-CDs sample solutions under natural (A) and UV light (B), the freeze-dried N-CDs samples under natural (C) and UV light (D).

3. 2. Introduction to characterization techniques

3. 2. 1. Introduction to X-ray photoelectron spectroscopy

X-ray photoelectron spectroscopy is a technique used for analysis of the composition and chemical bonding states of the elements on the sample surface. Irradiating a solid in vacuum with monoenergetic soft X-rays and measuring the kinetic energy is the basis of this technique [139]. As photons are chargeless packs of energy, their interaction with atoms on the surface transfers energy to electrons. Enough of this energy can result in ejection of electrons/production of photoelectrons. The kinetic energy that remains on the photoelectrons is the favoured quantity for XPS measurement because this energy is a function of binding energy that is a definite characteristic of each element. The binding energy is the difference between the energy of photoelectrons in the initial and final state after leaving the atom. The kinetic energy of emitted electrons can be measured:

Equation 3.1.
$$KE = h\nu - BE - \Phi_s$$

where $h\nu$ is the energy of the photon, BE is the binding energy of the atomic orbital the electron originates from, and Φ_s is the spectrometer work function. The number of detected electrons per energy interval plotted against their kinetic energy is the XPS spectrum. As each element has specific sets of binding energies, every one of them has a unique XPS spectrum. Peak heights and areas, in addition to spectral features of this plot, can provide quantitative data to identify the concentration of chemicals on the surface of the material under analysis.

XPS analysis is a surface-sensitive technique. Although the irradiated photons can interact within path lengths on the order of 1 to 10 μm, the mean free path of electrons is on the order of tens of angstroms. Therefore, only the top few atoms on the surface region can release electrons without energy loss useful for kinetic energy

36

measurement [139]. This technique may not be practical if the composition of the sample material near the surface region differs from the bulk of it. An element might be below the detection limit if the element is uniformly distributed in the sample but might be detected if that element was concentrated on the surface. However, our use of XPS for characterization of carbon dots is very informative as the diameter size of these materials is around 2-5 nm which is within the detection limit.

An XPS instrument includes vacuum chamber, X-ray source, energy analyser, transfer lens system, charge neutralizer and stage. X-ray source provides photons with specific energy for irradiation onto the sample; emitted electrons move freely along the vacuum chamber; transfer lenses collect photoelectrons and focus the electron beams towards the energy analyser; electrons of known kinetic energy can pass through energy analyser to the detectors; charge neutralizer prevents the accumulation of charges at the sample position; stage keeps the sample positioned [7]. The instrument determines the number of electrons in known energies for specific time intervals through a sequence of measurements. The output data is counts per second of electrons as a function of their corresponding kinetic energy.

A general rule of thumb when performing XPS analyses, particularly on samples of unspecified composition, is to first collect spectra over a wide range of energy. This could be performed under a poor resolution of energy to efficiently minimize the analysis time. Survey spectra, the obtained spectra under this condition, depicts the general peak structure of photoelectron emission intensity. It reveals the effective binding energy peaks, which can be highlighted for further high-resolution studies. The main objective of obtaining survey spectra is to determine the elemental composition of the sample based on the information from the binding energy peaks. Primary peaks in this XPS spectra represents the entirety of collected photoelectrons that the

instrument detects following the excitation of the sample surface. For obtaining these peaks, the work function of the instrument is considered as the lost energy. The background signal in the spectra is due to inelastic scattering of photoelectrons on the sample surface before arriving at the vacuum chamber. The inelastic scattering is an interaction that causes loss of energy of the incident primary electron [140].

The recorded number of electrons that leave the sample surface form the XPS spectra, but the instrument may not be able to detect all the emitted electrons. The kinetic energy of emitted electrons and the operating mode of the instrument may impact the efficient detection of photoelectrons. Moreover, transition of electrons from different electronic states of the same element may vary in the peak area. Therefore, it is needed to process the obtained raw data for better evaluation of the sample composition. Peak intensity and position are the most important values for the analysis of XPS spectra. The peak intensity is indicative of concentration of the material on the surface, while peak position is useful for analysis of elemental and chemical composition. Percentage atomic concentration tabulates the ratio of the area under each peak to the total area in percentages. The obtained numbers show how much of each material is present on the surface of the sample in percentages. A set of relative sensitivity factors (RSF) are applied in the XPS analyses to compensate for the disproportionality of the peak areas with the real quantity of the corresponding element. The sensitivity factors scale the measured areas to find meaningful atomic concentrations. Of other values of merit that should be considered in processing the data for XPS analysis is full width at half maximum (FWHM) that points at peak broadening. The broadening of a peak may be due to higher number of contributing chemical bonds that shape the peak structure.

3. 2. 2. Introduction to Fourier transform infrared spectroscopy

Fourier transform infrared (FTIR) spectroscopy is a technique used for identification and characterization of materials based on the interaction of infrared radiation and molecules. Infrared spectrum of absorption or emission of a solid, liquid or gas can be obtained using this technique. Organic and inorganic chemicals which contain covalent bonds absorb electromagnetic radiation wavelengths in the infrared region that is longer than the red edge of the visible (700 nm) and shorter than microwaves (1 mm) radiation [141]. The electromagnetic radiation wavelengths are depicted in Figure 3.2. The IR spectrum can be divided into three sub-spectral areas, named in relation to the visible range: (1) near-infrared (NIR) that is near the visible region and may excite overtone or higher harmonic vibrations (770–2500 nm), (2) mid-infrared (MIR) that mostly excites fundamental vibrations (2.500–25 µm) and (3) far-infrared (FIR) that excites lattice and rotational vibrations (25–1000 µm) [142]. Of these spectra, the MIR is used for chemical analyses. The IR radiation is generally expressed in wavenumber in preference to wavelength. The reason behind this preference is that energy and wavenumber are directly proportional, e.g. higher wavenumber higher energy. Wavenumber is the number of waves per unit distance that is equal to the wave frequency divided by the speed of light. Therefore, the corresponding wavenumbers for 2.5 to 25 µm region is 4000 to 400 cm^{-1}. Conversion of wavenumber ($\bar{v}$) to frequency (v) is as follows:

Equation 3.2.
$$\bar{v}\ (cm^{-1}) = \frac{1}{\lambda(cm)}$$

$$v(Hz) = \bar{v}c = \frac{c(cm/sec)}{\lambda(cm)}$$

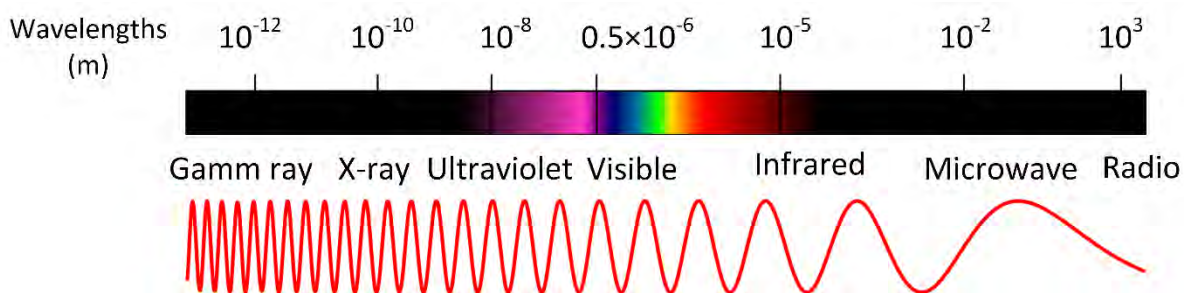where c is the speed of light, and λ is the wavelength.

Figure 3.2. Electromagnetic radiation wavelengths

Absorption of energy, including from infrared radiation, excites molecules to higher energy states. However, only energies of certain wavelengths that correspond to the natural vibration frequencies of the molecule are absorbed within the infrared region. This absorbed infrared energy in MIR amplifies the vibrational motions of the bonds with dipole momentum. Symmetrical molecules that share electrons evenly do not have a dipole moment to change as a function of time when absorbing infrared radiation and consequently have no characteristic IR spectrum fingerprint. The dipole moment of a bond in polar molecules varies in harmony with the frequency of incoming electromagnetic radiation for transfer of energy. The intensity of absorption depends on how effectively this energy is transferred to the molecule via dipole moments. As the covalent compound with polar molecules absorbs energy, the molecules tend to vibrate – stretching or bending depending on its geometry [143].

Considering the distinctive natural frequency of vibration in each type of bond and given the fact that the same type of bond in two different compounds may leave dissimilar footprints in the infrared absorption pattern, it can be said that no FTIR spectra of two different substances are alike. Therefore, the infrared spectrum of each compound is a chemical signature against which the absorption pattern of substances under analyses can be compared. If the FTIR spectra peaks of the two compounds are aligned, it is highly probable that the two substances are identical. Gaining information about the structure of a molecule is another advantage FTIR offers for

chemical analyses as the absorption of each type of bond appears in specific segments of the vibrational infrared region.

Modelling of the stretching vibrations can be exercised using harmonic oscillators [144]. Two point-masses joined by a spring symbolizes a chemical bond in this model)Figure 3.3(. The point-masses (m_1 and m_2) represent the atoms or chemical groups in the bond and the spring tenseness (k) models the bond strength or molecular force field. The vibration frequency (v) can be calculated:

Equation 3.3.

$$v = \frac{1}{2\pi c}\sqrt{k\frac{m_1+m_2}{m_1 m_2}}$$

Where m_1 and m_2 (g) are atom masses, k is the bond strength (dyne.cm^{-1}), and c (cm.sec^{-1}) is the speed of light.
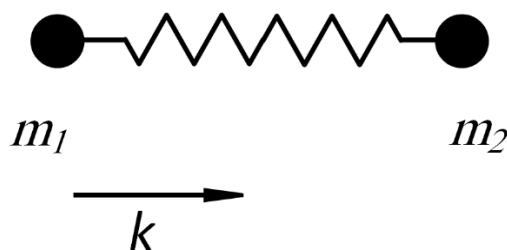
Figure 3.3. Harmonic oscillator model estimates the stretching vibrations.

As this oscillation frequency depends on the bond strength, double and triple bonds have higher frequencies. As a result of this, several factors such as group environment, electronegativity of neighbouring atoms, and hydrogen bonding interactions can influence the frequencies. For example, if one atom is involved in a hydrogen bond the bond strength decreases and the stretching mode frequencies of the chemical group downshift. However, the vibrational frequencies of a chemical are supposed to be in specific regions. Therefore, for detailed association of infrared frequencies and structural properties of a novel material when no data is available, it

may be required to do the IR analysis in different solvents and rule out the effects of the environment in the analyses [144].

An infrared spectrometer is an instrument that records the infrared absorption spectrum for a compound. The outcome of this instrument is a plot of wavenumber versus transmitted light. In part of the spectrum that samples do not absorb any energy, the transmittance is 100% denoting it is transparent to the radiation of those wavelengths. Therefore, the minimum transmittance peaks on the plot correspond to the maximum absorption of energy on that frequency.

An FTIR spectrometer is comprised of IR source, interferometer, sample compartment, IR detector, amplifier, analogue to digital converter and a computer [145]. The IR source is a high temperature alloy heated electrically to radiate thermal emission in the infrared region of the electromagnetic spectrum. The IR beam passes through the interferometer before being oriented towards the sample. Interferometer is an optical device consists of a beam splitter, a stationary mirror and a moving mirror designed for separation of spectral components of the beam in time. The beam splitter transmits half of the beam towards the stationary mirror and reflects the other half towards the movable mirror. Thereafter, the two beams recombine with each other at the beam splitter when reflected from the mirrors, but the pathlength differences of the beams have brought up interferences. Then, the generated interferogram which contains these interferences is directed towards the sample. Absorption of particular IR wavelengths by the sample modifies the interferogram. The detector collects the modified interferogram that has information about the absorbed amount of energy at every wavelength and converts it to analogue electrical signal. Then, the amplifier intensifies the signal and, the analogue to digital converter translates it to digital codes for further processing by computer. The computer makes a standard comparison

between the modified interferogram and a reference to extract the differences between the two signals. The computer also performs the mathematical operation of Fourier transform to construct a plot of infrared spectrum for the sample.

3. 2. 3. Introduction to transmission electron microscopy

Transmission electron microscope (TEM) has played an increasingly important role in material science, physics, biology, and nanotechnology to date. This powerful tool is the keystone for founding approaches in many realms of science as it is capable of visualizing things in nanoscale order.

From the advent of electron microscopy in 1931, it has had great impacts on the advancement of science and technology. We know from quantum physics that every particle or quantum entity can be described as either particle or wave. Having a comparison between the beam of light and electrons, which underlies the fundamentals of optical and electron microscope, respectively can lead us to a few differences and similarities. Both can have varied speeds and wavelengths. Interestingly, the wavelength of an electron is dependent on its speed. The wavelength of an electron decreases with increasing the acceleration voltage, and with the decrease of the wavelength, better resolution is achievable [146].

Although electron beams of high voltage are very informative about soft materials in high magnifications, there are contingencies that need to be considered in TEM imaging. As samples are put into vacuum for TEM analysis, it is needed to know that whether the characteristics of the material change under the vacuum condition. Moreover, radiation damage to samples at high acceleration voltage is possible to occur. The desired resolution for the TEM images determines how much energy the sample should be able to endure [146]. At high magnifications, the beam is focused on a small area of the sample. At higher operation voltages, the electron velocity would

be higher, and the specimen absorbs more energy for better image resolution. However, the decrease of the image contrast is expected as the number of interactions between the beam and sample is reduced.

By propagation of a bundle of waves onto a sample, some of them may interact with it and generate backscattered electrons, elastic electrons and inelastic electrons [147]. Backscattered electrons are those of the primary beam that had electrostatic interaction with the positively charged nucleus of an atom and are backscattered at an angle of more than 90°. Technically, these electrons have the same energy as the electrons of the primary beam. If the interaction of primary beam electrons with the nucleus results in electrons scattering at an angle of less than 90, those are elastic electrons. The bent of the angle for scattering electrons depends on how close electrons pass the nucleus and how heavy the nucleus is. The electric potential of a heavier nucleus bends the path of electrons more, in particular, when the primary electrons pass closer. In elastic scattering, electrons do not lose energy. The high-resolution information for the formation of TEM image is available in the elastic electrons. If electrons lose energy in their interaction with the cloud of electrons, they are inelastic electrons. In inelastic scattering, some energy is transferred to the sample and may cause radiation damage. Inelastically scattered electrons are not of much use for the construction of TEM images because they are less localized and, their interaction with the lenses may vary the focal lengths.

The general design of an electron microscope is comparable to that of a light microscope. Electron beam replaces the light and, glass lenses are substituted with electromagnetic/electrostatic lenses. TEM instrument consists of electron source, electromagnetic lenses, sample holder, lenses, and camera. A thermionic or field emission gun provides the beam of electrons to travel through a vacuum column in

which the sample holder is placed. There is a number of electromagnetic lenses along the column from top to bottom, each of which with a defined responsibility. The focal width of the lenses is selected based on the required strength of magnetic field. The first lens system which controls the overall brightness is condensers. They bundle electrons and direct them onto the sample. After transmission of electrons from the specimen, the objective lenses come into play to construct the primary image [147]. Thereafter, the primary image is magnified by the projective lenses, a system of two or three lenses that act together to project the magnified image on a detector. The charged couple device camera, which acts as the image plane detector, translates electrons into photons in the scintillator layer. The use of an in-column or post-column energy filter can enhance the signal to noise ratio by removing inelastic electrons that have different wavelengths [146].

The selection of electron source, microscope and operating voltage depends on the research question needed to be addressed. It may be required to compromise on one aspect of imaging to have optimum trade-offs between all the qualities. For example, at higher acceleration voltages, the mean free path of electrons increases. Consequently, the number of electron interactions with the sample decreases, which leads to higher resolution and possible radiation damages. Hence, high voltages are suitable to be used for thick, soft matter samples that are difficult to penetrate. Another example is the trade-off between brightness and contrast. Higher acceleration voltage increases the brightness and decreases the contrast. Therefore, the acceleration voltage is selected depending on the required contrast, brightness, resolution or penetration.

Formation of the TEM image is by wave interference of the electrons travelled through the sample. If the interferences of the waves upon their meeting are in phase, it is

called constructive. Otherwise, it is described destructive. A diffraction pattern from the combination of constructive and destructive wave interferences can be visualized by shining a laser on evenly spaced grating and placing a camera some distance further [146].

Sample preparation is of great importance for TEM imaging as the sample needs to endure vacuum conditions and electron beam radiation. The preparation should be designed in a way to preserve the natural state of the sample. For instance, drying is an appropriate approach to prepare samples of hard materials while it may spoil organic and soft materials. Another example is that radiation is less likely to damage dry samples of heavy metal. Instead, they can bring good contrast. For a good design of sample preparation, a balance between the choices of contrast, resolution, and natural state preservation should be thought about.

Staining with heavy metal can improve the contrast and protect the sample against dehydration and radiation damage. However, this preparation method suffers from a few drawbacks that should be considered. Staining restrains visible orientation as it needs sample support. The grain size of the metal can be an obstacle to obtain the possible maximum resolution. Moreover, dehydration which is required for staining may change the native state of the specimen. Positive staining is addition of metals to specific parts of the sample, while in negative staining, ground metal solution envelopes the sample. Another good sample preparation technique for TEM imaging is cryo-fixation. A drop of the solution sample is dripped on a gold or copper-coated grid and blot it to have a thin layer on the gird. Then, the gird is plunge frozen in liquid ethane/propane.

3. 2. 4. Ultraviolet, visible, and near-infrared absorption spectroscopy

The electronic, vibrational, and rotational transitions can be shown in the absorption spectrum. The maximum of this spectrum relates to the electronic transition line, while rotational and vibrational transitions are reflected in the series of lines in other parts of the spectrum. A molecule can have one, two or several absorption peaks depending on its structure. The population of molecules in the excited state can determine the absorption intensity. Absorption spectra is temperature dependent. The increase in temperature can expand the rotational and vibrational states in the molecules resulting in the broadening of the recorded spectrum [148].

Characterization of electromagnetic radiation is performed based on the amplitude, frequency, and phase like other wave phenomena. Photons are massless quantized elementary particles responsible for all light radiation of electromagnetic waves. The energy of photons is obtained from Planck's relation:

Equation 3.4.
$$e = h\nu = h\frac{c}{\lambda}$$

where h is Planck's constant, c is the speed of light, ν is frequency, and λ is the wavelength which is reciprocal of frequency.

The visible region of electromagnetic wavelengths to us is from around 400 to 700 nm. In study of absorption and fluorescence, the wavelengths range between 200-1000 nm is generally characterized. The wavelengths below 200 nm carry enough energy to cause irreversible disassociation of the absorbing molecules to free radicals. Scarcity of electronic transitions at wavelengths above 1000 nm in addition to strong infrared absorption of water are the reasons for this longer limit. Infrared absorption of water hinders the observation of samples containing water such as biological molecules [149].

3. 2. 4. 1. Electronic transitions for absorption of light in molecules

Electronic transitions occur in UV, visible and near infrared spectral regions. The pathway of a molecular electronic transition caused by photon absorption is from lower electronics states, normally ground states to higher electronic states (excited states). For practical purposes, it is usually assumed that the absorption of light is from the molecules in the lowest ground state. The highest occupied molecular orbital (HOMO) and the lowest unoccupied molecular orbital (LUMO) are the two types of orbitals in absorption and fluorescence spectroscopy. Both correspond to the ground state. Take formaldehyde as an example. Figure 3.4 shows the HOMO and LUMO and possible electronic transitions between the energy levels of formaldehyde. The order of energy of these electronic transitions is as follows [150]:

$$n \rightarrow \pi^* < \pi \rightarrow \pi^* < n \rightarrow \sigma^* < \sigma \rightarrow \pi^* < \sigma \rightarrow \sigma^*$$
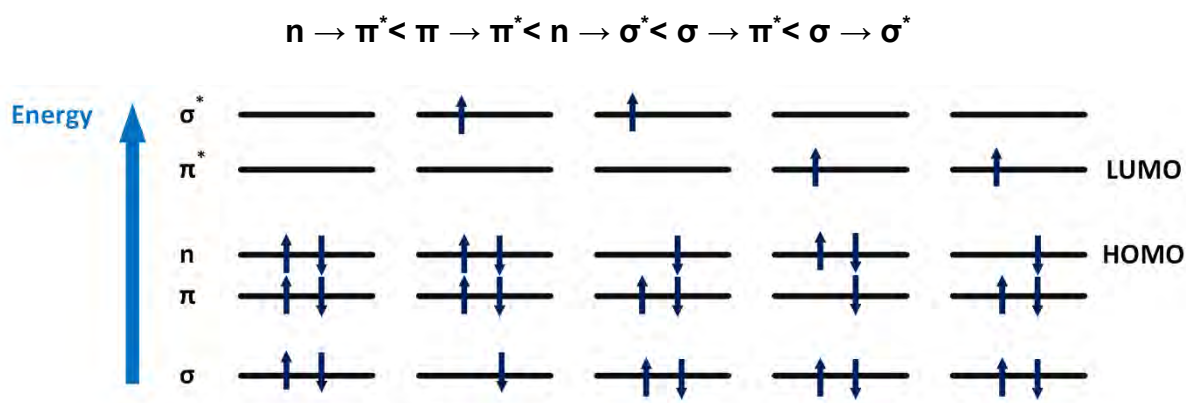
Figure 3.4. Energy levels of molecular orbitals in formaldehyde and possible electronic transitions [150].

Let us have a brief introduction about the formation of different types of orbitals. Two S atomic orbitals, or two P atomic orbitals having a collinear axis of symmetry, or one S and one P atomic orbital are the possible combinations for formation of orbitals. These bonds are called sigma bonds. Two P atomic orbitals that laterally overlap are π bonds. For instance, two carbon atoms are linked by one σ and one π bond in ethylene ($CH_2=CH_2$). Photons of appropriate energy can excite π electrons to an

antibonding orbital of π* (π → π*). To excite σ electrons, absorption in the far UV is needed. Heteroatom molecules such as oxygen or nitrogen can have nonbonding electrons with corresponding molecular orbital called n orbitals. It is possible to excite nonbonding electrons to antibonding orbitals [150].

3. 2. 4. 2. Franck–Condon principle

The Franck-Condon principle explains the intensity of vibronic transitions in polyatomic molecules. The simultaneous changes in electronic and vibrational energy levels owing to the absorption or emission of photons of appropriate energy are vibronic transitions. According to this principle, a change of vibrational energy level in an electronic transition is more probable if the two vibrational wavefunctions overlap. In other words, the Franck–Condon principle states that alteration of electronic distribution can happen way faster than changes in bond angles and distances. Therefore, these sets of bonds and angles that shape the atomic configuration of a molecule do not change considerably in the absorption or emission processes. As a result, it is no surprise that broad absorption bands with long wavelength extension of the tails exist. They are often sensitive to temperature as reducing the temperature can cause a shift of the band edge to shorter wavelengths that is owing to decrease of thermally excited population [149].

The energy levels for atoms in the gas phase are discrete, and their corresponding absorption bands are well-separated, whereas the situation for molecules in the solution is different. In the gas phase, the gaps between vibrational levels are filled in with the well-defined quantized rotational levels. On the other hand, the absorption spectrum of molecules in the solution may consist of broad bands as free rotation with quantized energy is not possible, resulting in elimination of rotational structures. However, vibrational structures can be identified in the solution. The absorption band

of aromatic hydrocarbons in non-polar solvents is a good example for recognition of vibrational structure in the solution.

3. 2. 4. 3. Effect of conjugation and molecular environment on absorption

Molecular orbital theory depicts the light absorption of molecules with conjugation. A linear combination of atomic molecules is utilized in this theory to characterize molecular orbitals surrounding the molecule. Bonding, anti-bonding and non-bonding are the three categories of molecular orbitals that can give a picture of electronic transitions between various orbitals (Figure 3.5). Aromatic molecules are of great significance to fluorescence researchers. In most of them, light absorption in the lower energy region is due to $\pi \rightarrow \pi^*$ transitions.
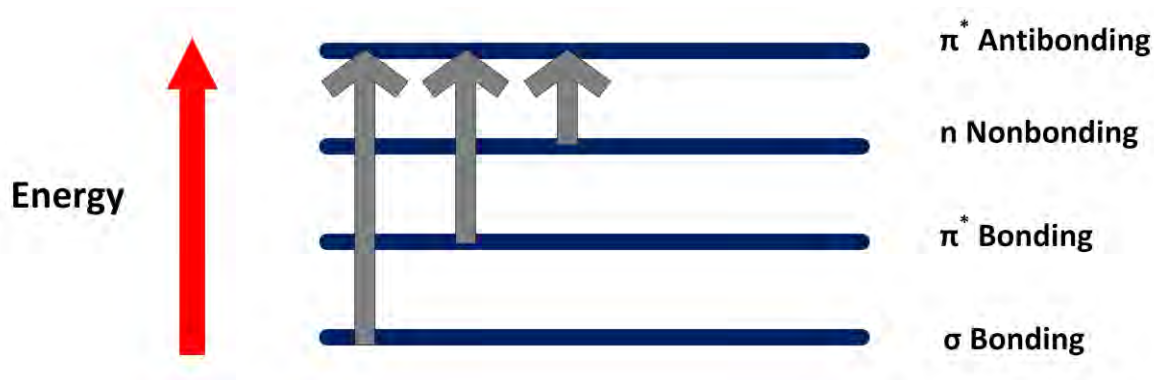
Figure 3.5. Energies of molecular orbitals and their associated transitions [149].

Carbon-carbon double bonds are of particular interest to us as it has π -orbital bonding which allows conjugation or delocalisation of π electrons in a system of alternating single and double bond. Conjugation and energy of $\pi \rightarrow \pi^*$ transitions in such systems are inversely proportional. The energy of $\pi \rightarrow \pi^*$ transitions decrease with the increase of conjugation in a molecule, which results in redshift in the absorption spectrum. The larger the extent of conjugation the larger the molar extinction coefficient and the more redshift in the absorption spectrum is observed [149]. Molar extinction coefficient is a measure of how strong chemicals attenuate light. Molecules that strongly absorb light have large extinction coefficients.

When the conjugated system comprises additional chemical groups, absorption spectra may be affected in two scenarios. First, if the additional chemical group contains chromophore, the absorption characteristics of chromophore may be added to the spectra. Secondly, the chemical group may fundamentally change the absorption spectra of the main molecule depending on whether it is electron donating or withdrawing.

Although the effects of molecular environment on fluorescence is our main concern when characterizing fluorophores, we need to know that molecular environment can also affect the absorption to a smaller degree. For instance, change of solvent polarity can impact the maxima of absorption spectrum and the extinction coefficient, though many of these effects are not significant [149].

3. 2. 4. 4. Beer–Lambert Law

The Beer-Lambert law describes the ability of a molecule to absorb light at specific wavelengths. The relation between extinction coefficient, sample concentration, and thickness of the absorbing medium is determined by this law. For study of solutions, they are placed in cuvettes, and the light passes through the cuvette. Therefore, the thickness of the sample is called the optical path length or simply path length. This Beer-Lamber law can be expressed as follows:

Equation 3.5.
$$A = OD = log(\frac{I_0}{I}) = \varepsilon c l$$

Where A is the absorbance of light through a material of pathlength I and concentration c. The term ε is extinction coefficient or molar absorptivity. I_0 and I refer to the intensity of the light entering and exiting the material, respectively. OD stands for optical density. From a practical perspective, the information from the absorption of solution is reliable when only the optical density is in the range of 0.01–2.0 depending on the precision of the instrument. If the optical density exceeds two, the parasitic light can deviate the

spectrophotometer from linearity, whereas the lower limit of 0.01 is because of the inherent noise in the instrument. Another consideration for absorption measurement is that spectrophotometers are dual-beam design. The instrument compares the absorbed light from a sample solution to the blank solution and calculates the absorbance for each wavelength [149].

3. 2. 4. 5. Practical Considerations

Despite our fundamental understanding of light absorption theory, absorption measurements are prone to misleading results due to a number of factors. From Beer–Lambert's law, we know that optical density and concentration of the absorbing solution are directly proportional, whereas in practice this proportionality may not hold linear in some cases. The erroneous results from deviation from Beer–Lambert's law can be from both intrinsic and instrumental causes. For instance, large aggregates like macromolecules in biological samples scatter light which may be simply identified as background absorption.

In the early days of spectrophotometers, fluorescence or parasitic light could reach the detector causing inaccurate results. A fraction of undesired wavelengths in the original incident beam that is not absorbed could largely contribute to the total light reaching the detector reducing the apparent optical density. This can produce unreliable measurement results for high optical density solutions. If dilution of a solution with an optical density higher than two is not possible for some reason, an alternative approach is to use short path length cuvettes [149].

3. 2. 5. Fluorescence emission spectroscopy

3. 2. 5. 1. What is luminescence?

The German physicist Eilhard Wiedemann coined the term luminescence from the Latin root of *lumen* (light) in 1888 to refer to phenomena conditioned by light in contrast

to incandescence, phenomena conditioned by increase of temperature. In technical terms, luminescence is the spontaneous emission of radiation from an electronically excited species or from a vibrationally excited species not in thermal equilibrium with its environment [150]. In modest words, when a light of certain colour is irradiated on some substances, they may shine a light of different colour after a very short time. Table 3.2 shows a summary of different types of luminescence categorized based on the mode of excitation.

Table 3.2. different types of luminescence [150]

Phenomenon	Mode of excitation
Photoluminescence (fluorescence, phosphorescence, delayed fluorescence)	Absorption of light (photons)
Radioluminescence	Ionizing radiation (X - rays, α, $β$, $γ$)
Cathodoluminescence	Cathode rays (electron beams)
Electroluminescence	Electric field
Thermoluminescence	Heating after prior storage of energy (e.g., radioactive irradiation)
Chemiluminescence	Chemical reaction (e.g., oxidation)
Bioluminescence	*In vivo* biochemical reaction
Triboluminescence	Frictional and electrostatic forces
Sonoluminescence	Ultrasound

In fluorescence and phosphorescence, the mode of excitation is the absorption of photons. Spontaneous emission of excited photons that is one of the consequences of the interaction of light and matter is called photoluminescence. In fluorescence, the

electron in the excited singlet state is paired with another electron in the ground state. Therefore, de-excitation to ground state accompanying emission of light is spin allowed and happens quickly. On the other hand, in phosphorescence that is the emission of light from triple excited states, the transition to ground state is spin forbidden, and therefore, the emission rate is slow. In other words, fluorescence is the spontaneous emission of luminescence with retention of spin multiplicity, and phosphorescence is long-lived emission of luminescence with change in spin multiplicity. The fluorescence lifetimes of many fluorophores are in order of nanoseconds, while phosphorescence materials may shine for several minutes. It should be mentioned that the distinction between fluorescence and phosphorescence is not always obvious from technical point of view.

The above description of fluorescence and phosphorescence are applicable to organic materials. There are other species like semiconductor nanocrystals, carbon dots and metallic nanoparticles that emit light but do not fit in these categories simply based on the concept of spin multiplicity. However, a huge number of publications talk about fluorescence quantum dots, fluorescence carbon dots and fluorescence gold nanoparticles in literature.

Illuminating light on semiconductor quantum dots generates pairs of electrons and holes. It is the recombination of electrons and holes in these materials that causes emission of photons. Therefore, if they recombine rapidly, the produced light has more characteristics of fluorescence, but if they are trapped in some metastable states, the recombination requires more energy, depends on temperature, and may have lifetime in order of phosphorescence. This temperature-based definition of fluorescence and phosphorescence is not applied for organic molecules [150].

3. 2. 5. 2. Characteristics of fluorescence emission

The emission characteristics of molecular fluorescence are briefly discussed in this section. The Perrin – Jablonski diagram visualizes the possible processes of photon absorption, internal conversion, fluorescence, intersystem crossing, phosphorescence, and delayed fluorescence. In this diagram, the possible transitions between the electronic states of a molecule are illustrated to depict the above phenomena in a molecule.

In the simplified Jablonski diagram shown in Figure 3.6, S_0 refers to the fundamental electronic state or ground state, which has the lowest vibrational energy level at room temperature. S_1, S_2, … are the singlet electronic states and the vibrational levels corresponding to triple states are denoted with T_1, T_2, and so on. Absorption is shown with vertical arrows starting from S_0 as the greater number of the molecules are in this vibrational level at room temperature. Photon absorption may excite the molecule to higher vibrational levels. Thereafter, the following radiative and non-radiative de-excitation processes can happen [150].
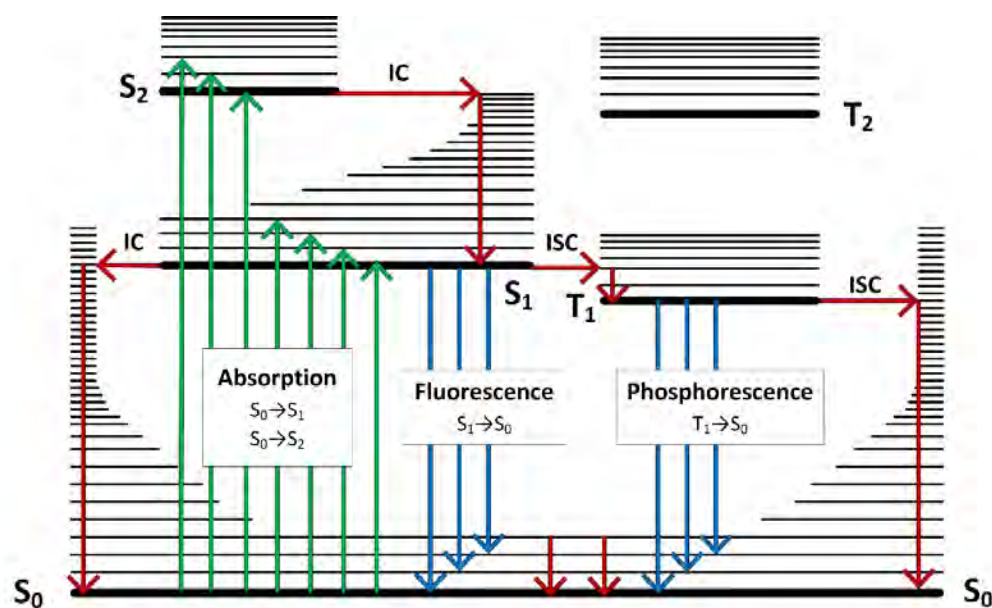
Figure 3.6. The Perrin – Jablonski diagram. The red arrows represent non-radiative transitions [150].

3. 2. 5. 3. Radiative and nonradiative transitions between electronic states

Internal Conversion

If a non-radiative transition between two electronic states of the same spin occurs, it is internal conversion. However, the molecule whose energy is internally converted eventually undergoes vibrational relaxation to the final electronic state. In the solution, the collision of excited molecules and solvent molecules can take the additional vibrational energy of this process. When a molecule is excited to vibrational energy higher than S_1, internal conversion and vibrational relaxation towards the S_1 are the possible processes. From S_1 to S_0, the internal conversion is still possible but inefficient compared to S_2 to S_1 because there is a large energy difference between S_1 and S_0. Therefore, the internal conversion is the competitor of fluorescence emission of photons in the pathway of S_1 to S_0 or intersystem crossing to the triplet state from which phosphorescence is probable to occur [150].

Fluorescence

The emission of photons that accompanies S_1 to S_0 relaxation is fluorescence. One major characteristic of molecular fluorescence is that the emission wavelength is independent of excitation wavelength because the emission happens from S_1. From the comparison between fluorescence and absorption spectra, it is known that: 1) the fluorescence spectra look like the first absorption band because the vibrational levels are similar. 2) The fluorescence spectra are at lower energy (higher wavelength) than the absorption as some vibrational relaxations can cause energy loss in the excited states. The photons emit as quickly as being absorbed, but excited molecules stay in the S_1 state for some time before undergoing any de-excitation processes. Therefore, after application of a short pulse of light, the intensity of fluorescence reduces. In this

fashion, the average lifetime of the molecule in the excited state can be measured [150].

Intersystem Crossing

Intersystem crossing is a non-radiative de-excitation process between two vibrational levels of the same energy but electronics states of different multiplicities. For instance, transition from excited molecules in the 0 vibrational level of S_1 towards T_1 triplet states is intersystem crossing. This de-excitation process could be a competitor of the other pathways such as fluorescence and internal conversion. For intersystem crossing to happen, spin inversion of electron in the excited state of S_1 is necessary as crossing between two states of different spin multiplicity is theoretically forbidden. Intersystem crossing may occur due to increase of radiation density. The increase of radiation density for a particular wavelength can enhance absorption to the point that population of upper and lower levels become identical. For photon emission, it needs to be greater population in the upper state than in the lower state [150].

Phosphorescence

From mechanistic photochemistry point of view, the term phosphorescence is reserved to refer to luminescence involving change in spin multiplicity characteristically from triple to single electronic states. Interestingly, the concept of spin multiplicity for distinction of phosphorescence is not applied for quantum dots and metallic nanoparticles. Despite that, the term "fluorescent quantum dots" is commonly used in the literature. on the other hand, there is a temperature-based distinction between fluorescence and phosphorescence that is not applied for organic species. In semiconductors, illumination of light to the material creates electron-hole pairs. If the electron-hole pair recombines straightaway, the emitted light is fluorescence, but if

they recombine after being trapped in some metastable states of energy, the emitted light is of phosphorescence.

It was once common belief to consider fluorescence and phosphorescence of the same nature. Antoine Henri Becquerel, the first person to discover evidence of radioactivity, believed that the term fluorescence should be abandoned as he imagined that fluorescence was just short-lived phosphorescence. Today, the distinction between fluorescence and phosphorescence is not based on the duration of emission as there exists long-lived fluorescence and short-lived phosphorescence [150]. The emission of light due to transition of electrons from the triple excited states to the ground state in which the spin orientations of the two levels are the same, is simply phosphorescence. The phosphorescence lifetime is in the range of milliseconds as the emission rate is slow for such forbidden transitions.

In solution at room temperature, non-radiative de-excitation from triple states may prevail the radiative phosphorescence. Many collisions may prefer intersystem crossing and vibrational relaxation in S_0 during this slow process of phosphorescence. On the other hand, low temperature and solid medium can provide the conditions to observe phosphorescence up to seconds. Generally, the fluorescence spectrum is positioned at shorter wavelengths than phosphorescence.

Delayed Fluorescence

Delayed fluorescence is a rare phenomenon in which an excited molecule in triple states, where phosphorescence emission is supposed to happen, goes back to the excited singlet state, and fluoresce. Delayed fluorescence of thermally activated intersystem crossing from T_1 to S_1 is probable to happen when the difference in energy between S_1 and T_1 is small and the lifetime of T_1 is comparatively long. Emission with the same spectral features of normal fluorescence is the result of this process.

However, the decay time is way more extended than normal fluorescence as the excited molecule stays in the triple states before radiative transition from S_1 [150].

3. 2. 5. 4. Emission and excitation spectra

Quenching

Reduction of fluorescence intensity is termed quenching. It can be due to physical or chemical processes. Energy transfer, charge transfer or photochemical processes are of the other mechanisms that can cause reduction in fluorescence intensity. Quenching is generally categorized into two types of static and dynamic. The dynamic or collision quenching is when the excited fluorophore contacts with a molecule which provides the pathway for nonradiative transition to the ground state. Oxygen species are common quenchers in this regard. Static quenching may happen when the fluorophore develops a stable complex with a non-fluorescent molecule leading to the de-excitation to the ground state [149].

Emission spectra

The emission spectrum is simply a plot of fluorescence intensity versus wavelength or wavenumber. It exhibits the distribution of the probability of transitions from the lowest vibrational level from S_1 to vibration levels of S_0. This plot is important to researchers in a few respects. For example, the plot is useful in analytical sensing. In this instance, a comparison between the fluorescence intensities of different samples can help us determine how much of fluorescence material is there. Alternatively, the change of intensity with the addition of a target analyte is useful information for many sensing applications. In binding of some fluorophore molecules with ions, a notable change in the shape of the spectrum can be observed. The emission spectrum can also give us insight into the local environment surrounding the fluorophore. The emission spectra is also informative about the local environment that surrounds the fluorophore. Some

fluorophores show redshift in their emission spectrum when the polarity of their solvent increases [149].

Excitation spectra

The excitation spectrum plots the variation of fluorescence intensity versus the excitation wavelengths for a fixed emission wavelength. The excitation spectrum comparatively measures the efficiency of different wavelengths to stimulate a particular fluorescence wavelength. The excitation spectra is supposed to be the mirror image of the absorption spectra if only one species exist in the ground state. In other words, if the excitation and absorption spectra do not match, it indicates that the fluorophore is not pure, and there may be other species in the ground state. Another possibility in this situation is that there may be sole species in the system but in different forms, such as aggregates or complexes. To record the excitation spectra, the instrument maintains the emission on a constant value by fixing the emission monochromator or appropriately filtering it while the excitation monochromator is scanned [149].

Excitation Emission Matrix

This advanced scanning method comprises the acquisition of emission spectra as a function of excitation wavelengths or vice versa. The acquired excitation-emission data are then depicted on 3D plots. Considering that each fluorophore can exhibit different excitation or emission spectra, the obtained matrix of intensity value over the excitation-emission wavelengths is unique. The EEM of each fluorophore can be used as the fluorescence signature to identify the fluorescence components in a mixture [149].

Stokes shift

The difference between the position of the first absorption band maximum and the fluorescence spectrum maximum is Stokes shift. The Stokes shift can give us insight into the excited states. The larger the dipole moment of a fluorescent molecule in the excited state, the greater the Stokes shift increases with solvent polarity. In other words, this characteristic can be employed as a fluorescence probe to measure polarity. Technically speaking, the detection of fluorescent species of large Stokes shift is more straightforward [150].

Inner filter effect

In high concentrations of fluorescence compounds, the measurement is prone to the inner filter effect, which can reduce the fluorescence intensity. Reabsorption of photons emitted at wavelengths between the overlap of absorption and emission spectra is more probable to occur at high concentrations. The inner filter effect changes the spectrum and intensity of the emitted light. Therefore, samples of high optical density should be diluted to obtain meaningful results as this effect can result in spectral distortion or even complete loss of signal [150].

Cuvettes

Cuvette is a small container of known size made of transparent material used for optical spectroscopic measurements. The fluorescence cuvettes are polished on four sides, but the absorption cuvettes may only be polished for two opposing sides. Glass, quartz, and plastic are the common materials used for manufacturing cuvettes. High-quality quartz can transmit down to the ultraviolet wavelengths (200 nm), glass can transmit to about 330 nm, and good plastic cuvettes can transmit down to 350 nm. Obviously, the choice of cuvettes depends on the type of application. Another consideration is the pathlength of the cuvette. The 1 cm pathlength cuvettes are

traditionally the very common type, which fit into almost all sample compartments of different fluoroscope machines [149].

3. 2. 5. 5. Instrumentation

Modern fluorescence instruments have been in use for more than fifty years. In their early days, fluorescent instruments were attachments of spectrometers to reflect the emitted light from the vaporization of mercury onto monochromators. It was the work of Robert Bowman at the National Institutes of Health at the beginning of 1950s that encouraged the generation first commercial spectrofluorometers with monochromators and quartz optics. Technological advancements in optoelectronics in recent decades has significantly improved the limit of detection of fluorescent materials to the point that femtomolar or even single molecule measurements are feasible.

Light source, light selection devices and light detector are the basic components needed to observe fluorescence. The role of light selection devices such as filters or monochromators is to isolate the emission spectra from the excitation wavelengths, but these devices are not ideal. One common approach to filter the excitation light in the emission spectra is to utilize a 90° angle between the excitation and detection directions.

The terms *fluorometer* and *fluorimeter* are widely used interchangeably but refer to slightly different concepts. Enrique Gaviola labelled the instrument he used for measuring fluorescence lifetime as fluorometer while steady state fluorescence spectrometers sHall be named fluorimeters [149].

Modern fluorescence instruments comprise of the following components [149]:

1. Light Source

Light emitting diodes, xenon arc lamps and lasers are the types of light sources used in fluorescence and absorption spectrometers. The range of wavelengths that these light sources can provide is of great importance in their application. In the last few years, LEDs and laser diodes have replaced xenon lamps in spectrometers due to the advantages that they can offer.

2. Optical Filter

Optical filters selectively transmit light of different wavelengths depending on the application. Generally, they are categorized into long pass, bandpass and interference filters. Long pass filters only pass long wavelengths and block all wavelengths below a certain range. Short pass filters allow short wavelengths to pass. Bandpass filters would allow a certain range of wavelengths to get through them. Excitation and emission filters are bandpass filters that are utilized for selection of excitation wavelengths or collection of desired emission wavelengths.

3. Monochromator

A monochromator is designed to transmit a narrow selectable band of wavelengths of light chosen from a wider range of wavelengths available at the input. Prisms were used in early monochromators to disperse the input light. However, nonlinearity of the light dispersion of prism-based monochromators was a major hindrance. Moreover, if UV light was required to pass, costly quartz prisms must be employed as the conventional glass prisms do not pass under wavelengths of 340 nm. So, it is no surprise that grating-based systems are widely utilized instead.

It is good to know that wavelengths selection mechanism in monochromators is not precise. For instance, at certain settings of the monochromator, a range of wavelengths are transmitted. The full-width half maximum (FWHM), that is the full-width of the wavelengths range at half of the maximum intensity, defines the quality of

a monochromator. Another aspect that should be considered is the stray light which sometimes finds its way to transmit through monochromator. Such peaks of stray light are referred to as Rayleigh Ghosts.

4. Polarizer

A polarizer is an optical filter that allows light waves of one particular polarization to pass through and blocks light waves of other polarization. Glan–Taylor calcite polarizers which feature an air gap between the two calcite crystals and allow transmission far into the ultraviolet, are widely utilized in modern optical spectrometers.

5. Detector

Despite the fact human eyes can only see the narrow wavelengths range between 380–720 nm, visual observation is still an effective method to detect fluorescence. For precision measurements, it is required to use photodetection tools such as photomultipliers. Their working mechanism is based on the photoelectric effect. A suitable photosensitive material can discharge photoelectrons after being impacted by the incident light. These electrons are of great use for intensity measurement of the input light. The sensitivity of photodetectors can be improved by setting up a series of photosensitive plates, each plate having a net positive charge compared to the previous one. These electronic devices named photomultipliers tube (PMD) amplify the impact of the incident light in multiple stages. Avalanche photodiodes (APD) are the solid-state counterparts of PMD. Another popular solid-state photodetector is charge-coupled device (CCD), which consists of an array of linked or coupled capacitors that can build up the electrical charge proportional to the incident photons from the projected image. The inherent intensity and exposure time determine the level of accumulated charge. After completion of the exposure, the obtained data is read-

out and converted to a digital value. Each assigned value contains information about a pixel which results in construction of the projected image.

3. 2. 5. 6. Common errors in sample preparation

One of the very common errors in sample preparation step is when the sample is too concentrated. In this case, the light is absorbed on the surface and, the observed signal at the detector is small. Contamination of the sample with particles and/or fluorescence impurity is another source of error. If the sample is contaminated with particles, they may drift along the laser beam and scatter. This can cause fluctuations in signal intensity as it looks too noisy. When the sample is contaminated with fluorescence impurity, the detected signals may get distorted by Rayleigh or Raman scattering. It is always good to consider that there may be more than one fluorophore in the sample under test. Having known that the emission spectra is independent of the excitation wavelengths, examining the emission at different excitations is helpful to find out if the sample contains more than one source of fluorescence [151].

3. 2. 6. Quantum yield measurement

The fluorescence quantum yield is one of the most important characteristics of a fluorophore. Definition of quantum yield can be the ratio of the number of photons emitted to the number of photons absorbed:

Quantum Yield = Photons emitted as fluorescence/Photons absorbed

Simply, if a fluorescence solution absorbs 100 photons and emits 20 photons, the quantum yield of that solution is 20%. This ratio is valid when the sample is under steady-state illumination with no energy loss, whereas the energy loss of the Stokes shift in calculation of quantum yield is required. Taking the Stokes shift into account, the emitted light is almost always lower in energy than the absorbed light. In other words, considering the energy differences, it can be said that even a perfect emitter

would have a quantum yield of less than one. Materials of large quantum yield such as rhodamines with values close to one display bright emission. The quantum yield could depend on the excitation wavelengths though such dependency cannot be found in most fluorescence materials [149]. So, quantum yield is a definitive characteristic of a fluorophore, considering that we know the temperature.

Theoretically, the quantum yield is given by

$$QY = \frac{\Gamma}{\Gamma + K_{nr}}$$

Where Γ is the emissive rate of the fluorophore and (K_{nr}) is the rate of nonradiative decay to the ground state.

The nonradiative deactivation processes that impact quantum yield may either result in well-characterized products such as electrons, protons, radicals, or less-characterized processes that are collectively named nonradiative transitions. Dissipation of energy as heat while returning to the ground state is the characteristic of nonradiative transitions. Internal conversion and intersystem crossing are the two types of such transitions.

Accurate determination of quantum yield is a challenge. There are two methods of absolute and relative to measure this quantity. In the absolute method, the sample is placed in a sphere whose interior is covered with highly reflective material. The light emitted from the sample is omnidirectional, reflects so many times and finally reaches the detector. Therefore, all the emitted light can be collected and measured compared to the input light [149].

For general purposes, the relative method is more practiced. In this method, a fluorophore of known quantum yield that has similarity with our sample in absorption and emission patterns is selected as the standard. For example, for samples with excitations in the UV or visible range, quinine sulphate and fluorescein are usually

employed. The standard and sample solutions should be diluted to make them have similar optical densities. Measuring the emission spectra of both samples, applying correction factors, and calculating the integrated area under the spectra give the total intensity of emitted light and quantum yield can be calculated as follows:

$$QY_{sample} = QY_{standard}(I_{T_{sample}}/I_{T_{standard}})(1\_10^{OD_{standard}}/1\_10^{OD_{sample}})(n_{sample}/n_{standard})^2$$

Where the term I_T term represents the total intensity, n is the refractive index of the solutions and $(1-10^{OD})$ refers to absorbed fraction of light at the excitation wavelength. However, sometimes the term $(1-10^{OD})$ is replaced with absorbance or optical density in the literature, which is a good estimation if the optical densities are low.

Calorimetry is another approach to measure quantum yield. Basically, nonradiative transitions from the excited state that compete with light emission dissipate energy in the form of heat. In this absolute measurement technique, the generated heat, which increases the temperature of the solvent, is quantified. Quantum yields obtained through this technique are usually consistent with those measured via photometric methods [152].

3. 2. 7. Fluorescence lifetime measurements

Time-resolved measurements are of great importance in fluorescence Spectroscopy. It can provide information that is not obtainable in steady-state measurements. For example, it may not be possible to distinguish the existence of two types of fluorophores from steady-state data of absorption and emission if the two spectra overlap. Another example is to differentiate between static and dynamic quenching. In dynamic quenching, the mean decay time of the total excited state population decreases while static quenching of ground state complexes does not decrease this decay time. Resonance energy transfer can be well studied via time-resolved

measurements. There are fluorescence sensors such as calcium probes that exhibit variation in lifetime when exposed to analytes.

Knowledge of the fluorescence excited lifetime is essential for understanding many of the characteristics of a fluorophore such as quenching. The fluorescence properties of a molecule, e.g., absorption and emission, are usually investigated in population than isolation. However, modern single-photon technique instruments can do lifetime measurements in isolation. This can be done by excitation of the fluorophore thousands of times and obtaining the fluorescence decay like bulk samples.

When a fluorescence sample is excited with a very narrow pulse of light, the initial population of fluorophores go to excited states which decays with a rate of $\Gamma + k_{nr}$ as stated by

Equation 3.6.
$$\frac{dn(t)}{dt} = (\Gamma + k_{nr})n(t)$$

where $n(t)$ is the number of excited molecules at time t following excitation, Γ is the emissive rate, and k_{nr} is the nonradiative decay rate.

The excited population decay with the exponential of

Equation 3.7.
$$I(t) = I_0 \, e^{-(t/\tau)}$$

Where $I(t)$ is time dependent intensity, I_0 is the intensity at time 0. The lifetime τ is the inverse of the total decay rate, $\tau = (\Gamma + k_{nr})^{-1}$.

Generally, the sum of rates that depopulate the excited states equals the inverse of the lifetime. Lifetime can be determined by fitting the data to decay models. Interpretation of the data for single exponential decay is simple as $t = \tau$. However, many samples, in particular biological ones like proteins and membranes, show more than one decay time. These complex decays can simply originate from mixing single exponential components or even interactions of the fluorophore with its environment.

For example, if a quencher is added to a protein, it can reduce the total average lifetime as only the added residue on the surface of the protein is accessible to quenching. The intensity decay now is a double exponential:

$$I(t) = \alpha_1 e^{-t/\tau_1} + \alpha_2 e^{-t/\tau_2}$$

In this expression, the α_i values are the pre-exponential factors. One fluorophore in different environments usually shows the same radiative decay rates. The values of α_i represent the fractional amount of fluorophore in each environment [151].

There are two classic approaches to measure the excited state lifetime. The impulse response or harmonic response methods relate to the time domain and frequency domain correspondingly. Direct observation of fluorescence decay is possible in the time domain, whereas the obtained information for fluorescence decay in the frequency domain is implicit.

3. 2. 7. 1. Frequency domain

In the harmonic method, the sample is excited with a constant light source whose intensity is modulated sinusoidally. The emitted light would be modulated and have the same frequency as the excitation source but with a delay in phase. The fluorescence lifetime of the sample can be calculated from this delay. The longer the phase delay the larger the phase shift between excitation and emission and the higher the fluorescence lifetime. In the strobe technique, the intensity of the fluorescence emission is measured in a narrow time window on each pulse. The time window is moved for sampling. A fluorescence decay is constructed after adequate sampling over an appropriate range of time [148].

3. 2. 7. 2. Time domain

Irradiating the sample with pulses of light and recording the intensity of emission versus time is the basis of the time-domain method. Strobe and time correlated single

photon counting are the time-domain techniques for measuring fluorescence lifetime. In the time correlated single photon counting measurement technique, the light source, detector, and optics are adjusted in a way that no more than one photon is detected at a time. Once the photon is detected, the corresponding time is measured. The fluorescence decay curve is built upon numbers of such photon events [148].

3. 2. 7. 3. Time correlated single photon counting technique

Time correlated single photon counting is a popular approach for fluorescence lifetime measurements for both *in vitro* samples and fluorescence lifetime imaging microscopy. As suggested by the name, this method is based on counting photons.

3. 2. 7. 4. Instrumentation Details for Time Correlated Single Photon Counting

Figure 3.7 shows the building blocks of a traditional time correlated single photon counting system. The constant fraction discriminator extracts the timing from the output signal of the detector (e.g., to the emission). This extracted timing information is useful for regulating the instrument response function as narrow as possible. The level trigger processes the input sync signal (e.g., to a photon from the excitation light) for timing blocks. A simple comparator is adequate for this purpose as the sync signals are usually well-characterized. The signal from the constant fraction discriminator and the level trigger is directed to the block of time to amplitude converter, which is the heart of this electronic system. This block calculates the time difference between the two input pulses and converts this time into a voltage proportionally. The analogue to digital converter block receives the voltage signal and converts it into digital timing values. Then, these values are used to address memory locations [153].

3. 2. 7. 5. Count Rates and Single Photon Statistics

Considering that the detector and other electronics systems in a TCSPC instrument have a dead time of several nanoseconds, during which they are only capable of

processing one event, it is required to keep the probability of registering more than one photon in a cycle as low as possible.

The instrument response function summarizes the characteristics of a TCSPC measurement system. The ideal system has infinitely sharp IRF indicating for precise electronics and detector and infinitely narrow excitation pulse. The resolution of a TCSPC system highly depends on the timing uncertainty the detector causes in the process of converting a photon event into electrical signal. The excitation light is of other considerable cause of IRF broadening. Although the-state-of-art laser systems can generate very narrow pulses, it is still required to have an electrical timing reference signal for comparison with the photon signal. Electronic components may compromise on rising and falling of the electrical signal used for time measurements that is another source of IRF broadening. The total IRF is the convolution of all component IRFs. Likewise, the obtained fluorescence decay from the measurement is the convolution of the decay from the actual physical process with the IRF. Therefore, it is needed to deconvolute the resulted decay so as to extract information about the lifetime [153].
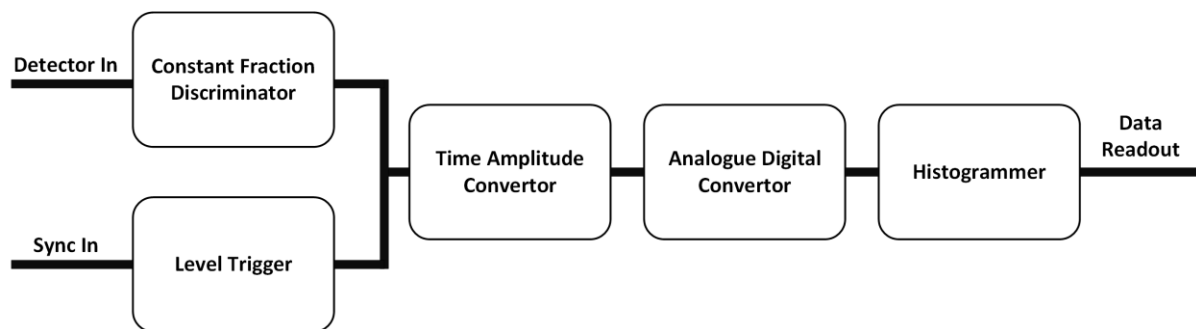
Figure 3.7. Block diagram of a traditional time correlated single photon counting system [153].

3. 2. 7. 6. Experimental Set-up for Fluorescence Decay Measurements with TCSPC

A simple setup for time correlated single photon counting measurements is illustrated in Figure 3.8 The light pulses are applied to the sample cuvette after passing the neutral density filter. The role of this filter is to weaken the light to a level appropriate for single counting statistics. The emitted fluorescence light from the sample needs to be filtered against the scattered excitation light. This is performed by means of cut-off optical filters. Thereafter, the light reaches the detector. The electrical signal from the output of the detector is fed to the electronic systems for signal processing. The electrical signal required for synchronization of photon arrival time is provided by the laser driver [153].
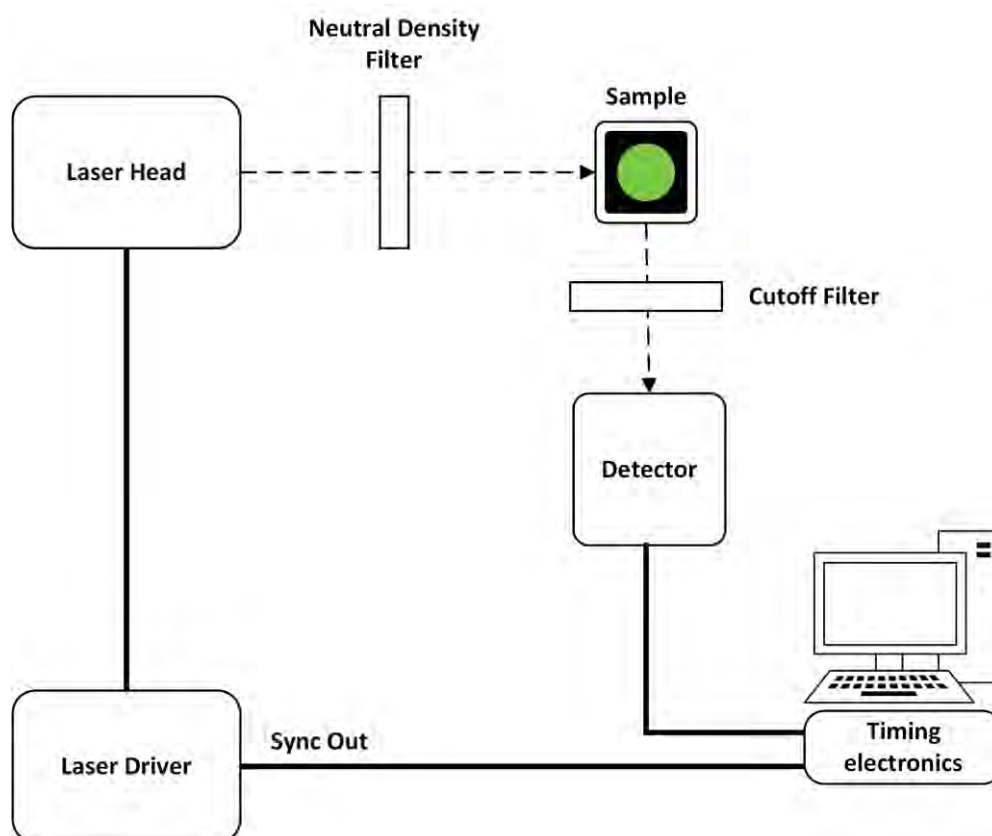
Figure 3.8. Experimental setup for lifetime measurement with single time correlated single photon counting system [153].

3. 2. 8. Hall effect measurements

The generation of a voltage difference across an electrical conductor under a magnetic field perpendicular to the flowing current is called Hall effect. Combined Hall and longitudinal resistance measurements can determine a number of material parameters [18]; carrier mobility, carrier concentration, conductivity type and resistivity. The first regular use of Hall measurements was in semiconductor industry two decades ago when characterizing bulk silicon was in high demand. Once the electronic characteristics of bulk silicon were well-quantified, this measurement technique became less popular, but today, modern semiconductor materials are no longer in bulk structure. Interestingly, Hall measurement can still be employed to study intrinsic electronic properties of novel nanomaterials. For instance, it is commonly believed that the occurrence of Hall effect in QDs is indicative of band-gap like charge transport similar to conventional semiconductors [19]. Nevertheless, there exists only a scanty number of works characterizing novel nanomaterials using Hall measurements [20, 21].

The history of Hall effect begins in 1879, when Edwin H. Hall observed that by applying a magnetic field to a thin metal strip carrying current, a small transverse voltage perpendicular to both the magnetic field and the current appears. Since then, Hall effect measurements have been proved to be a practical tool for electrical characterization of materials, in particular semiconductors. A combination of Hall and resistivity measurements can determine several materials parameters: carrier mobility (μ), carrier concentration (n), Hall coefficient (R_H), resistivity (ρ) and conductivity type (P or N). The measurement is equally useful for characterizing both low resistance and high resistance semiconductors [18].

The first regular use of Hall measurement in semiconductor industry dates to two decades ago, when characterizing bulk silicon was in high demand of scientists and researchers. Once the bulk mobility of silicon was fully comprehended, this measurement technique came out of the limelight. But the current trend and future perspective in semiconductor industry are not solely focused on silicon. Besides, modern semiconductor materials are no longer in bulk structure. Therefore, researchers may need to go back to Hall measurement to determine carrier concentration and mobility of the emerging semiconductors.

Lorentz force is the basic physical principle that underlies the Hall effect. Let us assume that a constant current flows along the x-axis under the application of a z-directed magnetic field (Figure 3.9). Lorentz force drifts a proportion of electrons away from the current direction towards the y-axis that results in excess charge in the side of the sample.
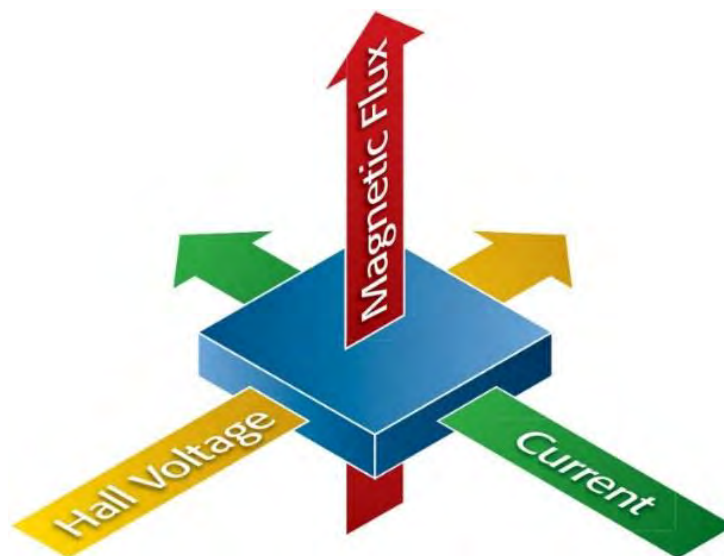
Figure 3.9. Schematic illustration of Hall effect [18].

Due to this charge, a potential drops across the sides of the sample that is Hall voltage. The magnitude of this voltage is

Equation 3.9.

$$V_H = \frac{IB}{qnd}$$

Where I is the current, B is the magnetic field, d is the sample thickness, q is the elementary charge, and n is the carrier concentration. If the sheet resistance R_S of the sample is known, the Hall mobility can be calculated through:

Equation 3.10.

$$\mu = \frac{|V_H|}{R_S IB}$$

3. 2. 8. 1. Van der Pauw technique for sheet resistance measurement

The sheet resistance of a material can be conveniently determined by the van der Pauw technique. In this technique, a current is driven along one edge of the sample, for instance I_{12}, and the voltage across the opposite edge V_{43} is measured. Schematics of van der Pauw configuration for sheet resistance measurement is shown in Figure 3.10.

$$R_{4312} = \frac{V_{12}}{I_{43}}$$

$$R_{3421} = \frac{V_{21}}{I_{34}}$$
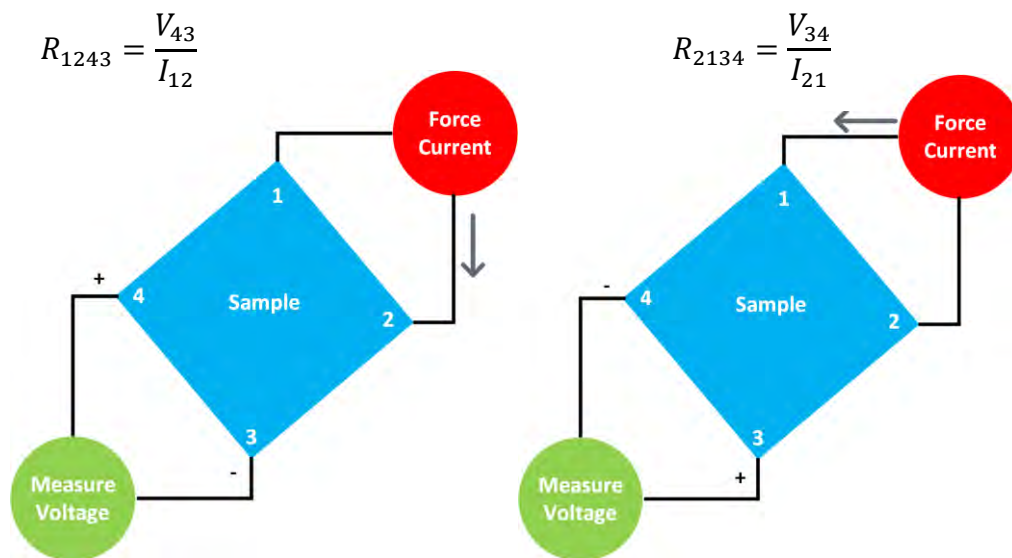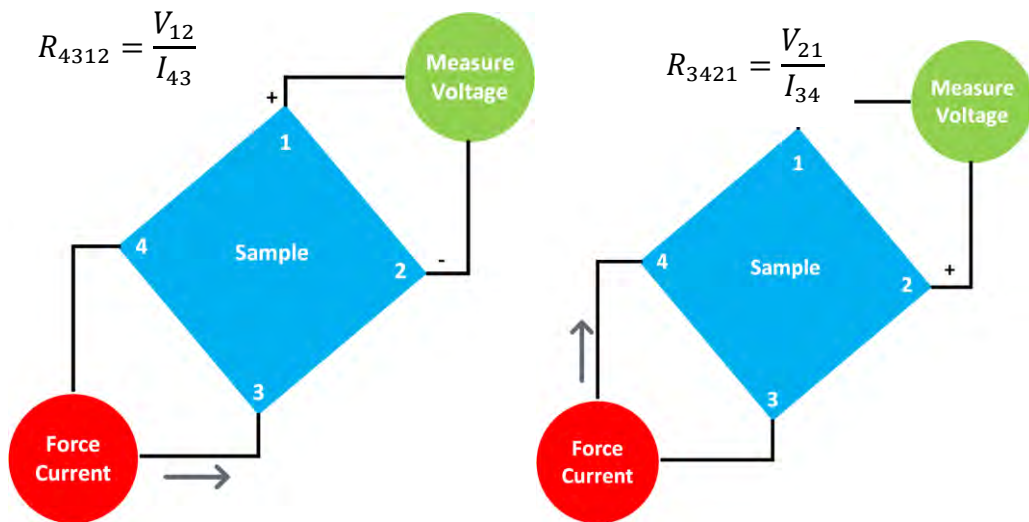
Equation 3.11.

$$R_A = \left(\frac{V_{34}}{I_{21}} + \frac{V_{43}}{I_{12}} + \frac{V_{12}}{I_{43}} + \frac{V_{21}}{I_{34}}\right)/4$$

$$R_{2314} = \frac{V_{14}}{I_{23}}$$
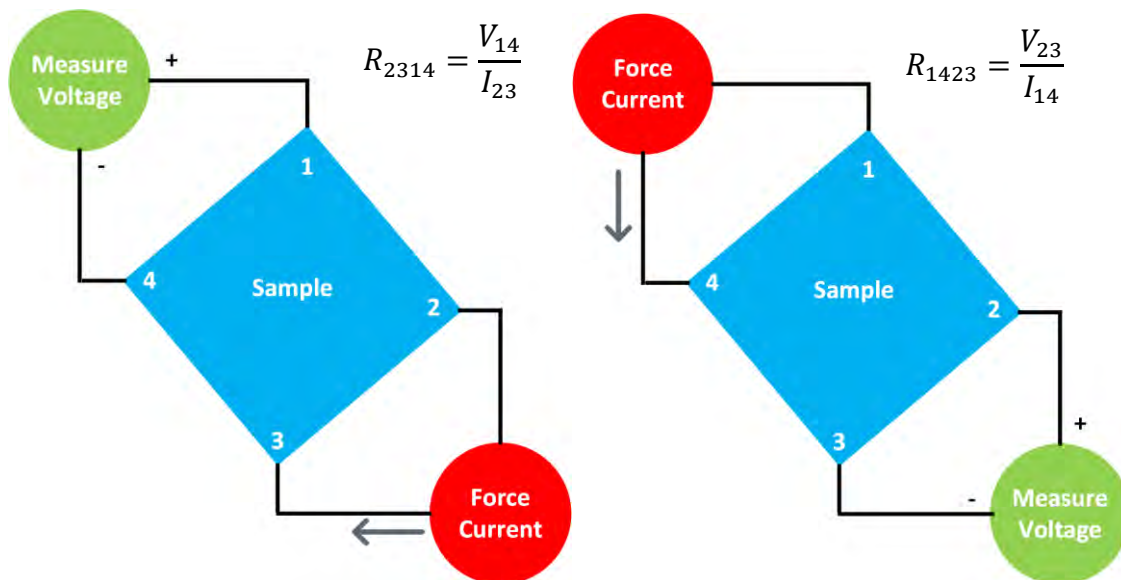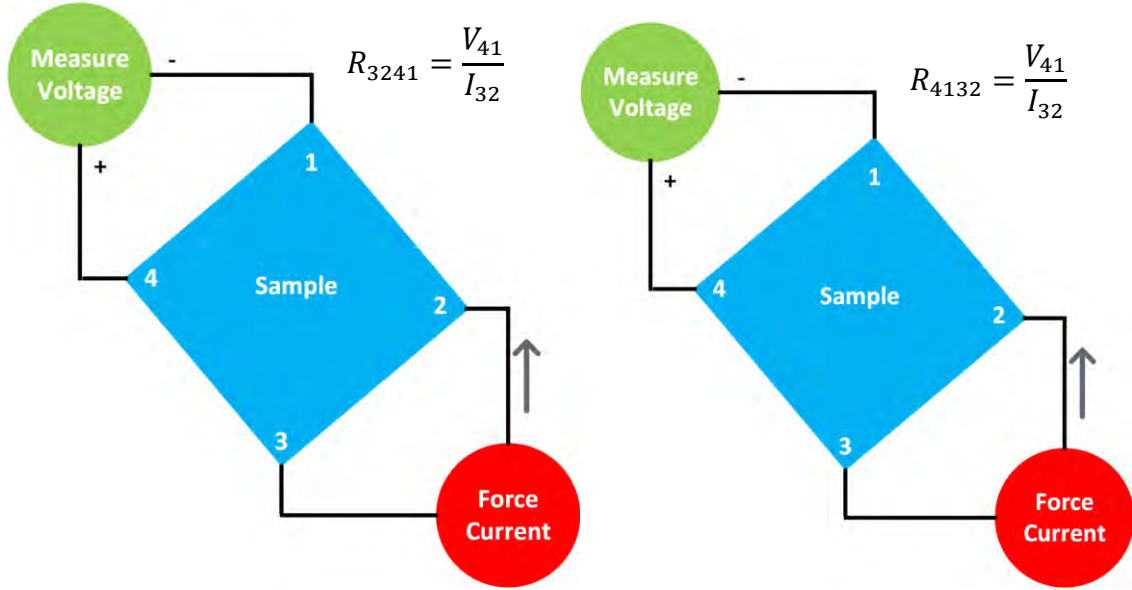
$$R_{1423} = \frac{V_{23}}{I_{14}}$$

Figure 3.10. Schematic representation of van der Pauw configuration for sheet resistance measurement.

Equation 3.12.

$$R_B = (\frac{V_{41}}{I_{32}} + \frac{V_{14}}{I_{23}} + \frac{V_{23}}{I_{14}} + \frac{V_{32}}{I_{41}})/4$$

By doing the measurement in both vertical and horizontal directions, sheet resistance can be determined from:

Equation 3.13.

$$exp(-\frac{\pi R_A}{R_S}) + exp(-\frac{\pi R_B}{R_S}) = 1$$

This equation can be solved numerically for R_S. If the sample is square shaped, we can assume that $R_A = R_B = R$, and in this case, the numerical solution for the sheet resistance equation is:

Equation 3.14.

$$R_S = \frac{\pi R}{ln2}$$

3. 2. 8. 2. Hall voltage measurement

A schematic of configuration for Hall voltage measurement is shown in Figure 3.11. For this measurement, a current is driven diagonally between the contacts at corners of the sample, for instance I_{13}, in presence of a magnetic field, and the voltage across the other diagonal V_{24} is measured. Then, the polarity of the magnetic field is reversed,

and the same measurement is carried out again. To achieve reliable results, it is recommended to source on other terminals, and reverse the polarity of current, and average all the obtained values.
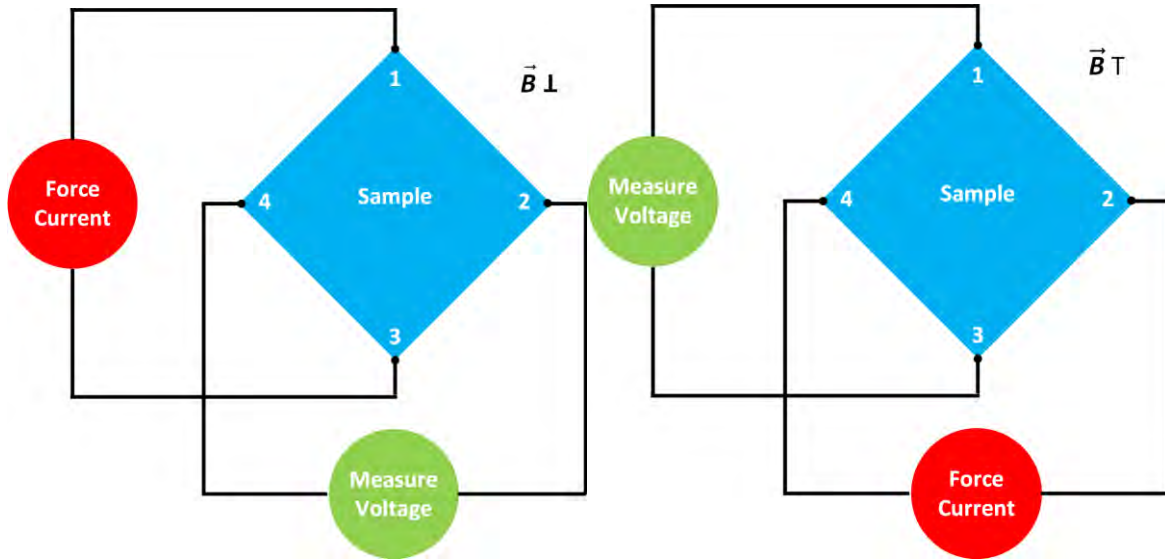
Figure 3.11. Schematic representation of Hall voltage configuration measurement.

$$V_C = V_{24p} - V_{24N} \qquad\qquad V_E = V_{13p} - V_{13N}$$

$$V_D = V_{24p} - V_{24N} \qquad\qquad V_F = V_{31p} - V_{31N}$$

Equation 3.15. $$V_H = (V_C + V_D + V_E + V_F)/8$$

3. 3. Characterization methods

The X-ray photoelectron spectra (XPS) were obtained using Kratos Axis Ultra XPS. The Fourier transform infrared (FTIR) spectra were gained utilizing Perkins Elmer Spectrum Two. Transmission electron microscope (TEM) images were taken with Hitachi HT7700 at the accelerating voltage of 120 kV. To obtain 3D fluorescence excitation-emission matrices and UV-Visible absorption spectra, a Horiba Duetta fluorescence and absorbance spectrometer was used. For fluorescence lifetime measurements, the Horiba DeltaFlex time correlated single photon counting system was employed. Hall effect measurements were performed in a in-house set up under

the magnetic field of 0.52 Tesla using Keithley 2602B source measure meter for current application and voltage measurement.

Solution samples were used for TEM imaging, absorbance, fluorescence, and quantum yield measurements. XPS and FTIR characterization and Hall effect measurements were performed on the freeze-dried samples.

For TEM imaging preparation of the samples, they were sonicated for 30 minutes in the first step. Then, the sonicated samples were further diluted by Milli-Q water. Thereafter, a drop of the diluted solutions was dripped on pieces of carbon-coated copper grids (200 mesh) and allowed to dry at room temperature.

The emission quantum yields of N-CDs were calculated using quinine sulphate (QS) as the reference. The UV-visible absorbance spectrum of QS and the sample solutions were recorded in 10 mm fluorescence cuvettes for at least five different concentrations with the maxima between 0 to 0.1. Exciting the same solutions with 340 nm, their fluorescence spectra were recorded, and the integrated fluorescence intensities were measured for each of them.

For Hall effect measurements, Piranha treated square-shaped cut pieces of glass with 10 mm sides were used as the substrate. The glasses underwent sputtering for deposition of four 100 nm thick gold contacts of 1×1 mm on each corner. Then the freeze-dried N-CDs were doctor bladed on the fabricated substrates. To minimize the electrical contact resistance, some conductive carbon paste was also dispersed over the contact area on top of the N-CDs layer. The schematic of this structure is illustrated in Figure 3.12. Thereafter, the sample substrates were placed under 0.52 Tesla magnetic field in our in-house Hall measurement setup, currents appropriately applied, and corresponding voltages measured with the source measure meter.
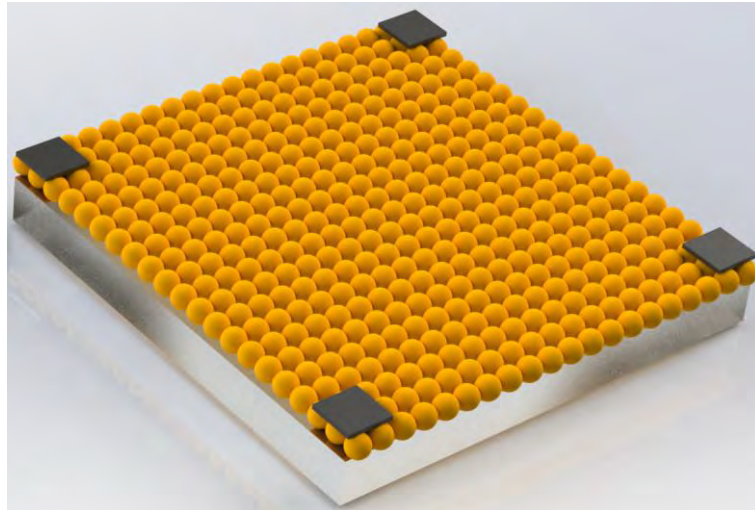
Figure 3.12. the Schematic illustration of the structure for Hall effect and resistivity measurements

Chapter 4 The effects of nitrogen doping on chemical properties of carbon dots

4. 1. XPS analysis of the N-CDs samples

To obtain quantified information about a sample, it is first needed to find peaks of the constituting elements, specify the related regions, and calculate the peak intensities. The relative amount of material in our samples is measured using three transitions of C1s, N1s and O1s, each of which appears as individual peaks in the XPS spectrum. Table 4.1 exhibits the summary of processed data for quantification of the survey spectra in Figure 4.1. The relative quantity of materials for transitions of C1s, N1s and O1s appeared as peaks in the XPS spectrum is measured and displayed based on atomic concentrations in percentages. To calculate these percentages, the area under the signal above the background is integrated. Herein, the three C1s, N1s, O1s photoelectron lines are selected because these three peaks are most intensive in the spectra and do not have any interference with any other transitions in the region. The higher the intensity of the peaks the greater the signal to noise ratio, or in other words, better precision in data acquisition. However, the real-world measurements are not ideal and, contamination from other elements, particularly SiO_2, the glass substrate on which the samples are placed during the measurement, can be observed.

We know from the FTIR that hydrogen do exist in our samples, but the XPS cannot measure hydrogen. The H1s electrons of hydrogen are technically valence electrons contributing in chemical bonding. On the one hand, the probability of valence electrons being emitted is small. On the other hand, signals from the excitation of valence electrons in other atoms largely overlap with the hydrogen aotms. The broadband appearance of signals from valence electrons in the XPS spectra is also another

reason that makes it next to impossible to discern H1s electrons from valence electrons of other elements [154].
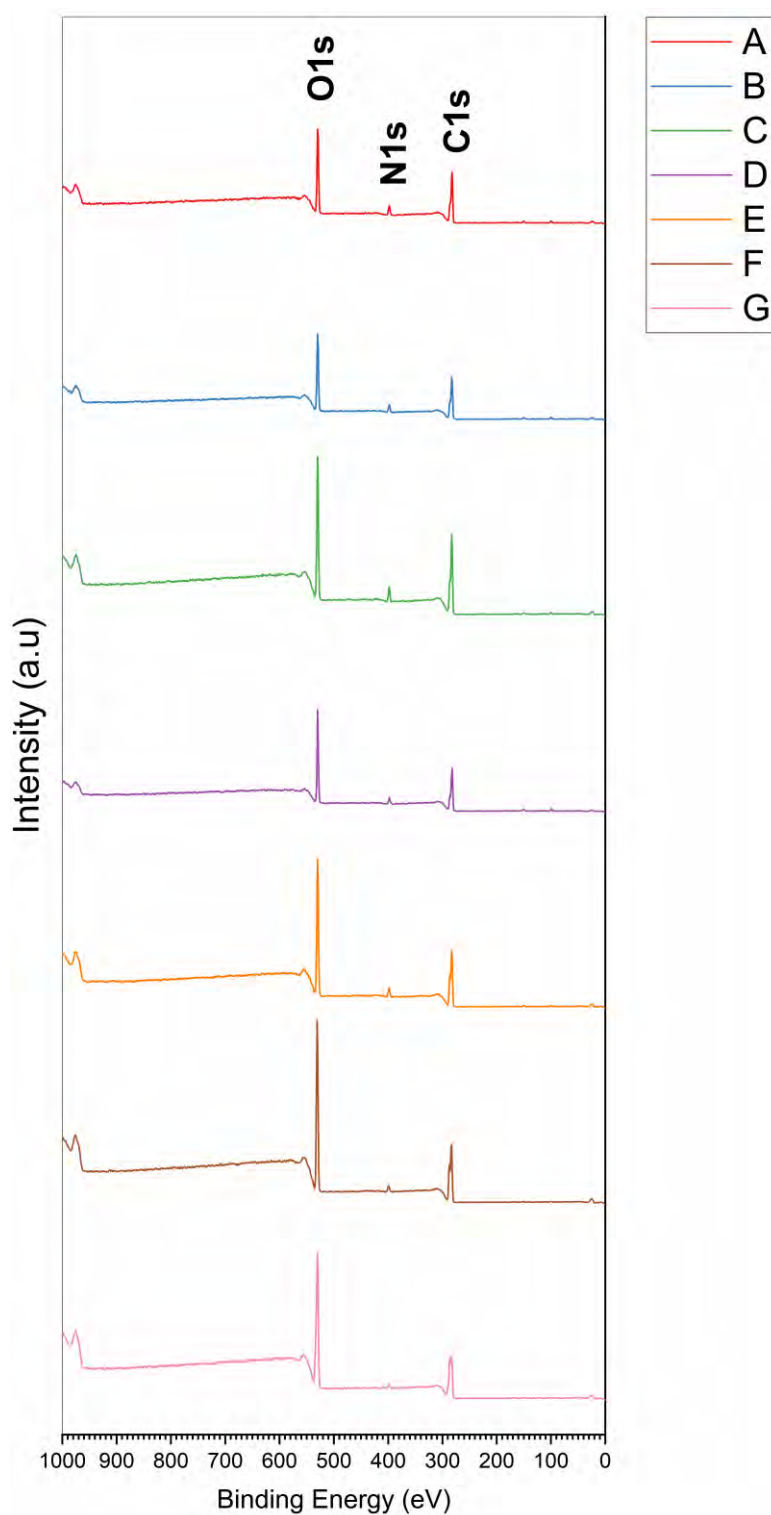
Figure 4.1. XPS survey spectra of the (A-G) samples

An important consideration when performing XPS measurements is the acquisition time. In general, XPS is an invasive technique though some materials may undergo changes when subjected to vacuum, X-ray or charge compensation mechanism. In a good experimental design, the acquisition time is minimised, especially for vulnerable materials using the survey mode.

The steps of energy in survey mode are usually optimised to shorten the time required for obtaining the data while not missing the important narrow peaks. Thereafter, high resolution is performed on the landmark areas identified by the survey. The fine energy steps in the high resolution are focused on few specified peak areas, which optimises the acquisition time for revelation of details about the material characteristics, which may not be easy to find in the survey. Recognition of chemical states of an atom in a molecule is of the advantages the narrow scan XPS spectra offers. Take C1s electrons. Depending on the element to which the carbon is bonded the binding energy varies in amplitude (Y-axis) and direction (X-axis).

Reducing the resolution of energy for the survey spectra scan is determined by changing a combination of settings of the instrument. Moreover, there is a selection mechanism for electrons leaving the sample. Therefore, the efficiency for the collection of electrons can be affected and should be adjusted accordingly. This adjustment is called transmission correction. This correction is necessary to achieve the equivalent of the atomic concentrations in high resolution to that of data from the survey, especially that not all the instruments follow a well-specified transmission function.

To remove backgrounds from the set of selected peaks in the XPS analysis, algorithms such as linear interpolation between two the defined boundaries of the peaks, Shirley background, are applied. This algorithm calculates an average background based on the intensity of the left and right boundaries of the peak. The use of such algorithms is

helpful as the data from low energy electrons in the spectra are not informative about their chemical states. Thereafter, a linear combination of Gaussian and Lorentzian functions is curve fitted into the peaks. The objective of this mathematical operation is to model the peaks based on their constituents, which finally reveals information about bonding elements of the peaks. It is sometimes inevitable to compromise on conformity of the fitted curves with these functions. To achieve optimum fittings, application of least square approximation may be necessary.

Inhomogeneity and surface contamination are factors that can influence the accuracy of the results from XPS. The obtained numbers for the atomic concentrations of inhomogeneous samples may not be representative of the true elemental composition. From the XPS viewpoint, even homogeneous samples are prone to such error. If the surface of a homogenous material gets contaminated for any reason during the sample preparation before undergoing XPS, it is highly probable to obtain erroneous results for the expected ratio of the material constituents. The layer of contamination can attenuate the signals from scattering of the electrons and consequently causes the alteration of the relative intensity of emission peaks that is used for calculation of atomic concentration.

Generally, the relative intensities of the photoemission peaks in the XPS spectra depend on the probability of emission of electrons after scattering of the photons with the atom. The emission of electrons after such incidents is dependent on which core level of the atom has changed in the final state. Therefore, one cannot expect the number of detected electrons to be correspondingly distributed between photoemission peaks for each element. They may appear with intensities disproportional to their true atomic concentration numbers. To correct the intensities, it is needed to compensate for these differences that resulted from the photoemission

process. Relative sensitivity factor (RSF) is applied when processing the data for this purpose [155].

The number of electrons that an instrument records for particular kinetic energy may be slightly different from the true number of electrons leaving the sample. The ratio of emitted electrons to the detected number of electrons may alter as a function of kinetic energy. To compensate for these variations to adjust collection efficiency, the transmission function correction is measured and applied. Transmission correction is essential in quantitative XPS measurement without which a comparison of results from different operating mode e.g. lens modes, energy resolutions, aperture settings and spot-sizes of the X-ray source is not possible. [155].

We conducted XPS analyses on the series of synthesized N-CDs to obtain information about their chemical composition. In the survey analysis, three major peaks at around binding energies of 283, 398, and 530 eV, which respectively correspond to C1s, N1s, and O1s were observed. The survey also provided us the elemental composition percentages of the N-CDs. These pieces of information are summarized in Table 4.1 and illustrated in Figure 4.1.

Table 4.1 shows that from sample G to A- lower to higher amount of urea, higher to lower citric acid to urea ratio- 1) the nitrogen content increases from 1.93% to 5.73% that is indicative of successful doping of this element into carbon. 2) the carbon content increases from 55.33% to 62.07% that is a good piece of evidence demonstrating that nitrogen doping improves carbonization though to a certain degree. 3) Oxygen content decreases from 42.74% to 29.76%.

The deconvoluted high-resolution C1s, N1s and O1s spectra of the samples are shown in Figure 4.2 to Figure 4.4. The C1s high resolution spectra contain four peaks at 284.9, 285.5, 287.5, and 289.1 eV binding energies that belong to C-C, C=C, C-H;

C-O, C-N; C=O, C=N; O=C-O bonds, respectively. A comparison of C1s peaks in all these figures can lead us to this conclusion again that nitrogen doping improves the carbonization as in samples with the greater amount of urea the ratio of areas under the curves of C-C, C=C to O=C-O ones tends to be generally higher indicating for existence of more carbon on the surface.

The high resolution N1s spectra consist of two peaks at 400 and 402 eV, which respectively corresponds to C-N pyrrolic bonds and N-H/graphitic N bonds. What can be noticed here is the higher intensity of the C-N peak relative to the N-H/graphitic N peak in samples with the higher amount of urea, which implies for prevalence of more carbon and nitrogen on these N-CDs. The high resolution O1s spectra contain two peaks at 532 and 533.5 eV, which can be attributed to C=O and C-O- C, C-OH, respectively. The trend that the ratio of the area under the C-O-C, C-OH curve to the C=O tend to grow smaller in samples with more urea indicates that fewer OH groups exist on the surface of better-carbonized samples.

Table 4.1. The ratio of the constituents of the prepared precursors and the elemental composition percentages of their corresponding N-CDs from the XPS survey. A-G labels in this table that refer to the obtained N-CDs samples are used for their naming in further experiments.

Sample name	A	B	C	D	E	F	G
Citric acid	5.25 g						
Urea	0.89 g	0.69 g	0.59 g	0.47 g	0.32 g	0.164 g	0.082 g
CA/Urea molar ratio	2	2.375	2.75	3.5	5	10	20
Carbon	62.07%	61.1%	62.1%	60.1%	57.6%	56.2%	55.3%
Nitrogen	5.73%	5.2%	5.16%	4.89%	4.54%	2.69%	1.93%
Oxygen	29.76%	31.3%	31.6%	32.5%	37.0%	40.5%	42.7%
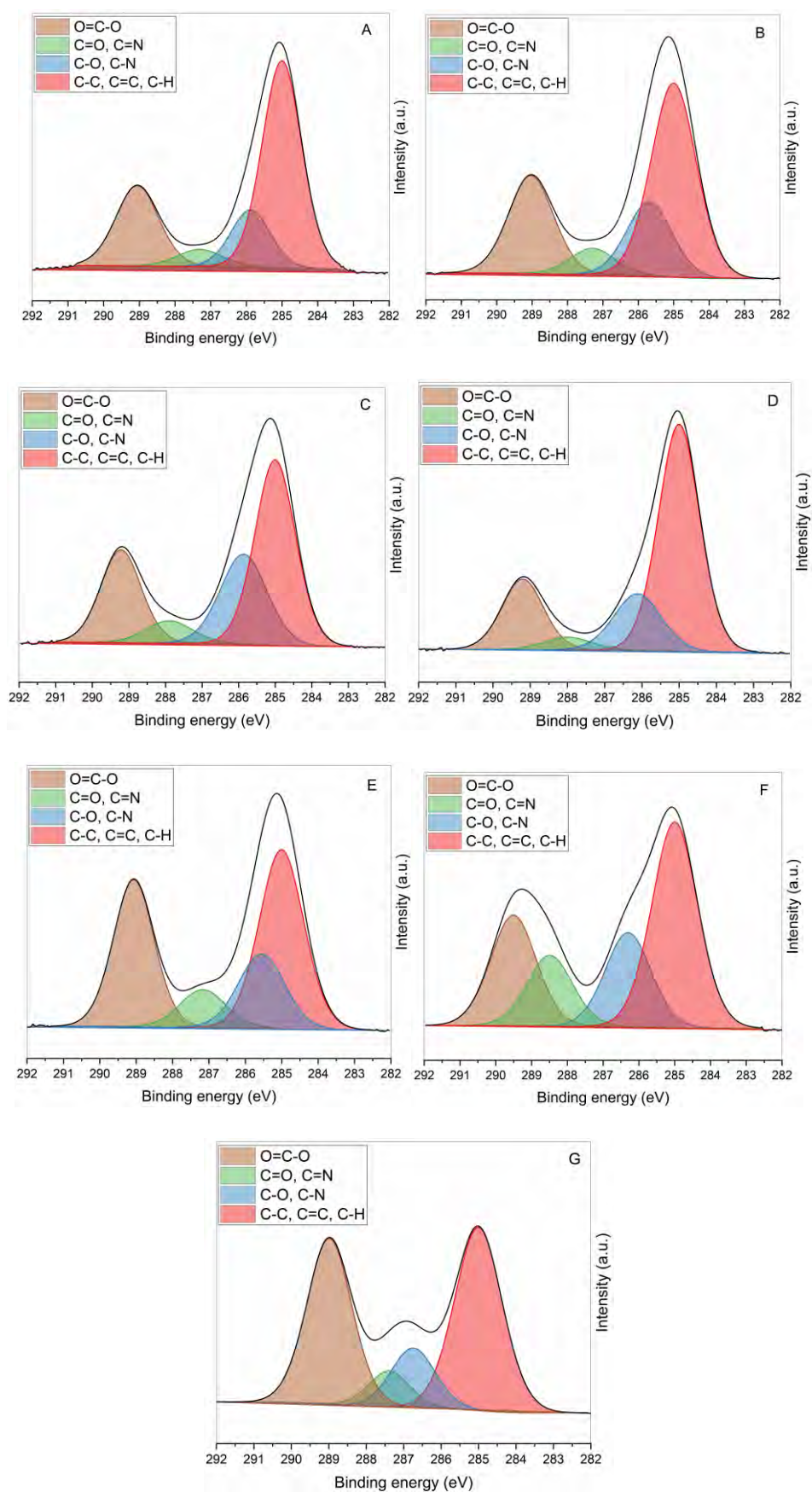
Figure 4.2. Deconvoluted high-resolution C1s spectra of samples A-G.
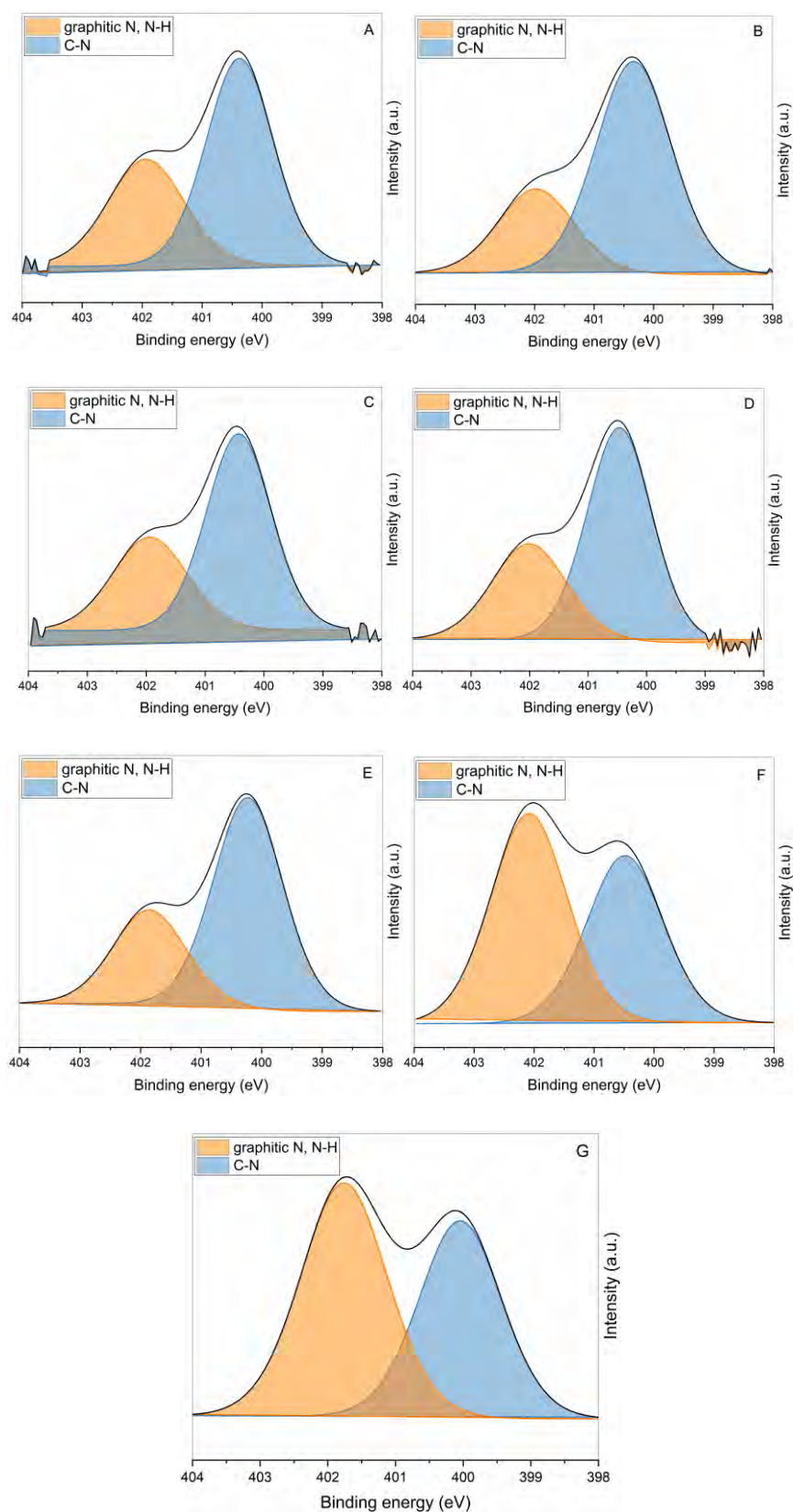
Figure 4.3. Deconvoluted high-resolution N1s spectra of samples A-G.
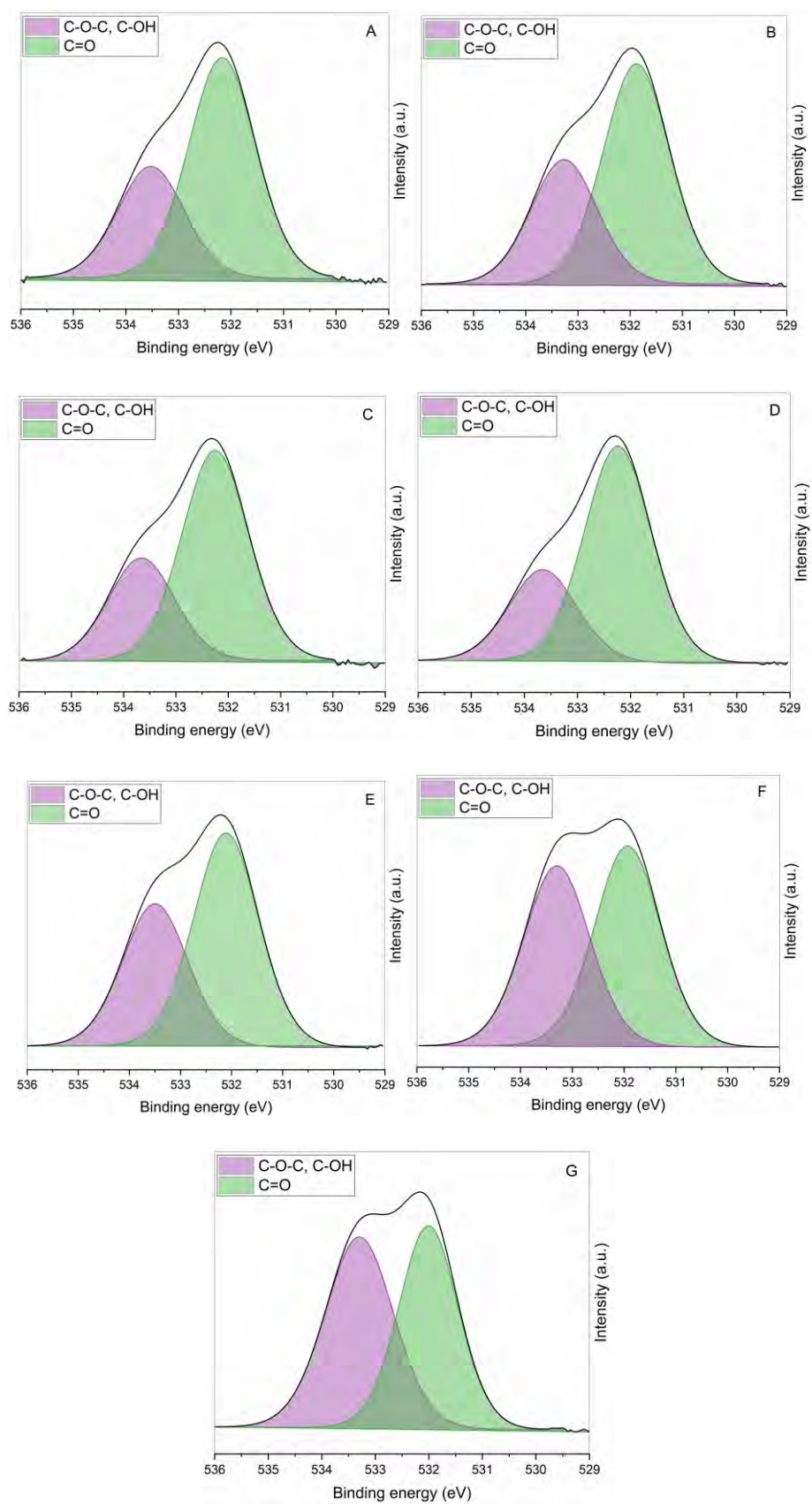
Figure 4.4. Deconvoluted high-resolution O1s spectra of samples A-G.

4. 2. FTIR analysis of the N-CDs samples

Figure 4.5 presents the FTIR spectra of the seven N-CD samples. IR characteristic peaks of the following stretches can be seen in these spectra: 785 cm^{-1} (NH stretch), 1174 cm^{-1} (C-O stretch), 1398 cm^{-1} (C-O stretch), 1557 cm^{-1} (C=C stretch), 1655 cm^{-1} (C=N stretch), 1700 cm^{-1} (C=C stretch), 2982 cm^{-1} (CH stretch), 3284 cm^{-1} (OH stretch) and 3495 cm^{-1} (NH stretch). The presence of amine (785 cm^{-1}), amide (1700 cm^{-1}, 3495 cm^{-1}), imine (1655 cm^{-1}), alkane (2982 cm^{-1}), carboxylic acid (1174 cm^{-1}, 1398 cm^{-1}, 3284 cm^{-1}) and aromatic carbon (1557 cm^{-1}) functional groups can be established from the FTIR spectra.
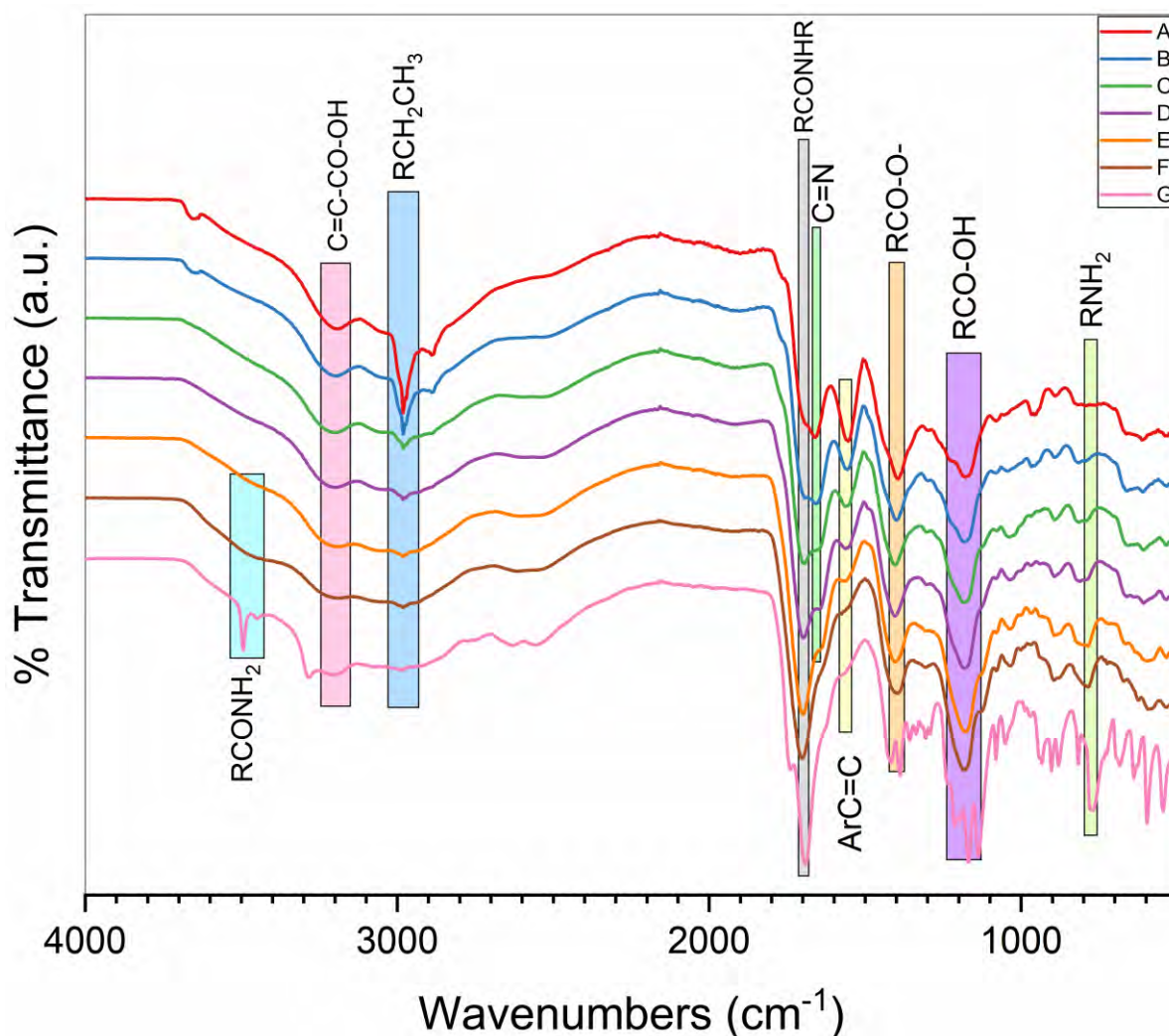
Figure 4.5. The presence of different functional groups in FTIR spectra of samples A-G

A few trends can be extracted from the comparison of the FTIR spectra of the N-CDs; from sample G to A (lower to higher nitrogen content), 1) the intensity of the peak attributed to C=C gradually increases, which is another evidence that nitrogen doping results in better carbonization. 2) The amines and amides peaks gradually disappear. Instead, a new peak belonging to C=N stretch of imines comes into view that is another evidence for successful doping of nitrogen into carbon 3) carboxylic acid peaks tend to remain unchanged in all the N-CDs.

4. 3. Transmission electron microscopy images of the N-CDs samples

The TEM images of the seven samples presented in Figure 4.6 to Figure 4.12 show that the produced particles are well-dispersed withing the size distribution of 2-5 nm without any noticeable trend among the samples. Although the single particles are within the range of typical dimension of CDs, they tend to assemble into aggregates in larger clusters even in very diluted solutions. Considering evidences for narrow distribution of electronic transitions in infinitely diluted CDs [10], these aggregates can be introduced as a governing parameter in photoluminescence of CDs.

As is seen in the TEM images, sample A which has the highest amount of urea in the precursor shows the best crystallinity compared to the other samples. It indicates that urea facilitates formation of crystalline CDs. In samples B to G, where the amount of urea decreases in the reaction, CDs tend to be amorphous without any specific trend in their morphologies. However, our most important observation here is that all the N-CDs samples tend to aggregate in clusters.
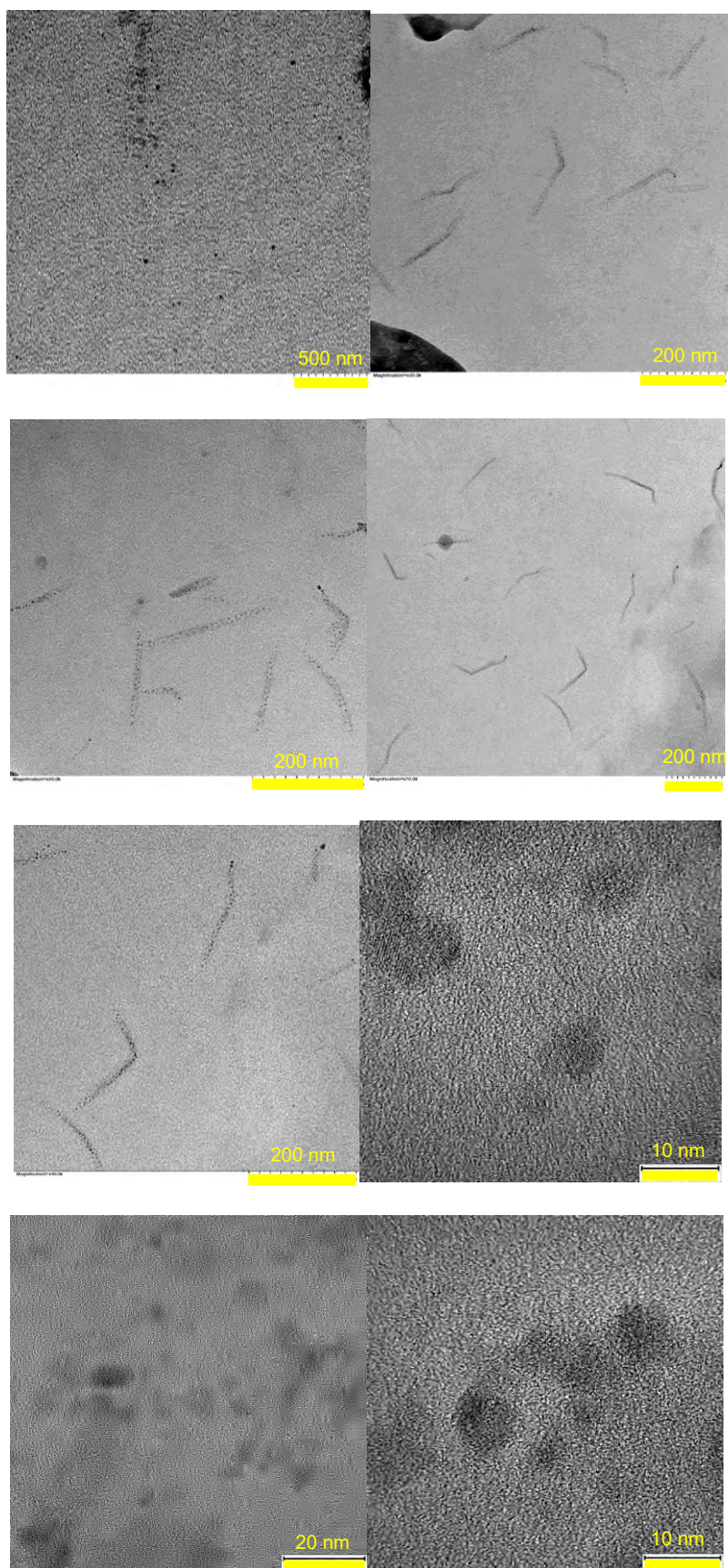
Figure 4.6. TEM images of sample A
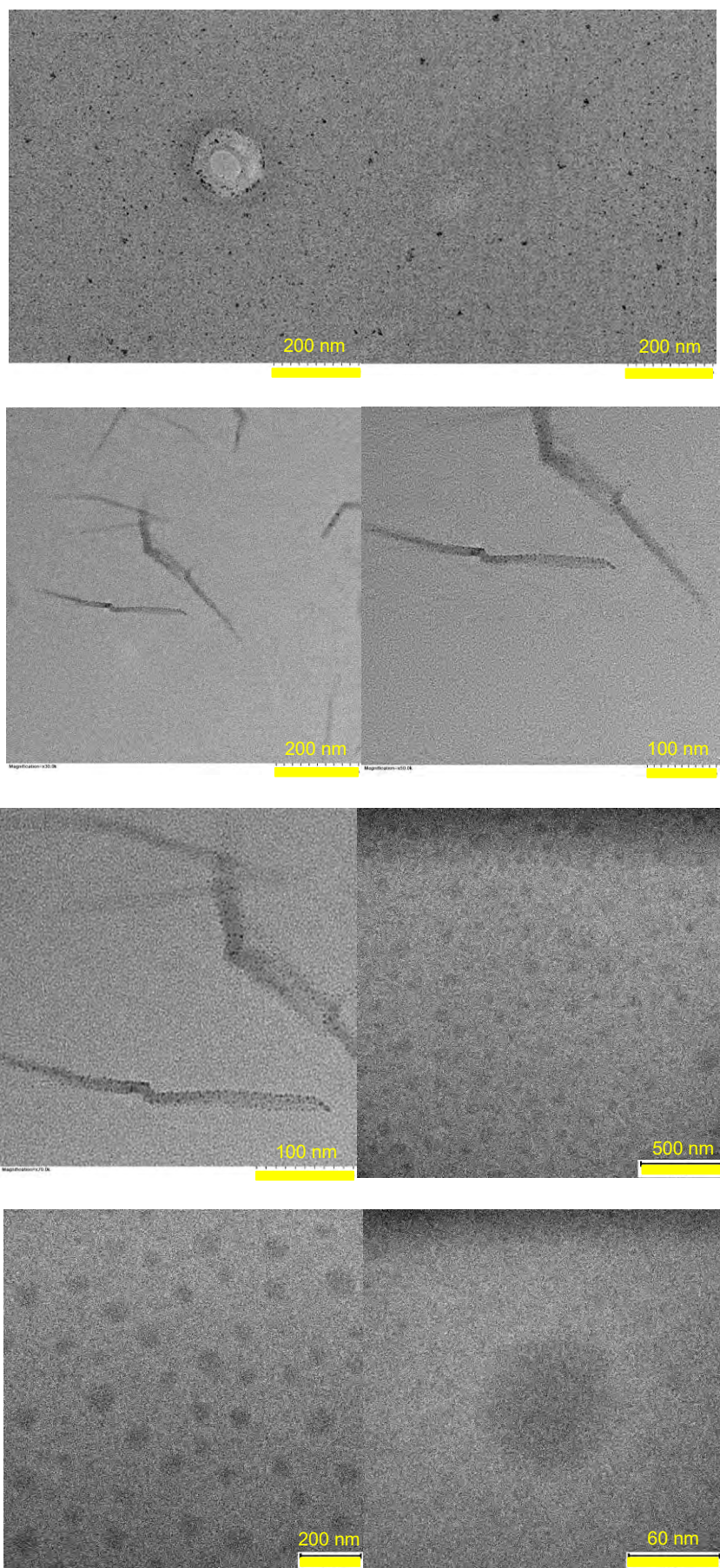
Figure 4.7. TEM images of sample B
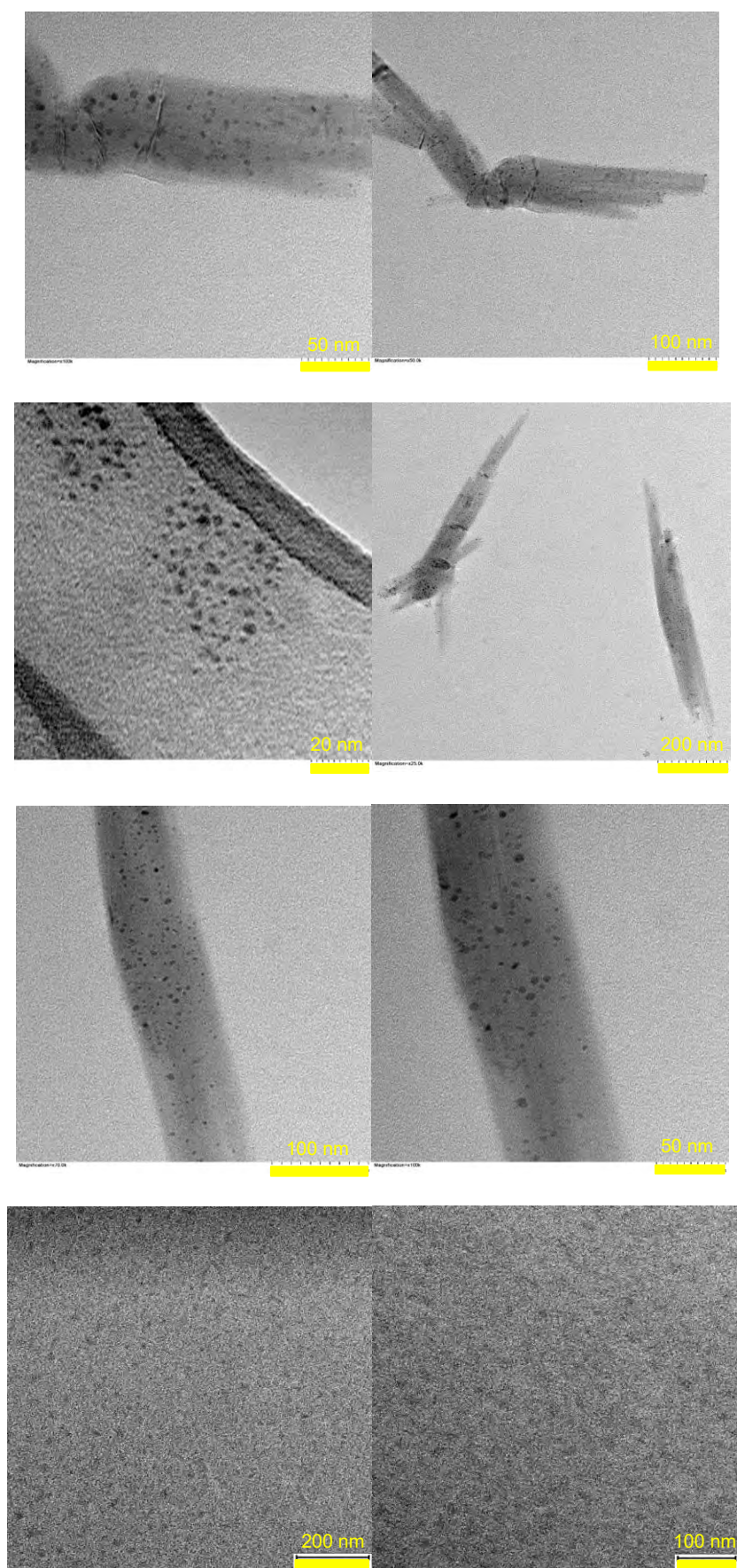
Figure 4.8. TEM images of sample C
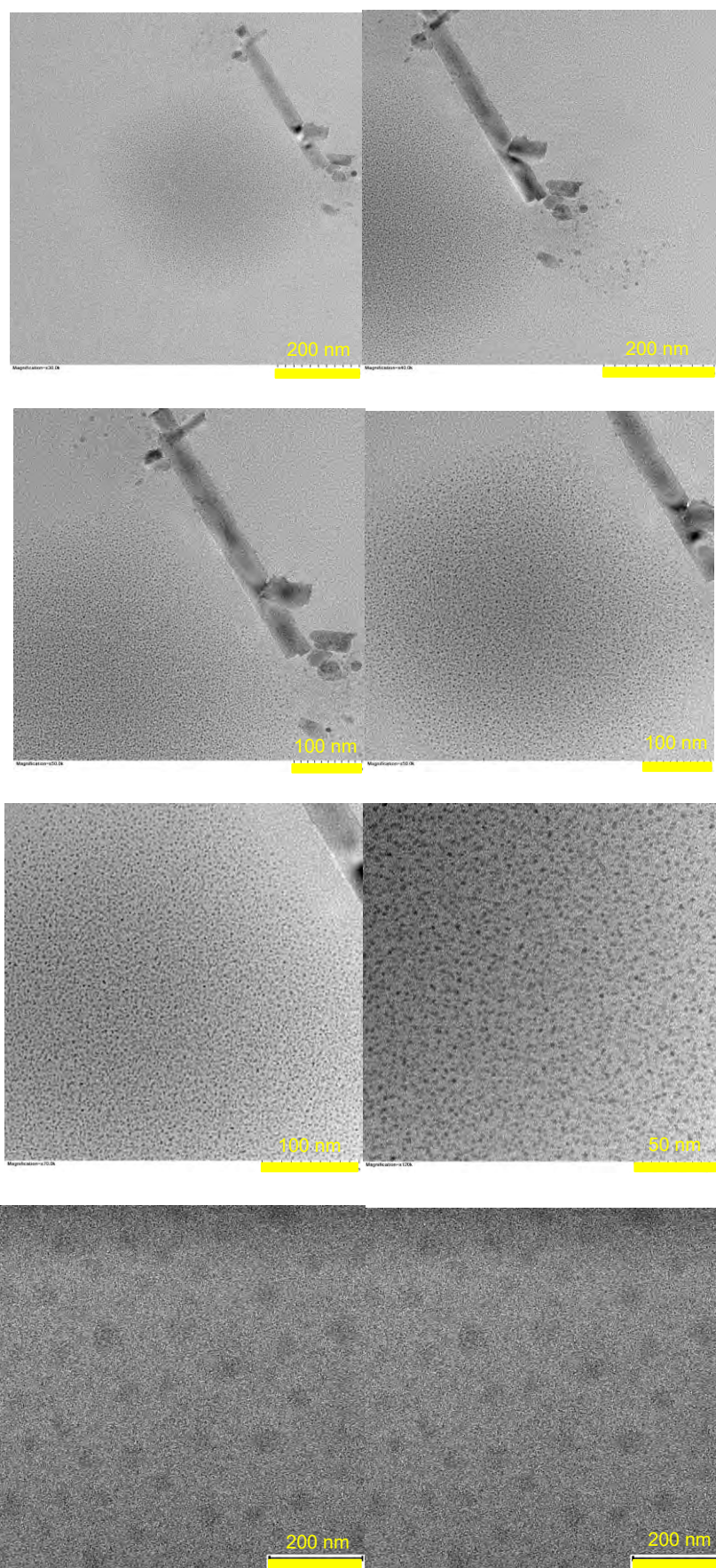
Figure 4.9. TEM images of sample D

Magnification=x60.0k

100 nm

Magnification=x40.0k

200 nm
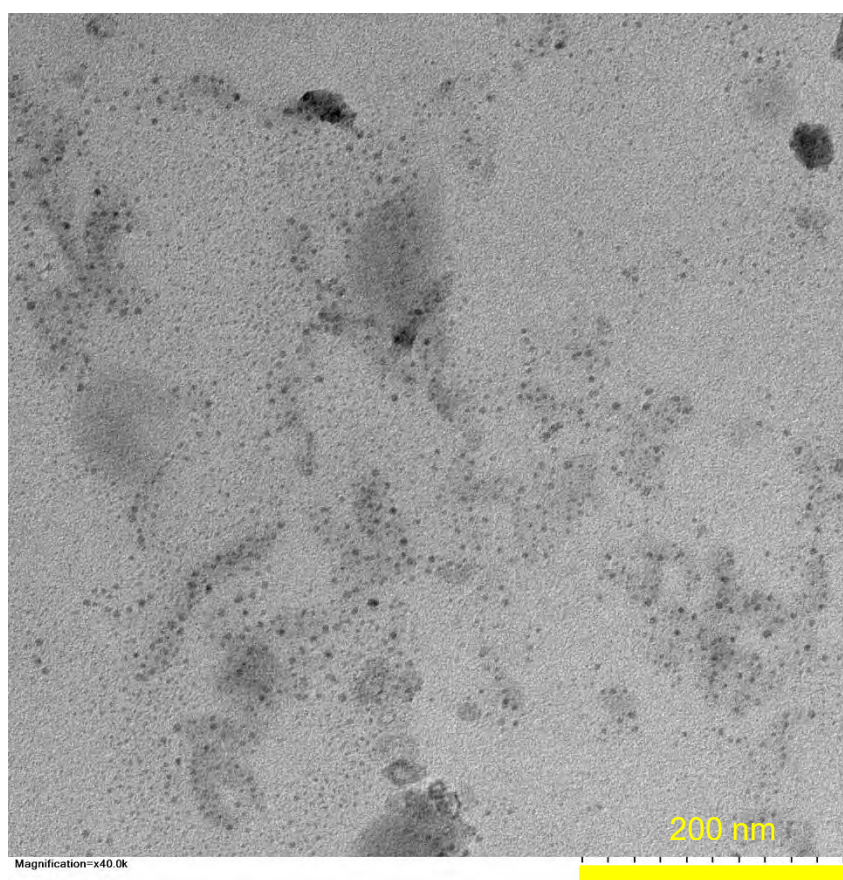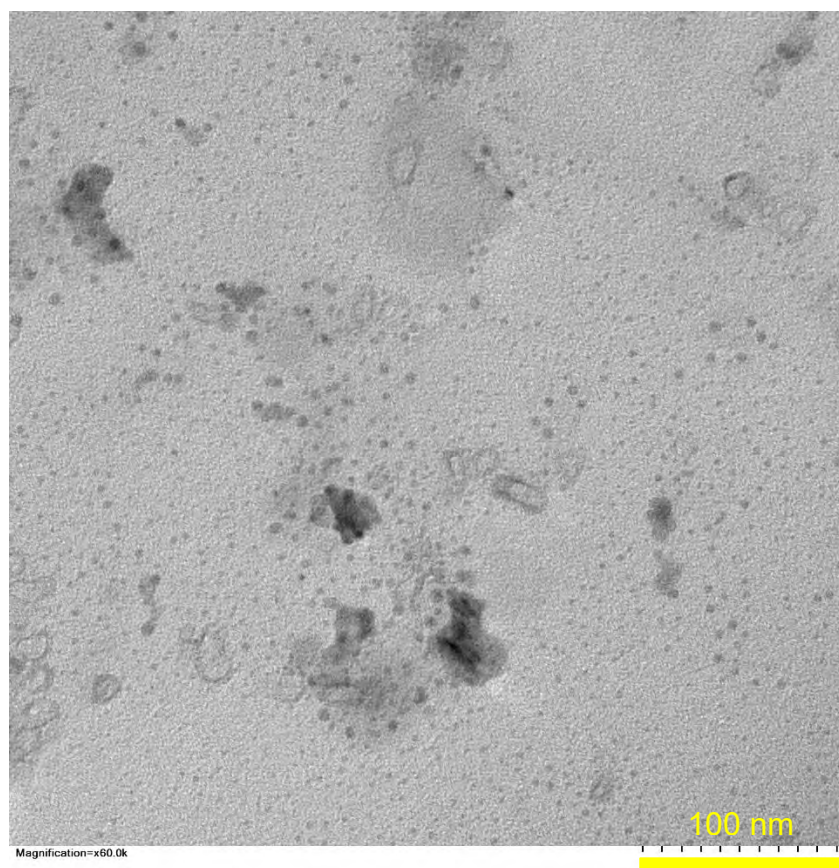
Figure 4.10. TEM images of sample E
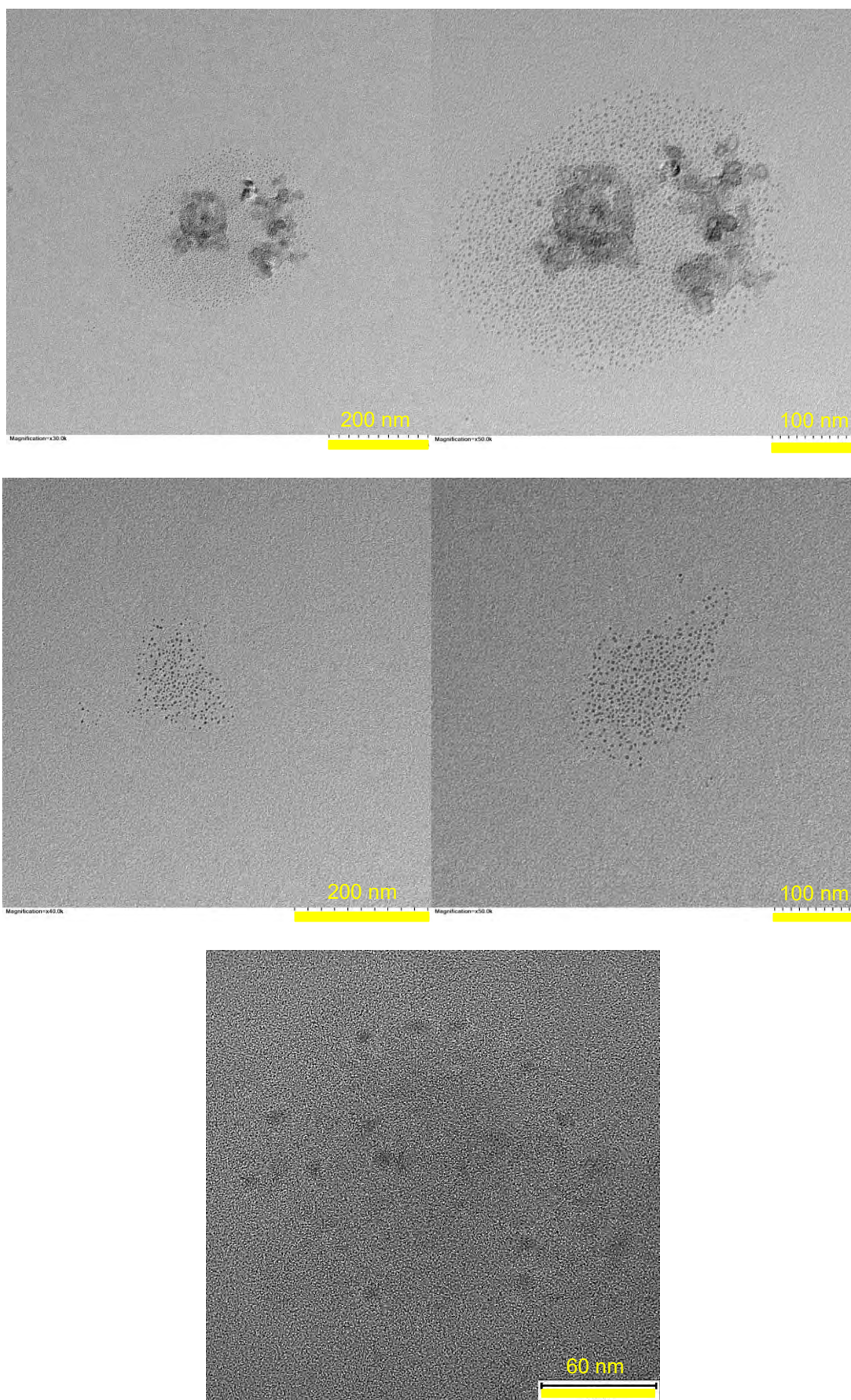
Figure 4.11. TEM images of sample F
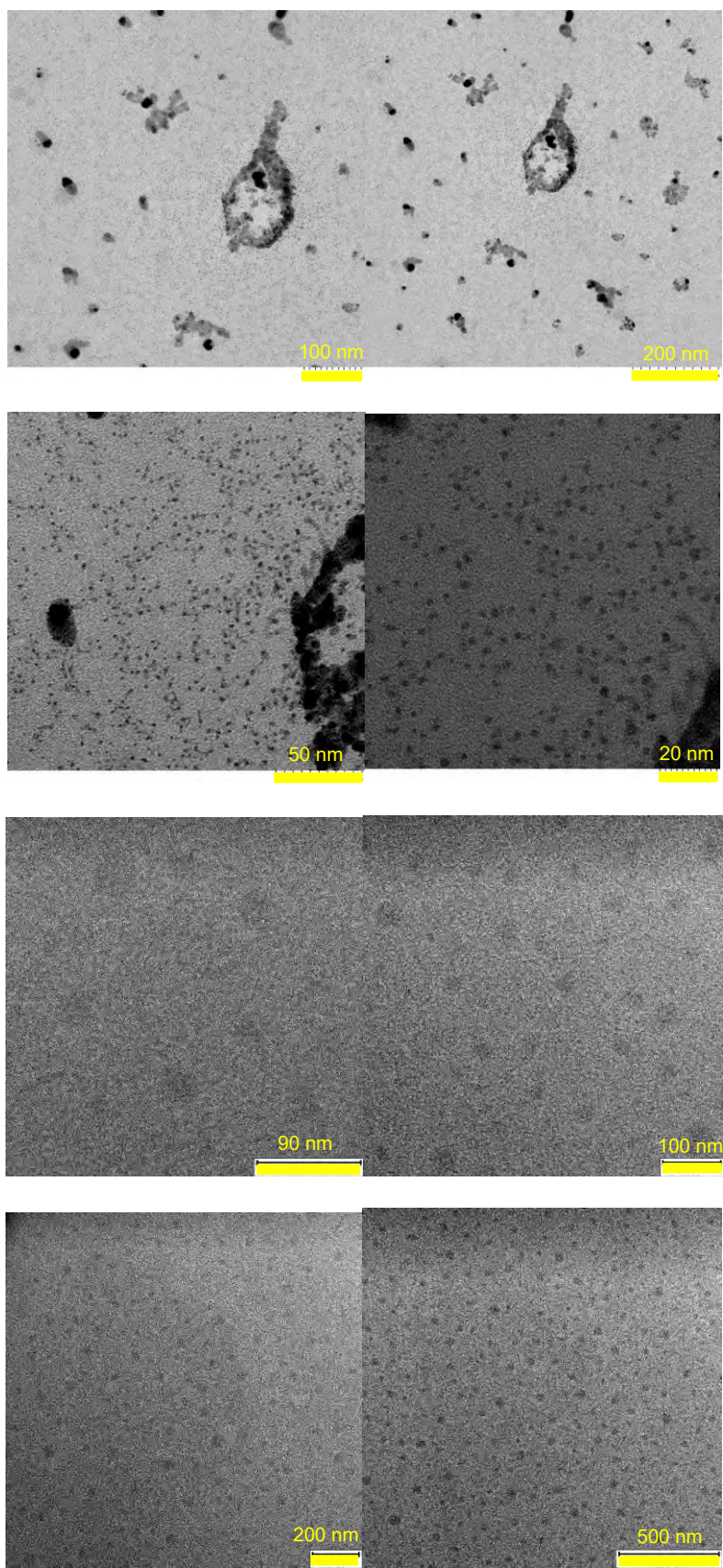
Figure 4.12. TEM images of sample G

Chapter 5 The effects of nitrogen doping on optical properties of carbon dots

In this chapter, the results of investigating the optical properties of N-CD samples were presented: Fluorescence emissions were mapped on 3D excitation-emission matrices at varied concentrations, UV-visible absorptions were recorded, and the efficiency of emissions were determined by quantum yield measurements.

5. 1. The absorption spectra of the N-CDs samples

Figure 5.1 shows the absorption spectra of the seven samples recorded with the Horiba Duetta fluorescence and absorbance spectrometer. Concentrations of each N-CDs solutions were adjusted to have the maximum of absorption positioned approximately at 0.1. Here are the notable trends extracted from the absorption spectra of the N-CD samples.

1. The featureless absorption shoulder of N-CDs at 200-240 nm that is generally attributed to $\pi^* \to \pi$ transition of the sp^2 carbon core bands is wider in samples with less nitrogen content.

2. The narrower absorption shoulder in samples with higher amount of nitrogen indicates the existence of more functional groups on their edge/surface which, impedes exposition of the core to the solvent.

3. There exists a broadband from 285 to 365 nm in the absorption spectra for all the N-CDs intensity of which enhances as the nitrogen doping increases. This band is commonly assigned to either $\pi^* \to n$ molecular or surface/edge electronic transitions of nitrogen and oxygen containing groups, however contribution from $\pi^* \to \pi$ transitions is strongly argued [2].

4. The greater extension of the absorption tail into the longer wavelengths in samples with more amount of nitrogen. This is a compelling evidence nitrogen

states should be responsible for the reddest component of the emission spectra.
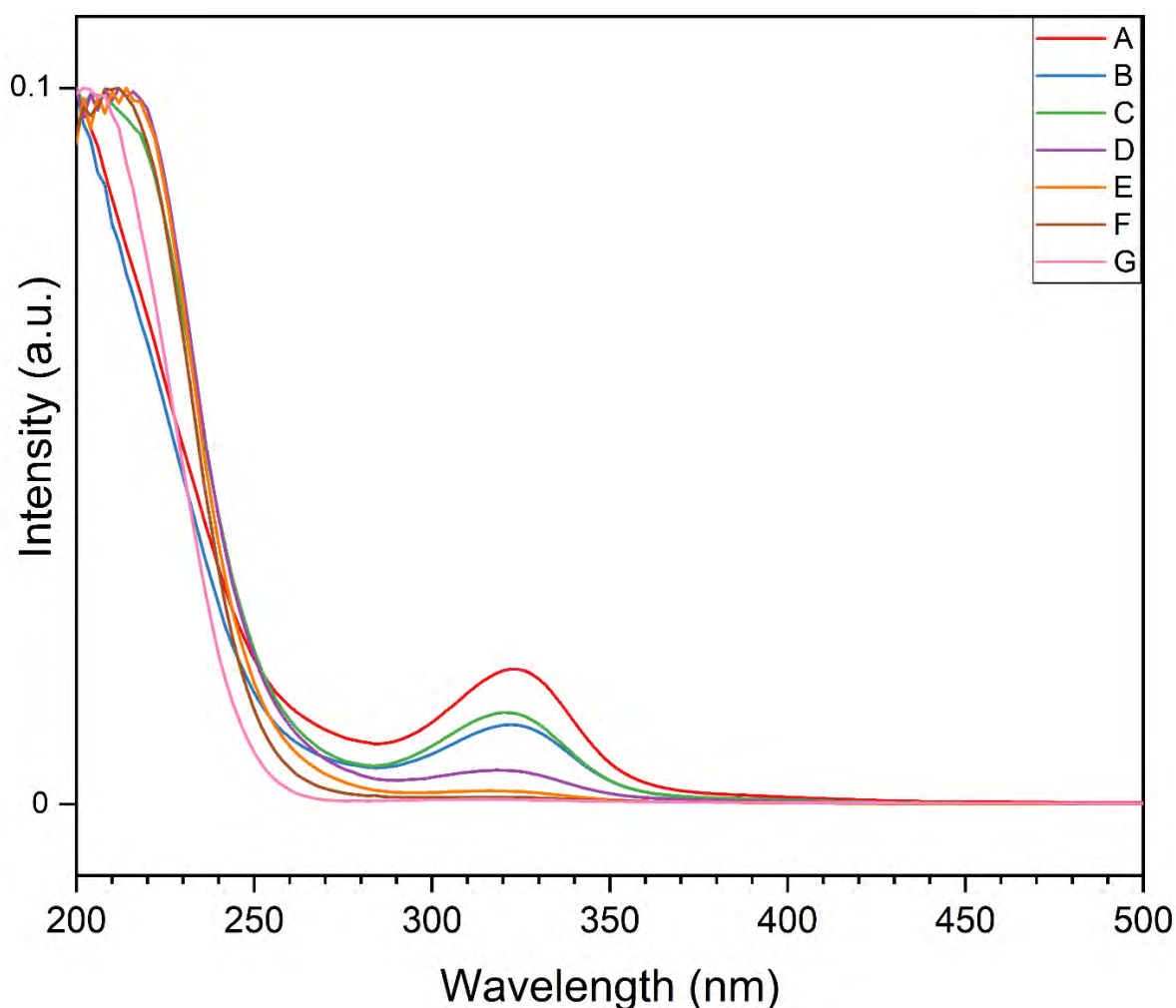
Figure 5.1. The absorption spectra of the N-CD samples.

5. 2. Fluorescence emission spectroscopy

5. 2. 1. Concentration-dependent fluorescence spectroscopy of the N-CD samples

Figure 5.2(A-G) shows the 3D excitation-emission matrices of the N-CDs diluted 0, 3, 5, 10, 20, 50, 100, 500 times. All the measurements were performed using the same instrument setting. This ensured that the amplitude and the colour of scale in these figures provides a good comparison between fluorescence emission of the samples.

Several trends are evident in Figure 5.2(A-G). Two major emission curves can be distinguished in mid-range concentrations of higher carbon/nitrogen content CDs (A100, A500, B50, B100, C50, C100, D20, D50, E10). Of these two curves, the emission of the redder one (Curve II) is broadly excitation dependent, redshifts with the increase of concentration. Along this redshift the emission intensity of the curve decreases though there is an optimum concentration for the highest emission intensity for each sample (A100, B50, C20, D10, E5, F3, G3). The wide breadth of the curve indicates that it comprises at least two emissive centres. The bluer curve (curve I) appears individually in mid-range concentrations (A100, A500, B50, B100, C50, C100, D20, D50, E10), disappears at high concentrations (A50, B20, C20, D10, E5 and higher) and integrate into the curve II at lower concentrations. The broadness of the curve in B500, C500, D100, E20 indicates the arrival of the two curves at each other. Curve I show excitation independent emission that is one significant characteristic of molecular type of fluorescence. The emission peak from this curve is located at 440 nm with a very narrow excitation range of 285-305 nm. Contrary to curve II, the bluer curve does not shift in wavelength with the change of concentration when individually present. As an example, the two curves and three fluorescence centres are shown on the 3D excitation-emission map for sample B50 in Figure 5.3.

A0
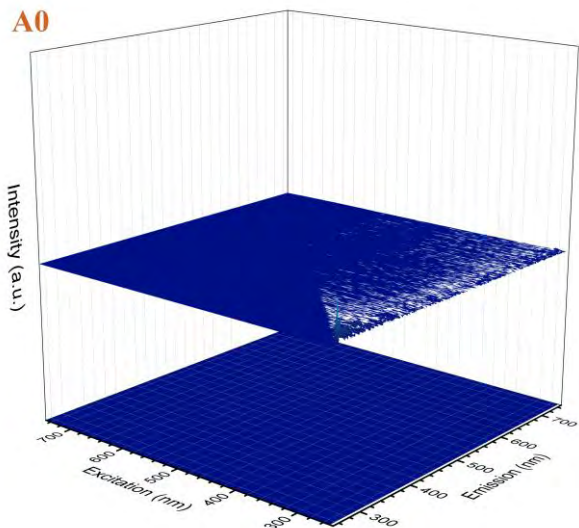
A3
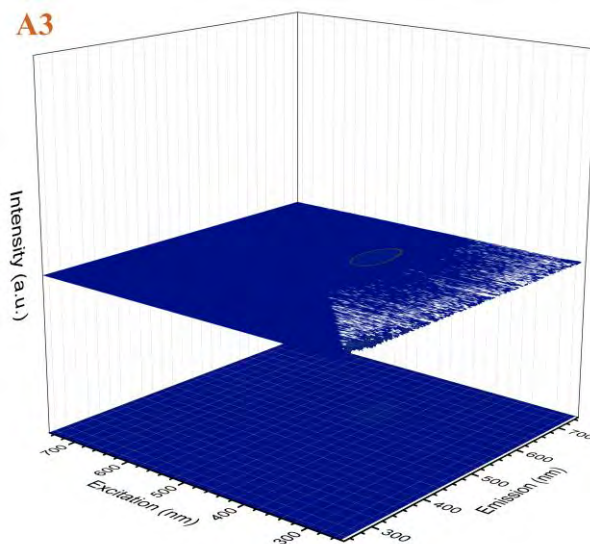
A5
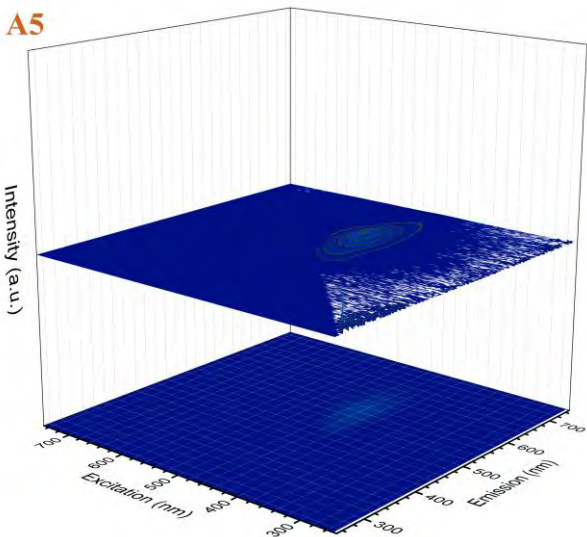
A10
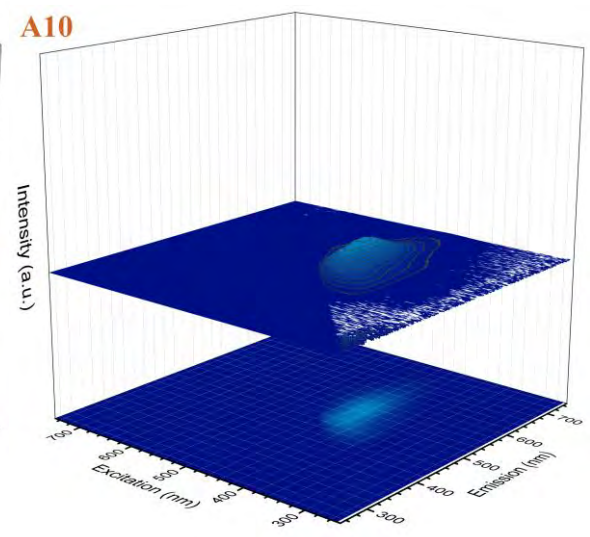
A20
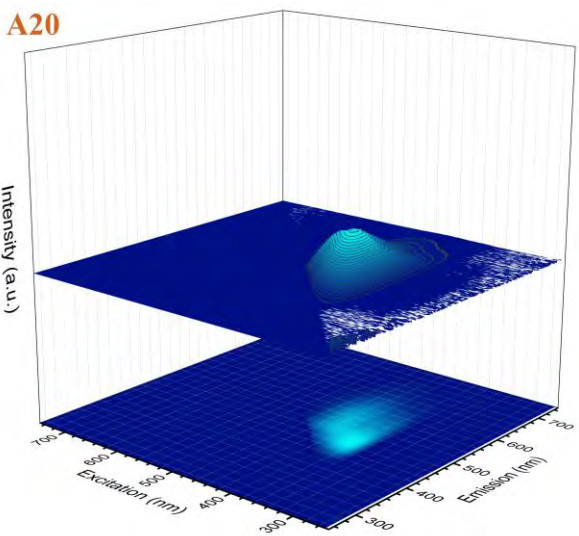
A50
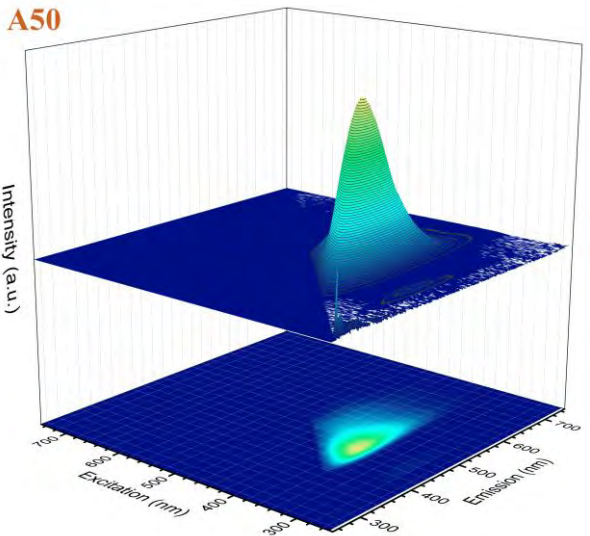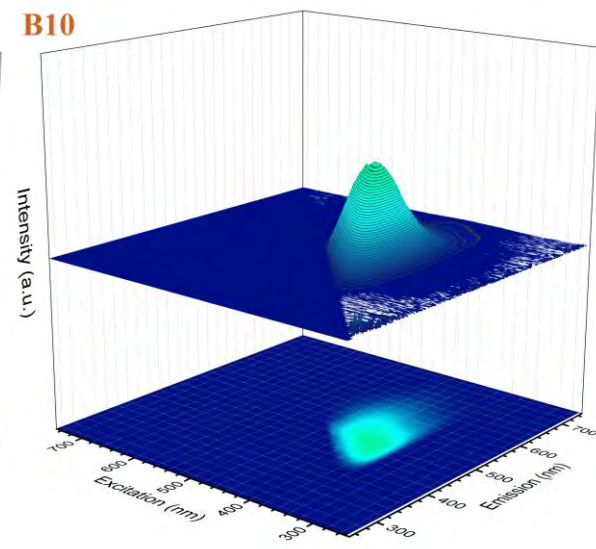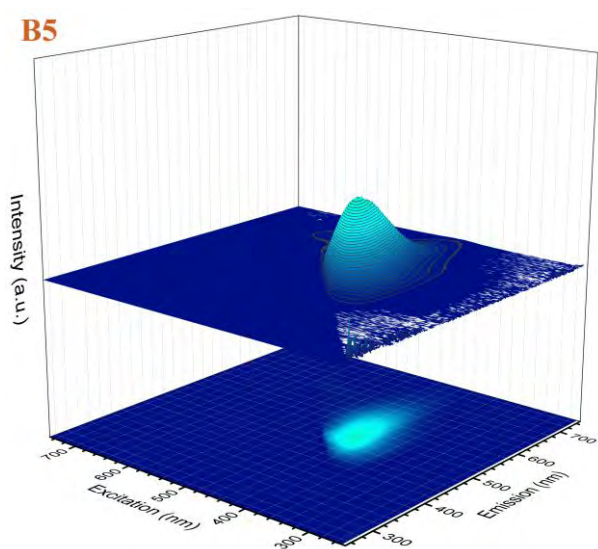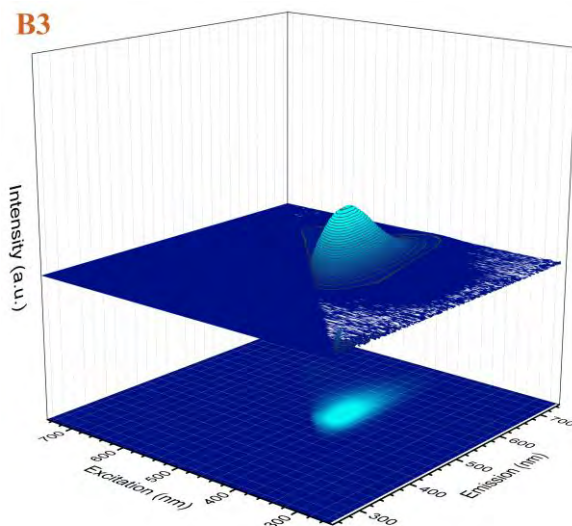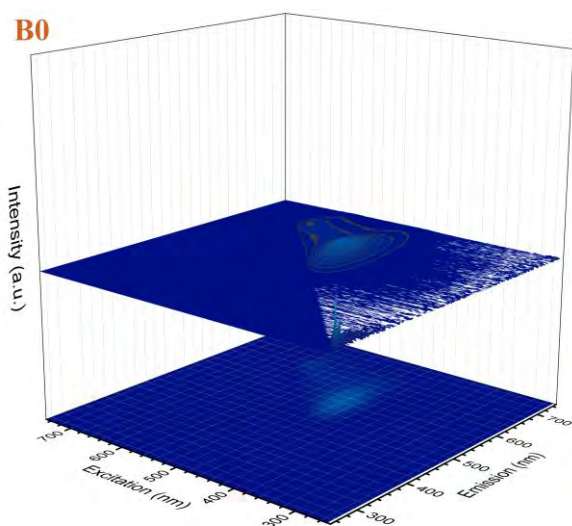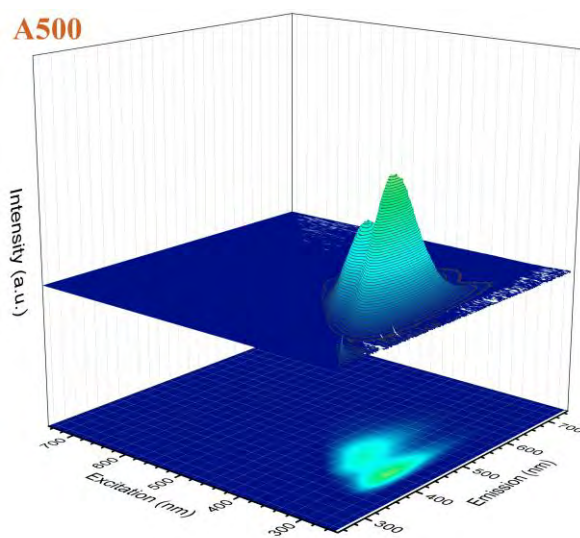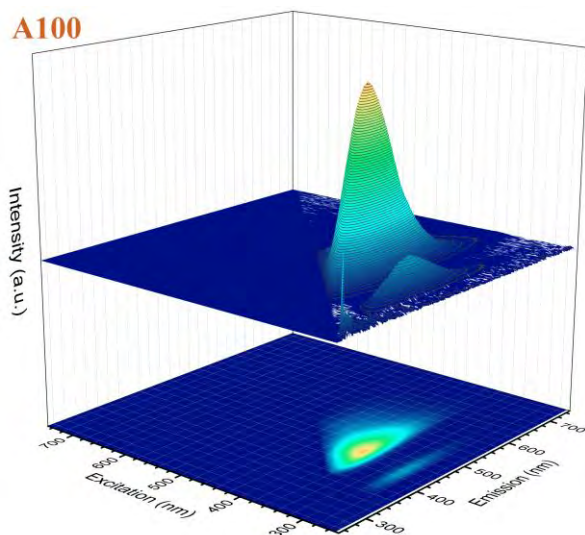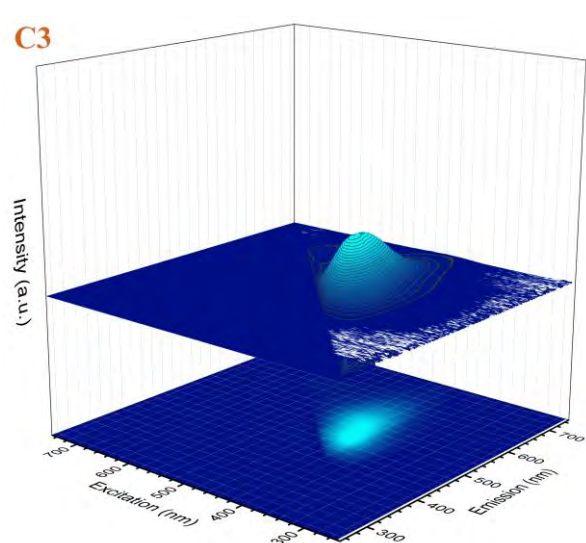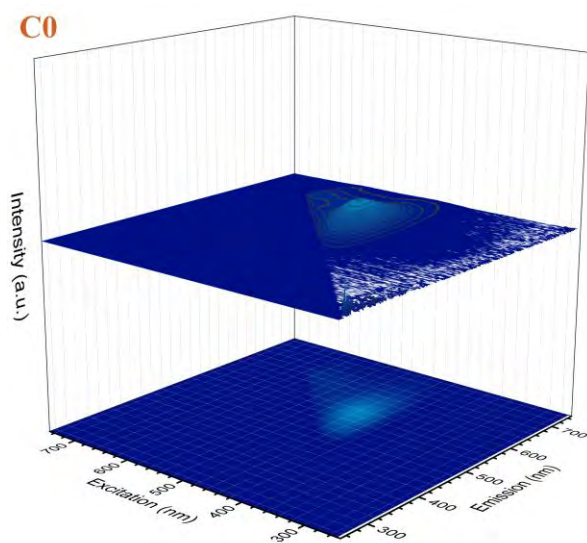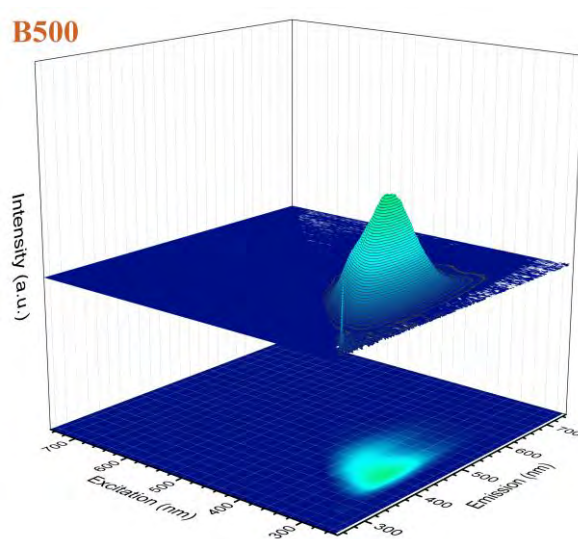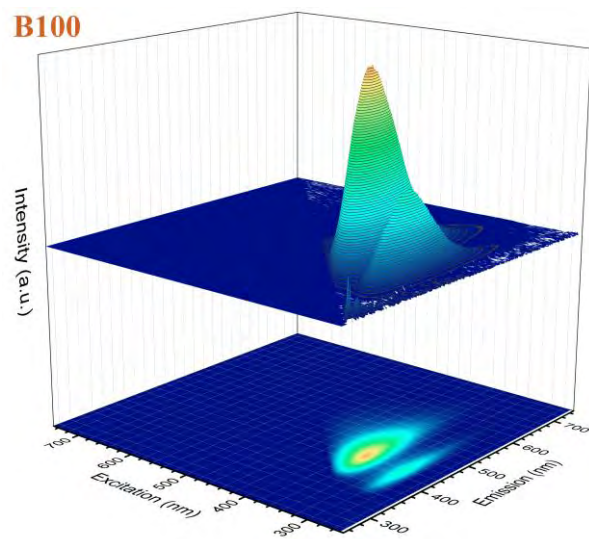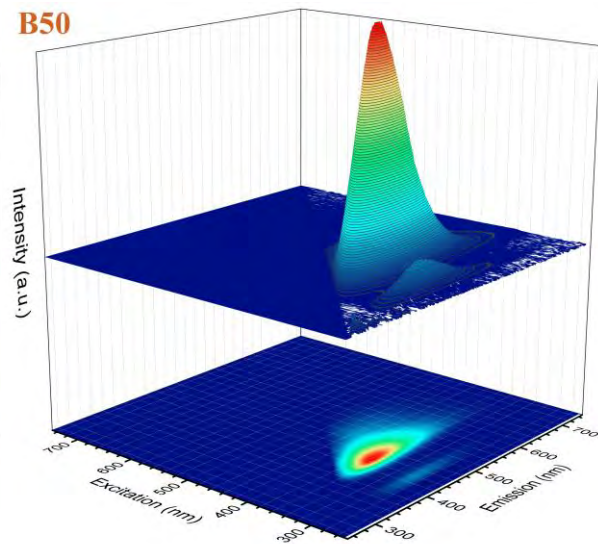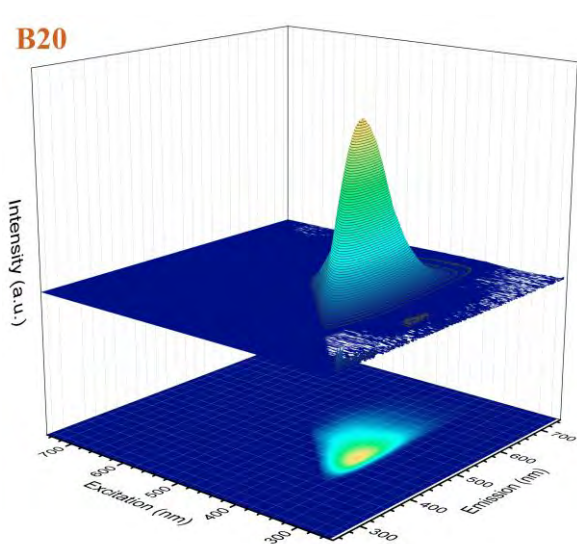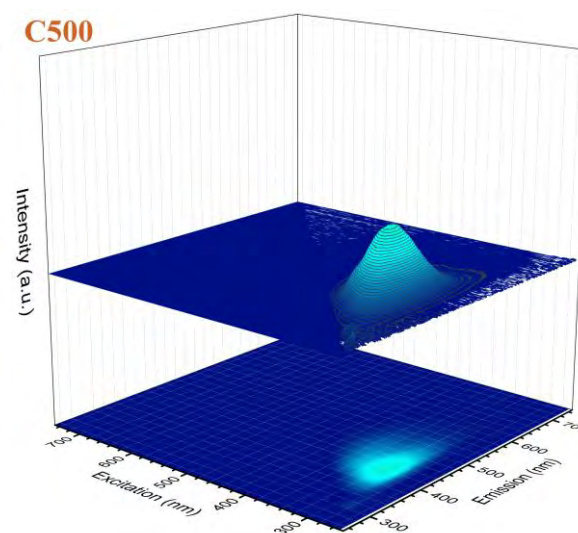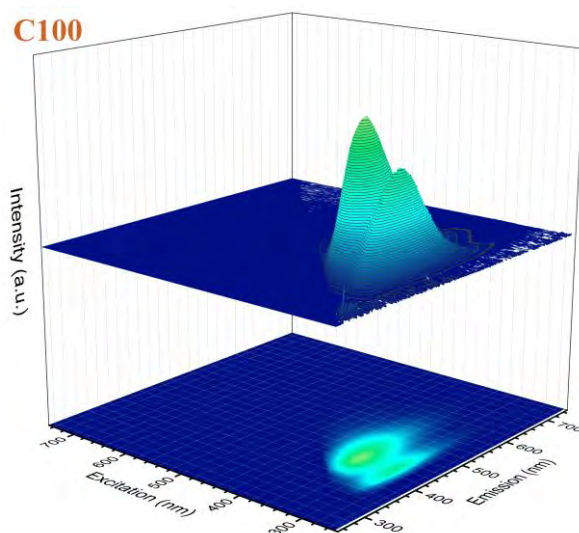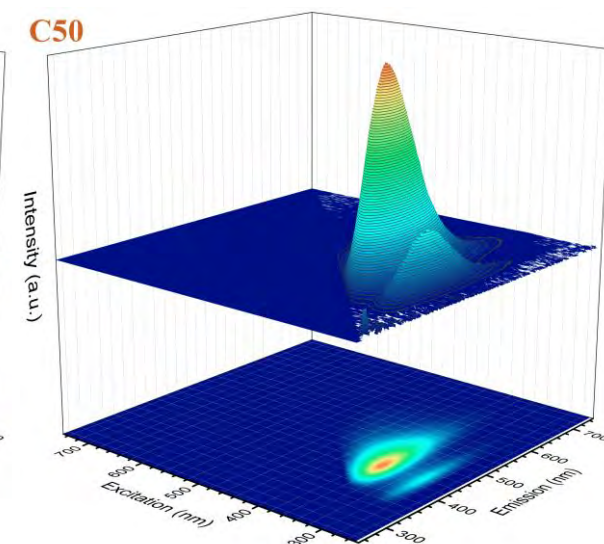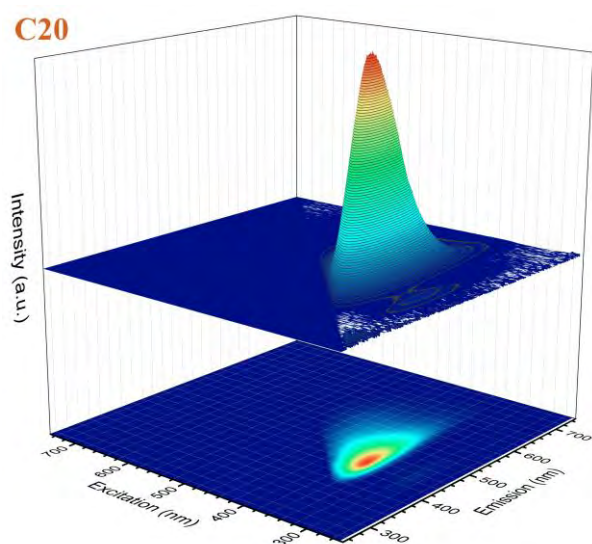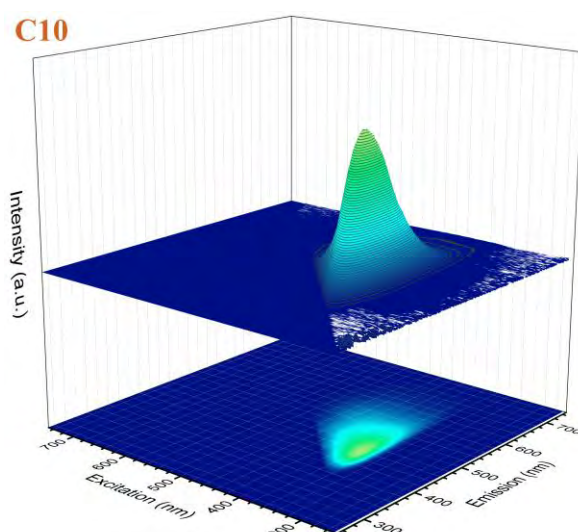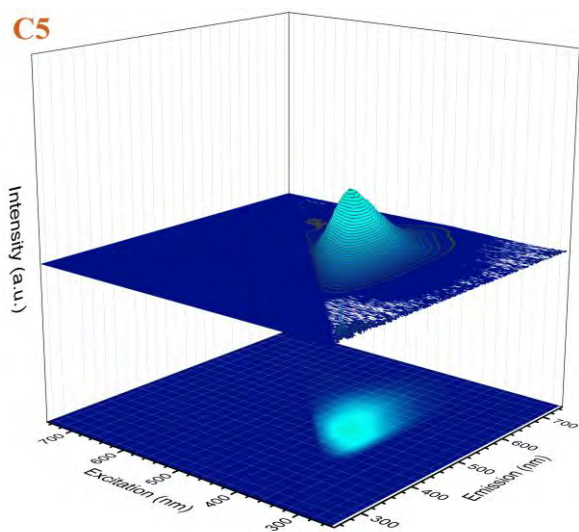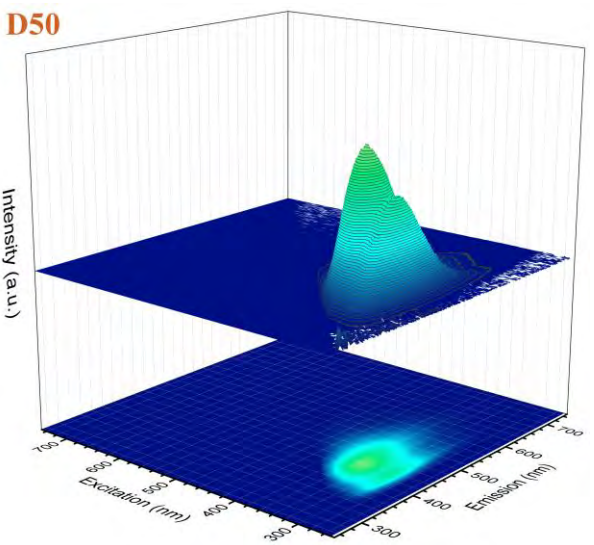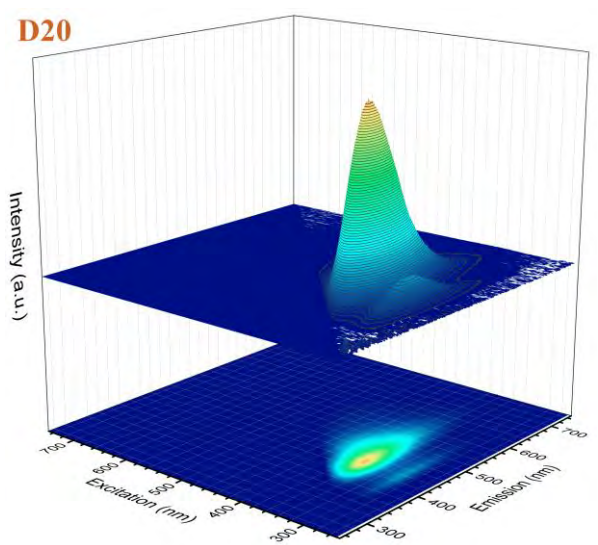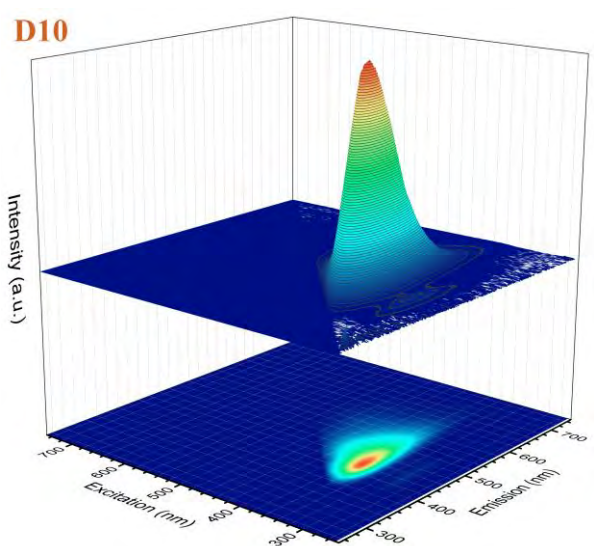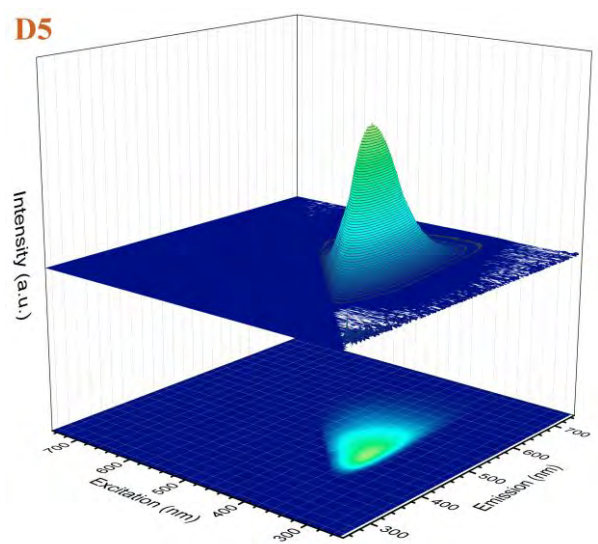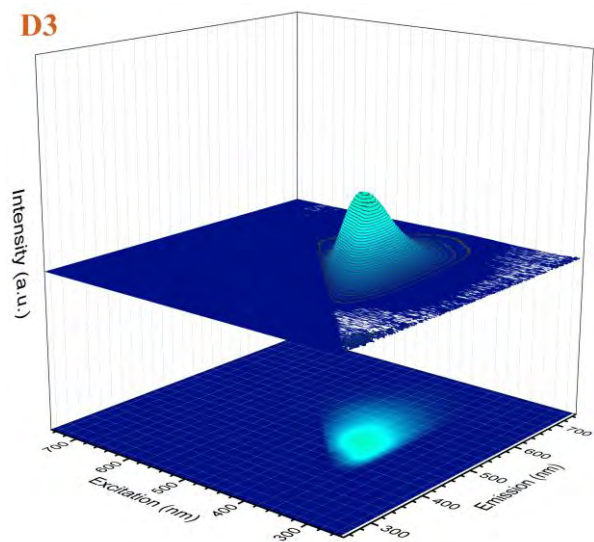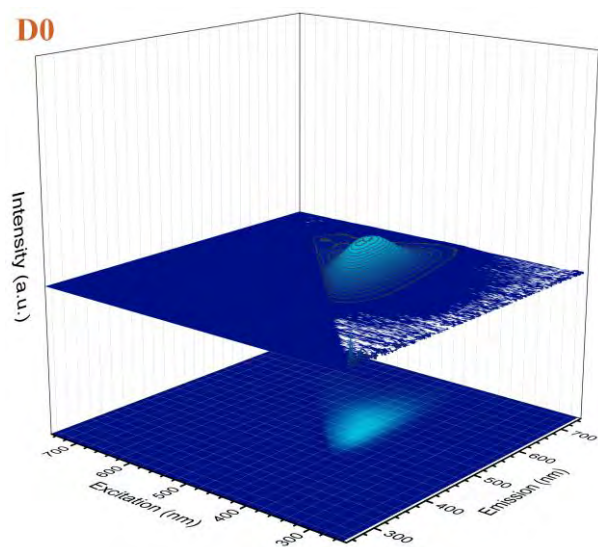
D100

D500

E0

E3

E5

E10

F5

F10

F20

F50

F100

F500

G0

G3

G5

G10

G20

G50

110
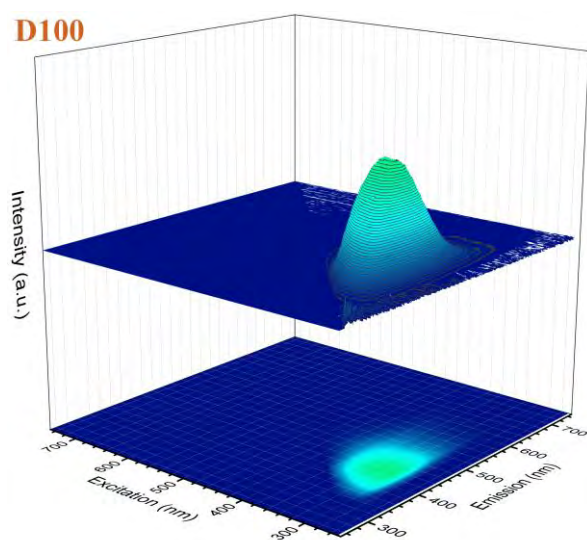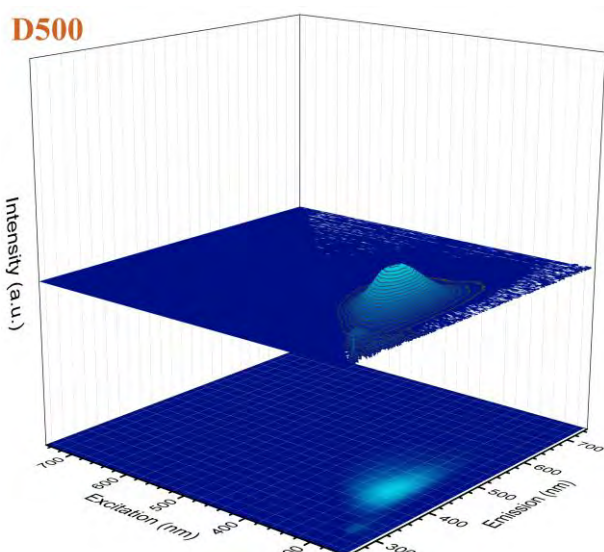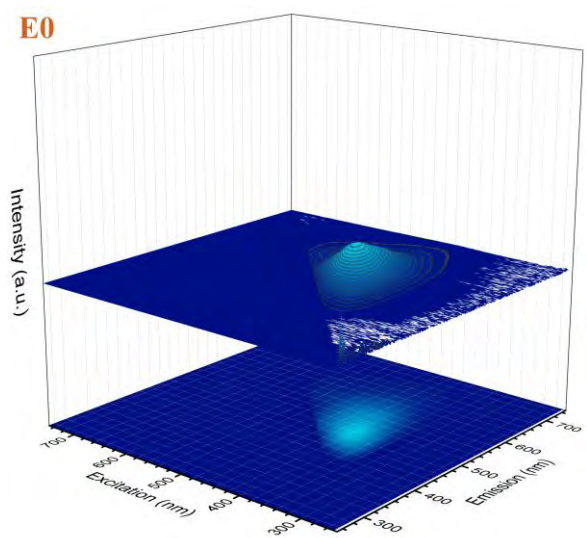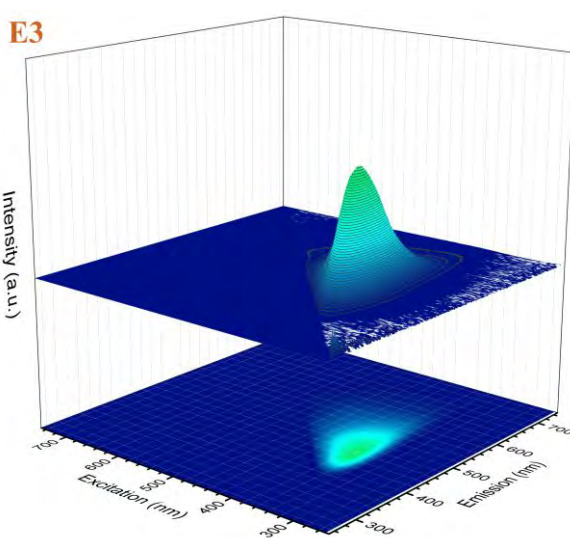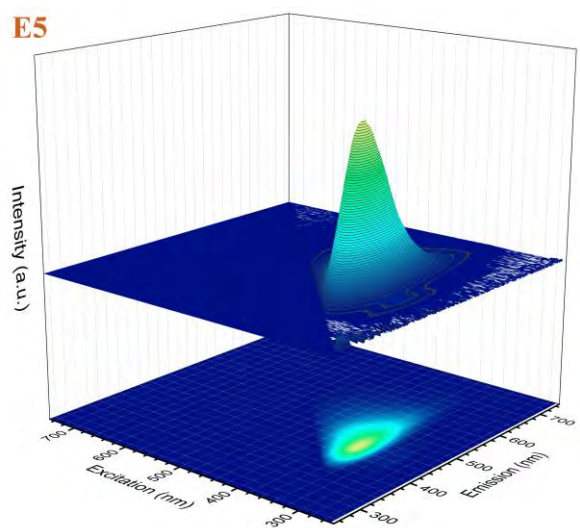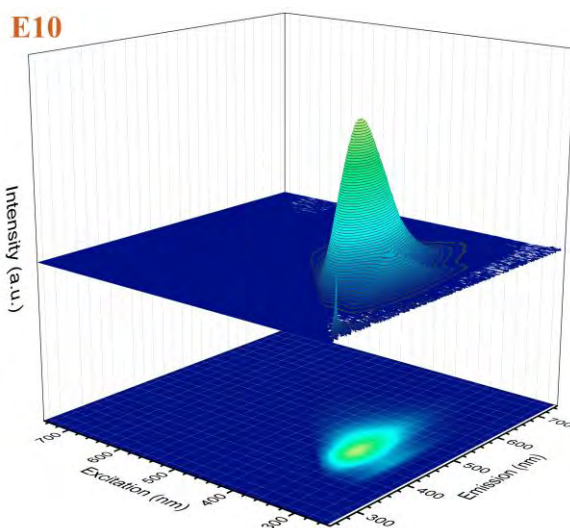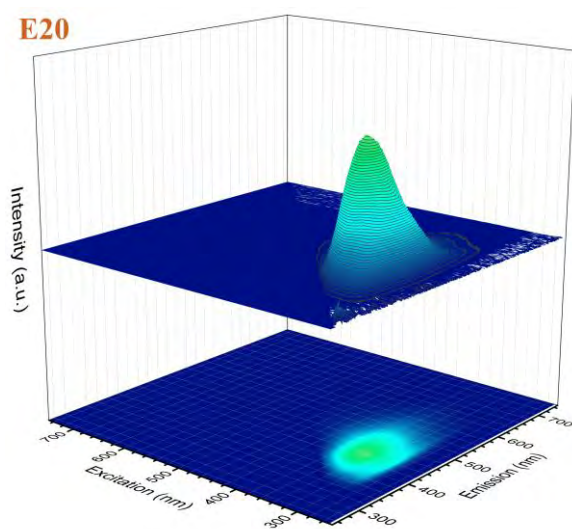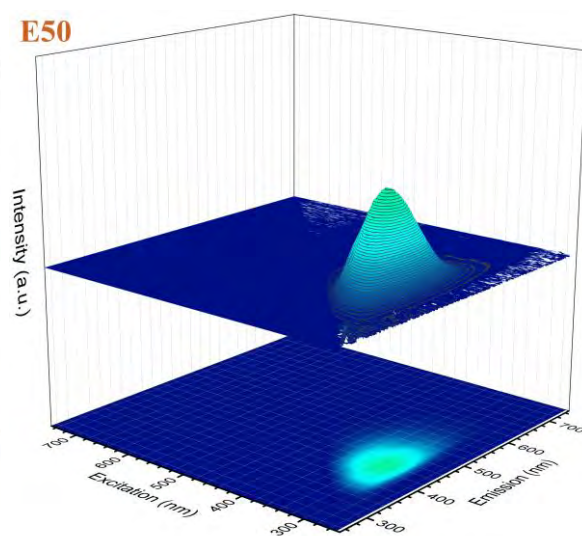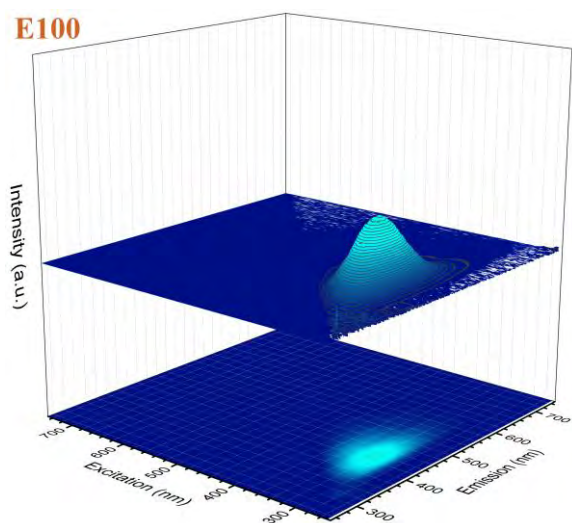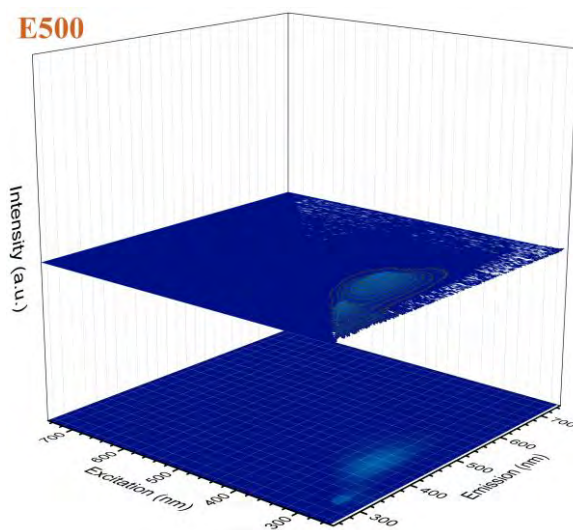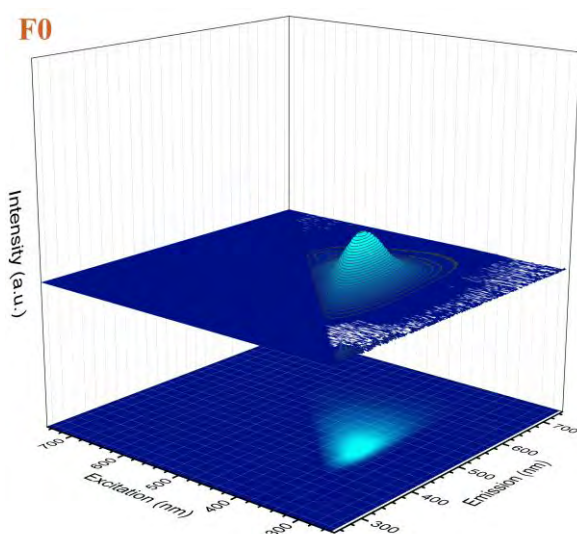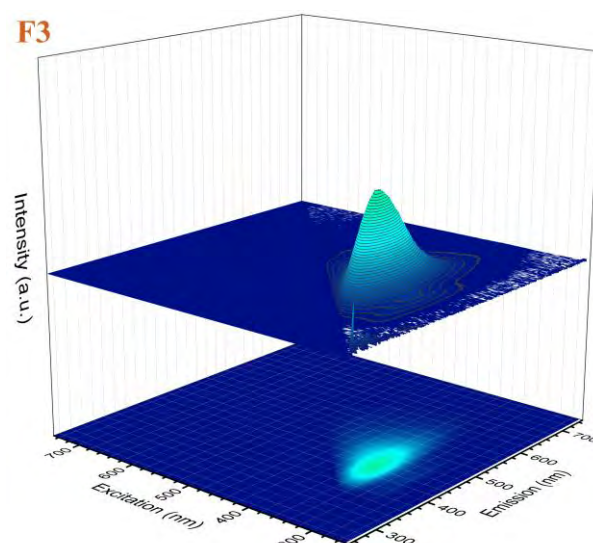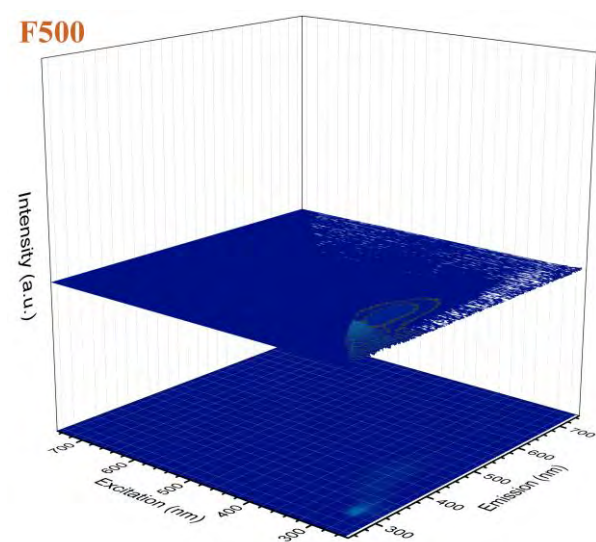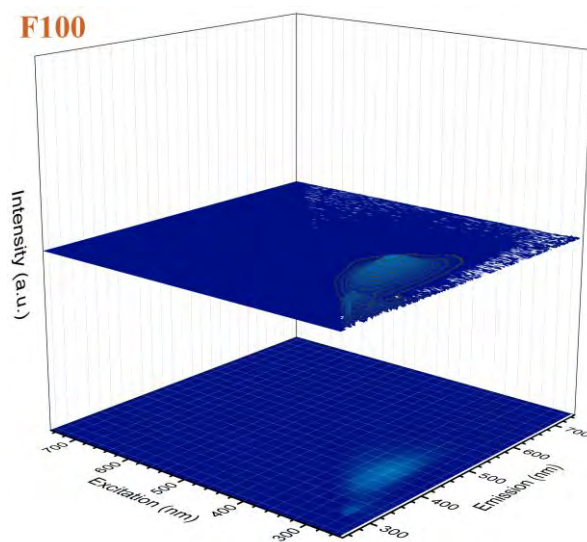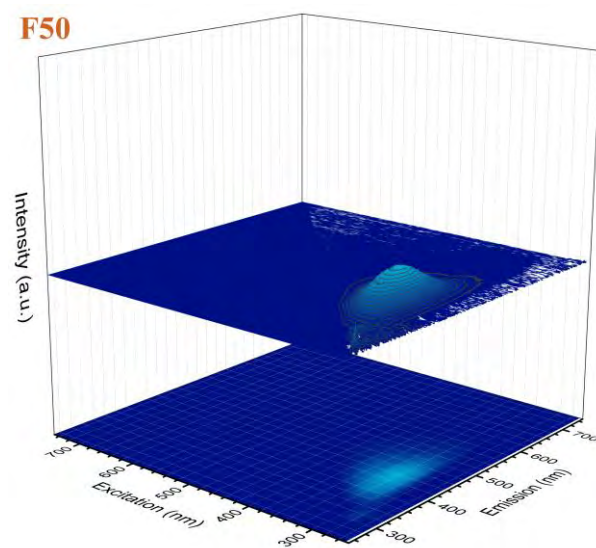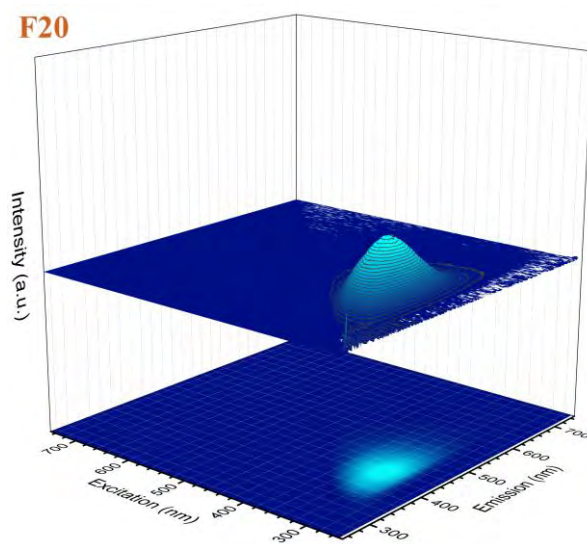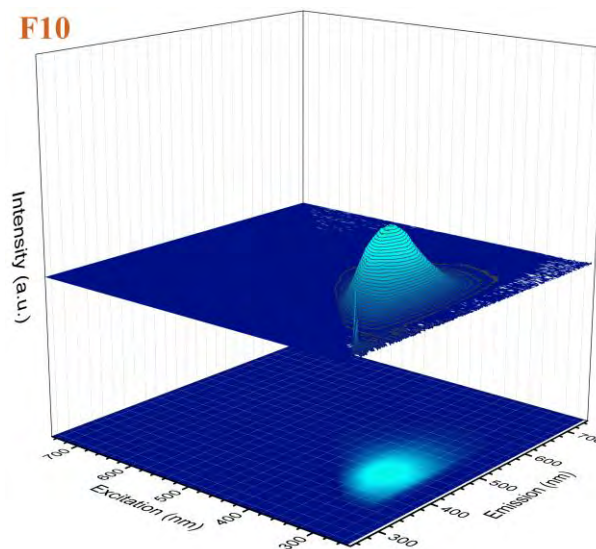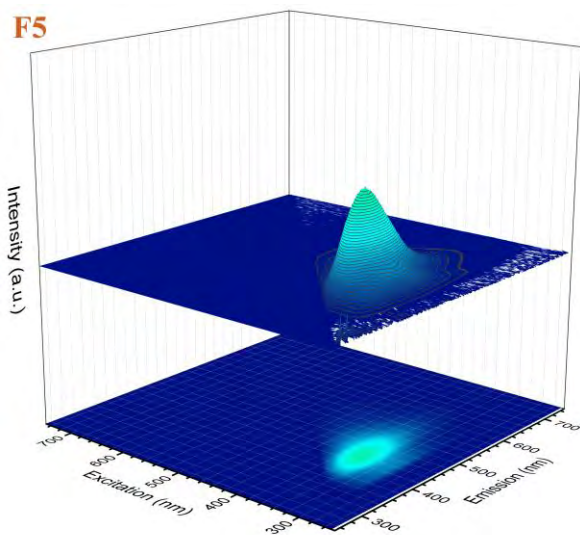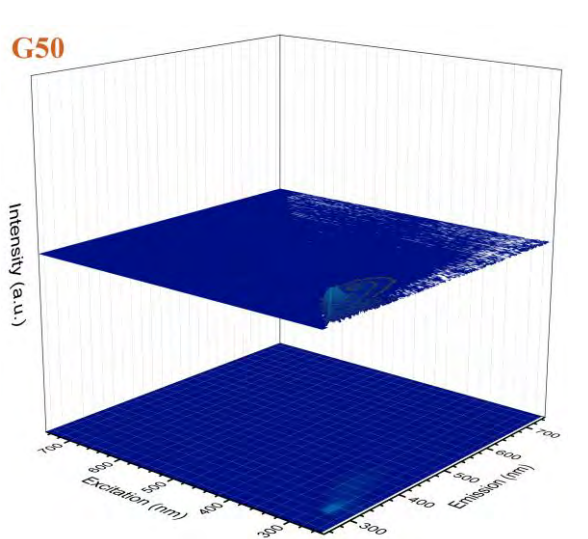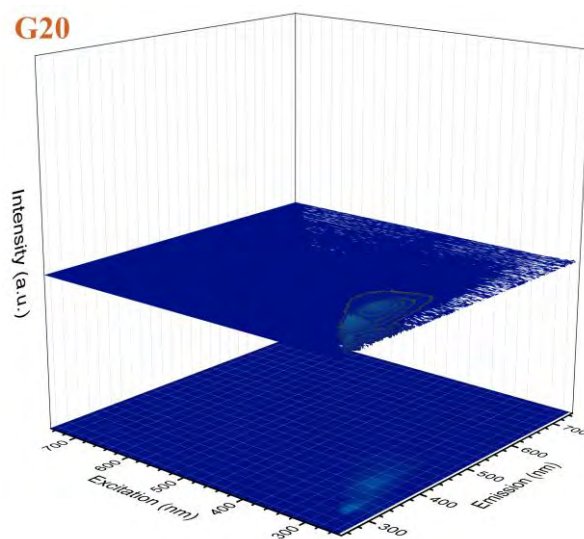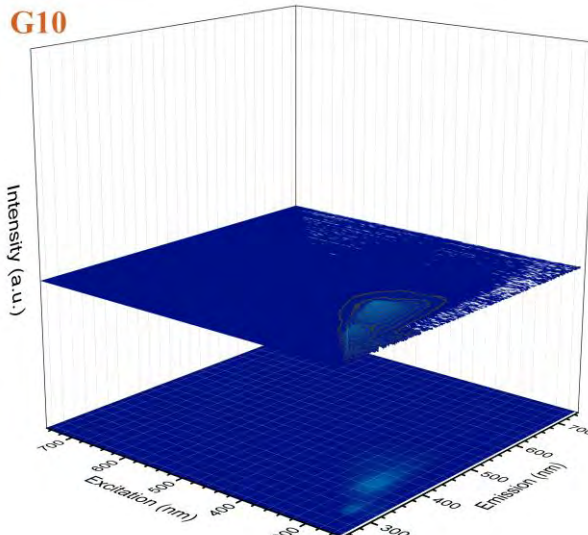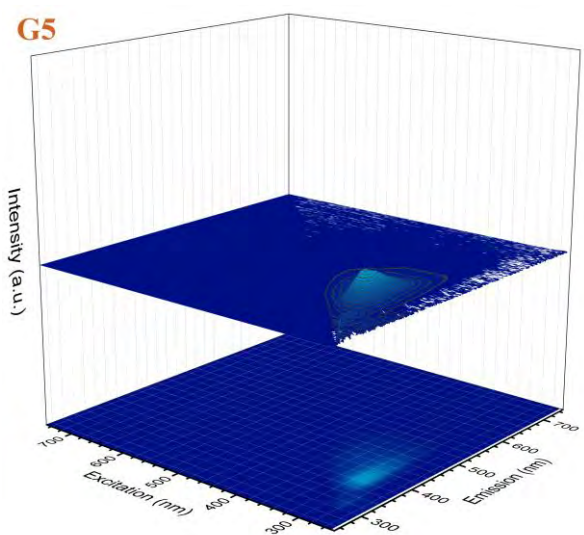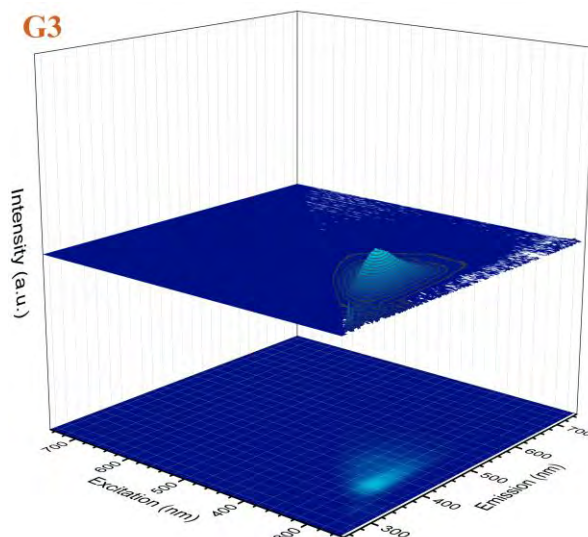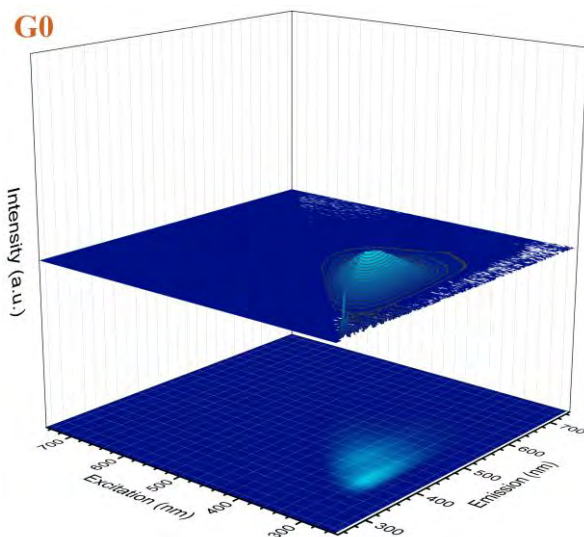
Figure 5.2. 3D maps of excitation-emission matrices of (A-G) N-CDs samples diluted 0, 3, 5, 10, 20, 50, 100, 500 times.
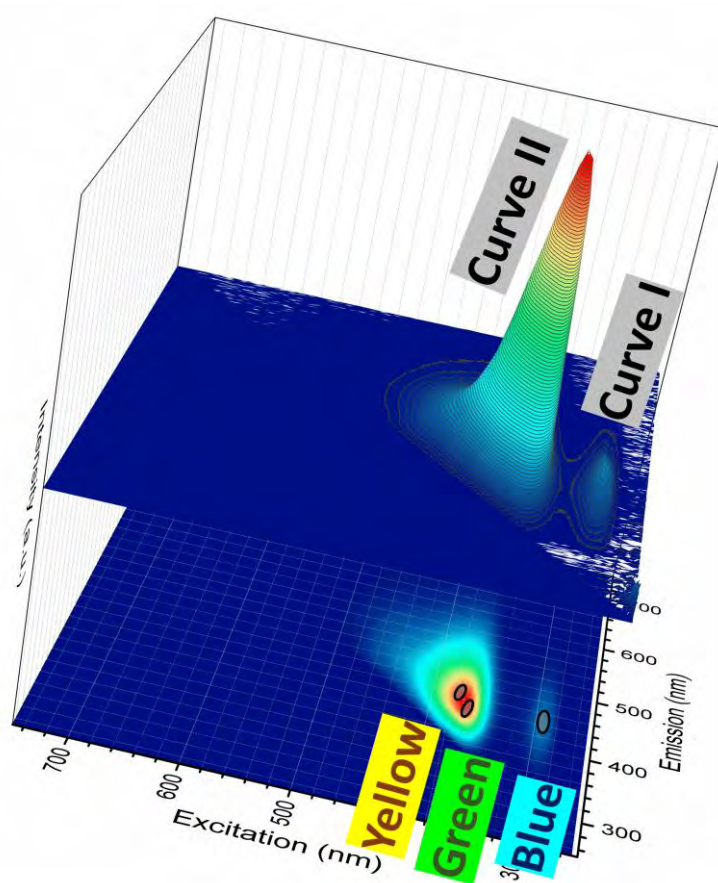
Figure 5.3. The two curves and three emissive centres on the excitation-emission matrix for sample B50.

To further illustrate the fluorescence characteristics of the samples, their emission at concentrations of A100, B50, C50, D20, E10, F5, G3 for excitation wavelengths of 300, 320, 340, 360, 380 nm are shown in a 2D plot in Figure 5.4. The excitation spectra of the seven samples at concentrations of A100, B50, C50, D20, E10, F5, G3 fo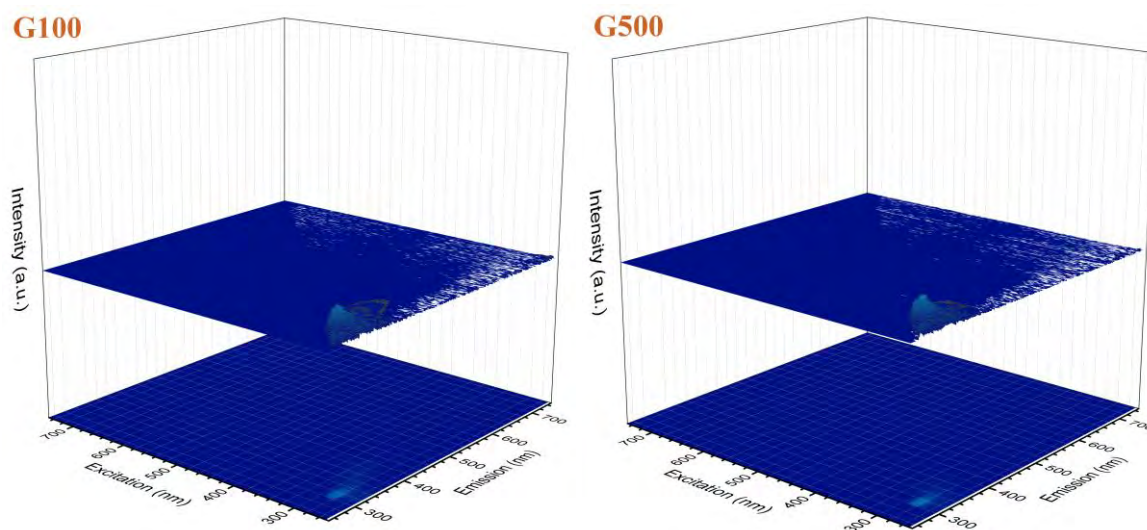r emission wavelengths of 440, 460, 480, 500, 520 nm are also depicted on a 2D plot in Figure 5.5. As can be seen, there are two major excitable bands around 300 nm and 360 nm for the two curves. The trend here is that in samples of more nitrogen content, the two bands are discrete whereas with the decrease of nitrogen the 360 nm band blue shifts towards the 300 nm one.

Figure 5.4. The emission spectra of the N-CDs samples for excitation wavelengths of 300, 320, 340, 360, 380 nm at concentrations of A100, B50, C50, D20, E10, F5, G3.
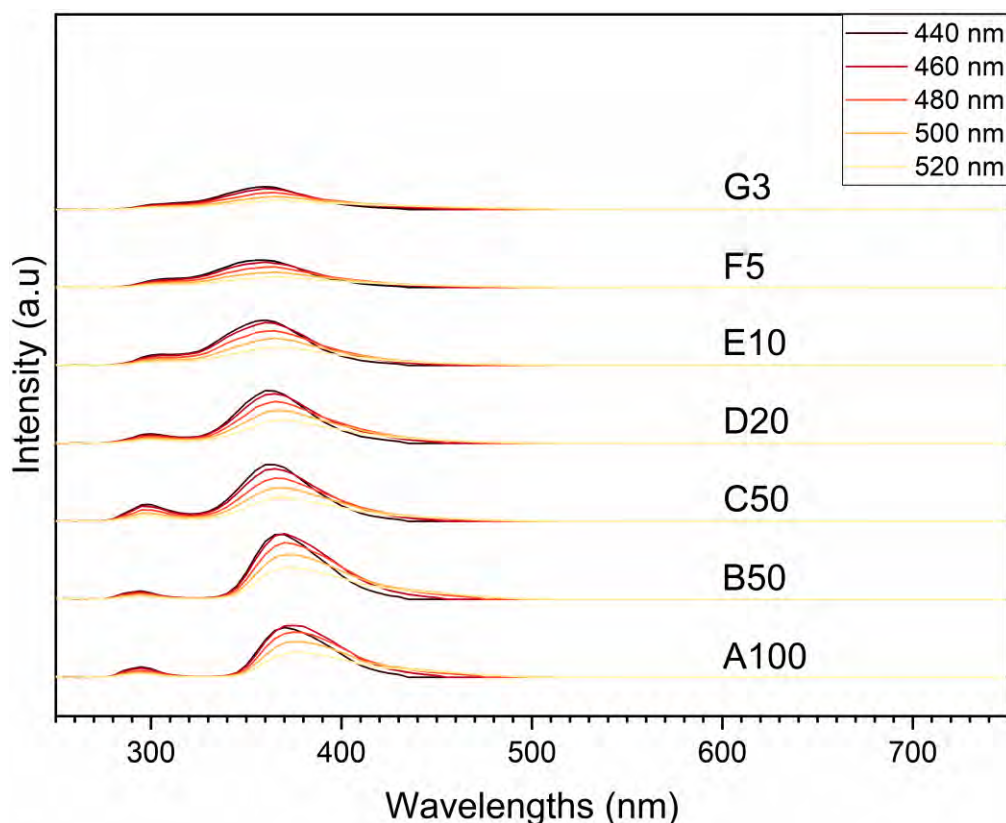
Figure 5.5. The excitation spectra of the N-CDs samples for emission wavelengths of 440, 460, 480, 500, 520 nm at concentrations of A100, B50, C50, D20, E10, F5, G3.

5. 2. 2. Photoluminescence mechanism in the N-CDs

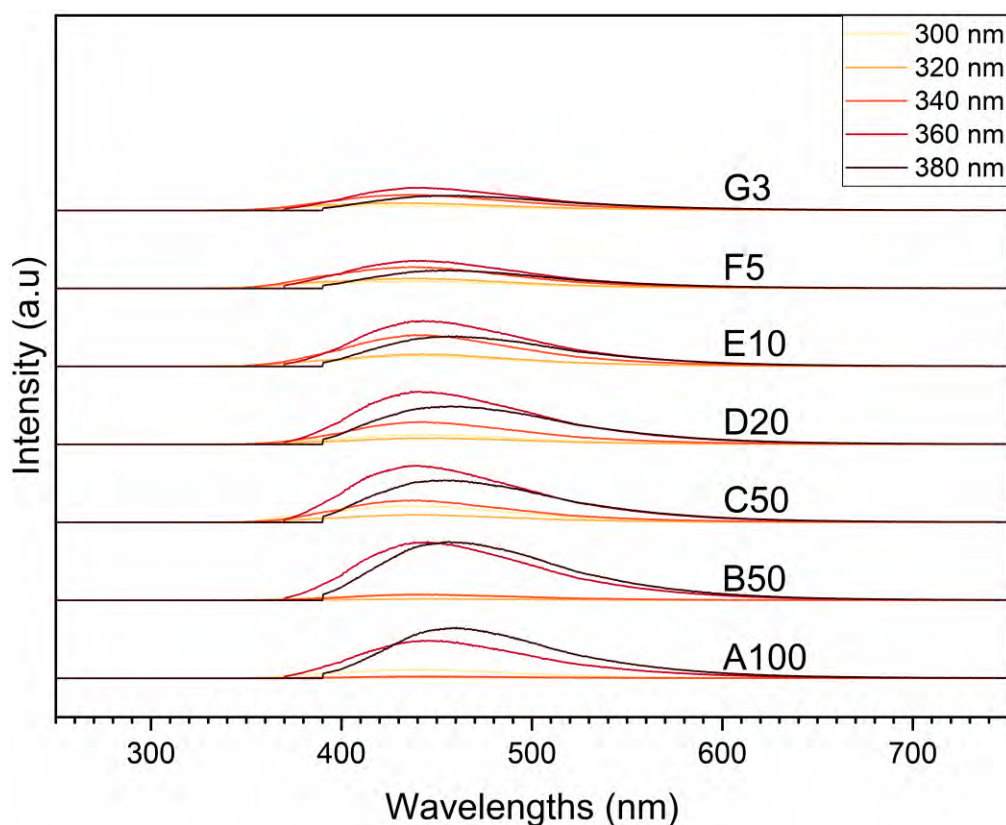Considering all the figures of excitation-emission matrices of our work into account, three major emissive centres with blue, green, and yellow wavelengths can be identified within the curves. Figure 5.6 illustrates the intensity of the three fluorescence centres for samples A-G at 0, 3, 5, 10, 20, 50, 100, 500 times dilutions. The omnipresence of the green centre in all sample solutions with varied degrees of nitrogen doping implies that the emission from this centre belongs to $\pi^* \rightarrow \pi$ transitions of the sp^2 carbon core. From the absorption results, the nitrogen states are responsible for the reddest component of the emission herein the yellow emissive centre. The very narrow excitation range of the blue centre when not merged with the green one under the bluer curve suggests that this emission may originate from molecular type of fluorescence ($\pi^* \rightarrow n$, $\sigma^* \rightarrow n$).

113

Figure 5.6. Peak intensities of the blue, green, yellow fluorescence centres of (A-G) N-CDs at dilutions of 0, 3, 5, 10, 20, 50, 100, 500 times.

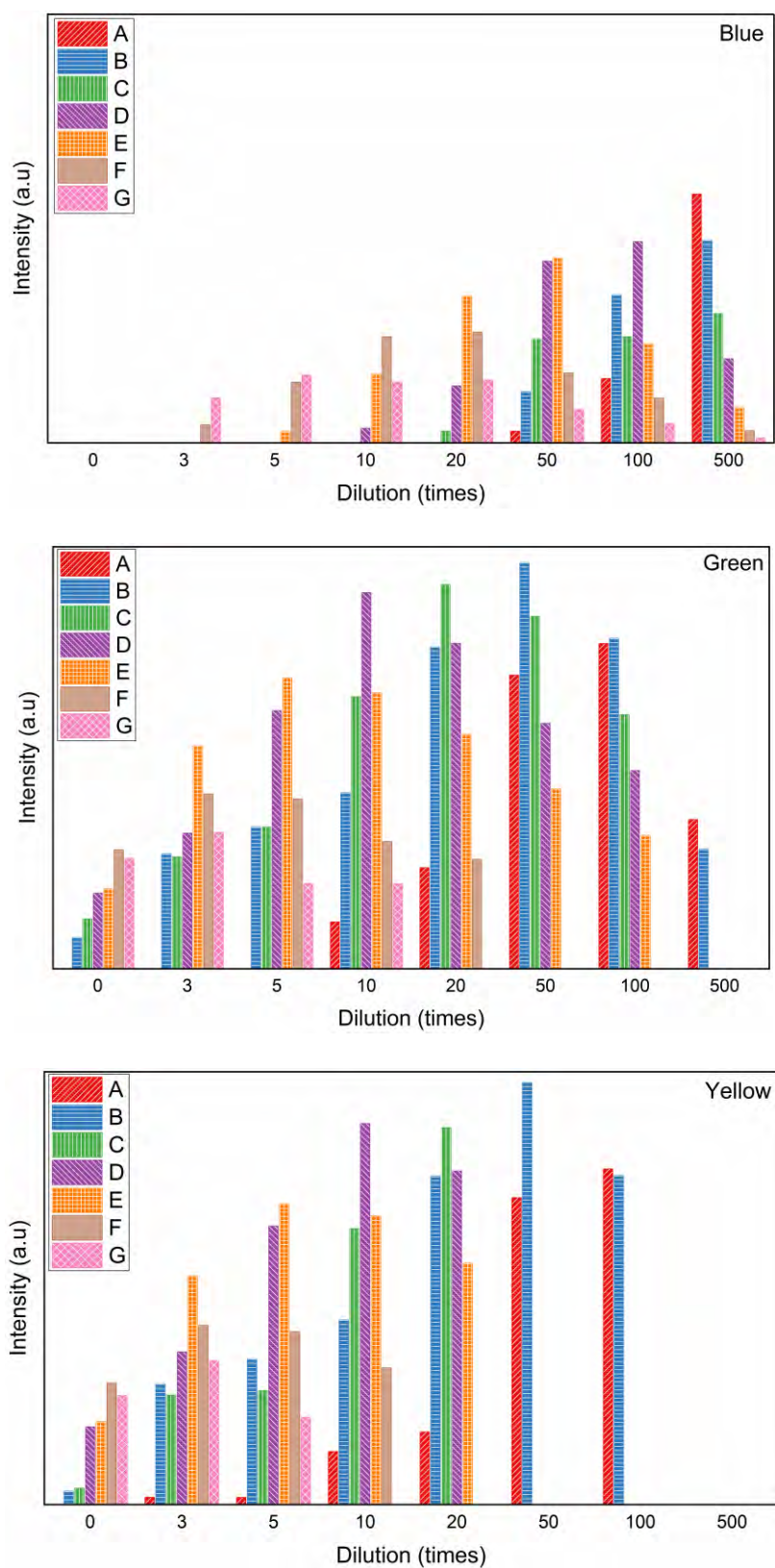Take sample C as an example to explore the mechanisms behind concentration dependent emission of N-CDs. At high concentrations (C0, C3, C5, C10), the green and yellow emissive centres shape curve II. The general trend with increasing the concentration is that the entire curve II slides to the redder region, and the emission intensity decreases. It is only in mid-range concentrations (C50, C100) that the two curves appear on the matrix simultaneously (curve I the bluer one and curve II the redder one). In this scenario, the blue centre forms curve I on its own, and the two other centres shape curve II. At low concentrations, the yellow centre disappears, and the green and blue centres merge to form curve I. The dominance of the green centre at low concentrations is a hindrance to observe the excitation independency of the blue centre as with decreasing the concentration the green centre blue shifts from curve II to integrate into curve I. In low concentrations, the combined effect of the blue and green centres under the curve I as a whole, where the prevailing green centre is widely excitation dependent, obscures our vision of the excitation independent feature of the blue centre.

Evidently, concentration dependent multi-colour emission of N-CDs originates from the competition between the three fluorescence centres. The question here is what mechanisms determine the winner of this competition. Energy transfer between the emitting centres through non-radiative cross relaxation and the existence of self-absorption/inner filter effect can aptly describe the system. At high concentrations, there would be many and various energy states on which both radiative recombination and non-radiative cross relaxations are probable to occur. It can be postulated that with the increase of concentration, more non-radiative cross relaxation pathways are provided for electrons to finally recombine at lower energy states. At the same time, self-absorption and/or inner filter effect is in place quenching the bluer region. The

provision of such an abundant variety of states results from the aggregation of CDs clusters of different sizes. That the presence of these states facilitates energy transfer between the adjacent fluorescence centres ultimately dictates the emission characteristics. In mid-range concentrations, the moderated self-absorption/inner filter effect would allow the blue centre to appear on the excitation-emission matrices where the other two centres have still a role to play. At low concentrations, cross relaxations to lower energy nitrogen states are hindered as the addition of adequate water assists the inductive effect, which enhances charge carrier density in the core leading to the disappearance of the yellow centre while the blue and green centres are present. Of our other observations here is that with the increase of concentration, the green and yellow centres redshift along the matrices while decreasing in amplitude. Population of oxygen states which provide the pathway for cross relaxation to lower energies can again explain this observation. Oxygen related groups are known to be non-emissive electron traps [156], and their existence on the surface of our N-CDs has been confirmed in the FTIR spectrum.

It has been demonstrated that functional groups in photoluminescence of graphene quantum dots contribute to both blue and red edges of the emission. Interestingly, it is the bluest component that shows the molecular type of fluorescence characteristics [157]; it is spectrally invariable with the change of particle size or excitation energy. The concentration dependent photoluminescence study of N-CDs here also confirms that the emission of the blue centre does not change with the excitation provided that the preponderant green centre would allow it to individually exist. Furthermore, there are corroborative evidence explaining N-CDs synthesized from citric acid precursor consist of fluorescence derivatives that contribute to the blue emission [1].
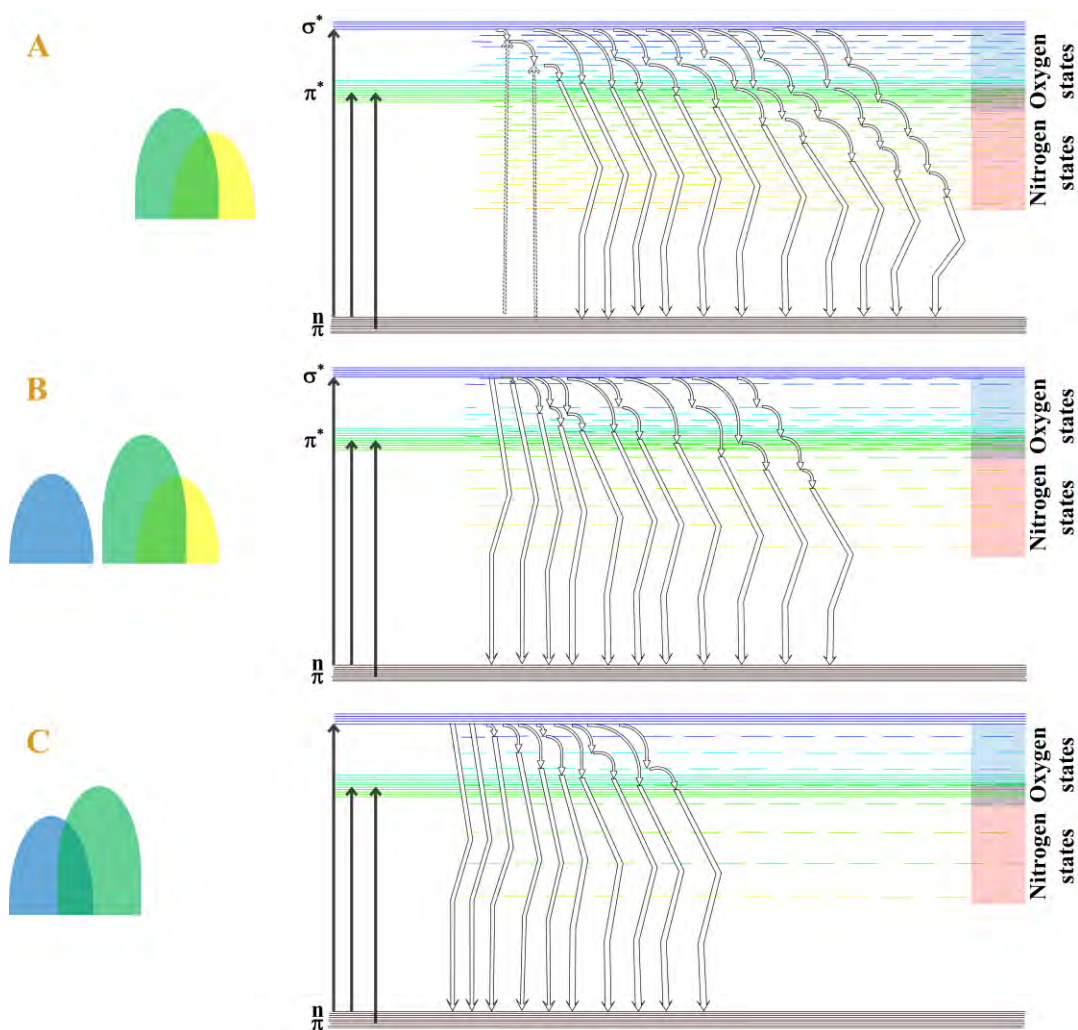
Figure 5.7. Illustration of the proposed fluorescence mechanism of N-CDs at high (A), medium (B), and low (C) concentrations.

Taking our results into account and considering the established arguments around the fluorescence origin of CDs, the reasoning behind both core-state model and molecular fluorescence are credible and convincing. Thus, it can be proposed that the two mechanisms co-exist in the system complicating our understanding of CDs photoluminescence. Figure 5.7 illustrates the competition between the three fluorescence centres at high, medium, and low concentrations in the proposed mechanism.

5. 3. Quantum yields of N-CD samples

For measurement of quantum yield in our N-CDs, quinine sulphate was used as the reference. The UV-visible absorbance spectrum of QS and the sample solutions were recorded for at least five different concentrations with the maxima between 0 to 0.1. The sample solutions were excited at 340 nm, and their fluorescence spectra were recorded. Thereafter, the areas under the curves (integrated fluorescence intensity) were calculated and plotted a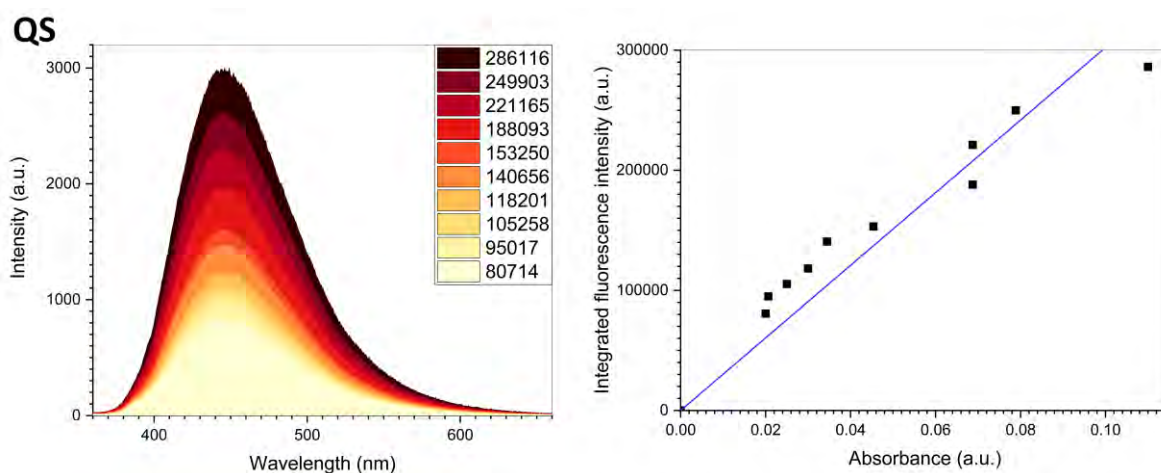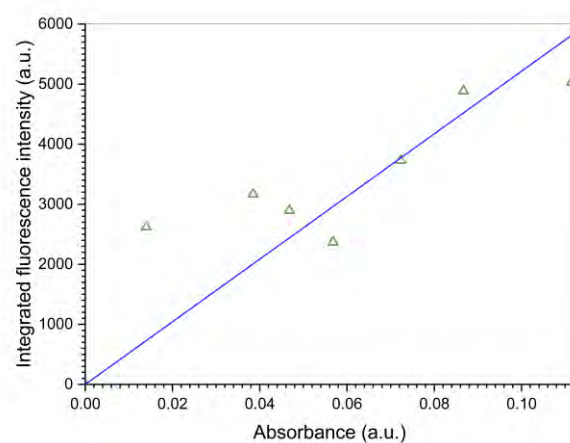gainst their corresponding absorbance (Figure 5.8). The slopes of interpolated lines passing the intercept of zero were calculated for each sample. Figure 5.9 illustrates the interpolated lines of all the samples for quantum yield measurements all in one plot. Numbers in the legend in Figure 5.9 reflects the term $Grad_{sam}/Grad_{ref}$ in the following equation through which quantum yields were calculated.

Equation 5.1.
$$\Phi_{sam} = \Phi_{ref} \times \frac{Grad_{sam}}{Grad_{ref}} \times \frac{\eta_{sam}^2}{\eta_{ref}^2}$$

The subscripts "sam" and "ref" stands for samples and reference, respectively. Φ is the emission quantum yield, Grad is the slope of the lines, η is the refractive index of the solvents. Since all the measurements for either of the reference and the samples were performed in water, the term related to refractive indices cancels out.
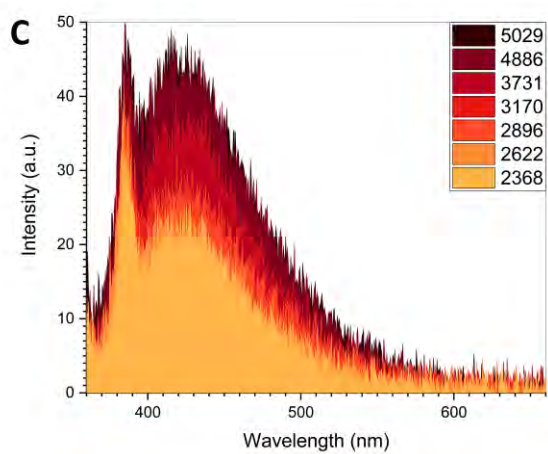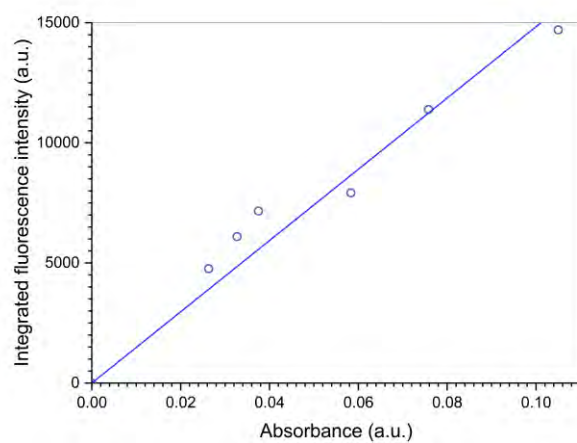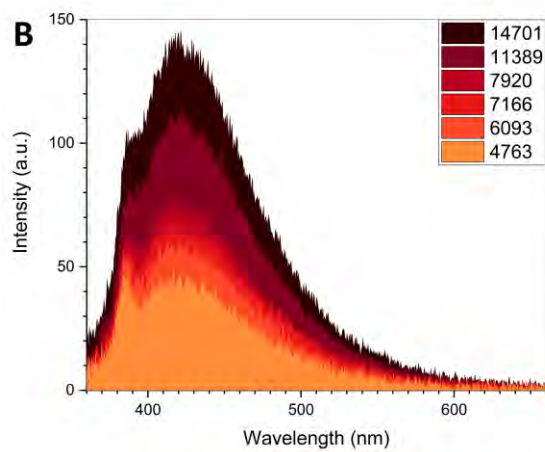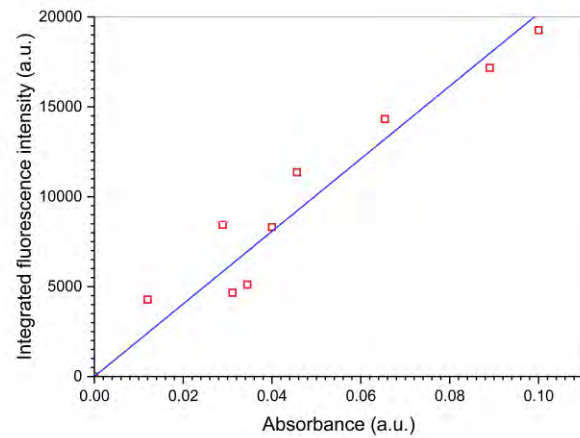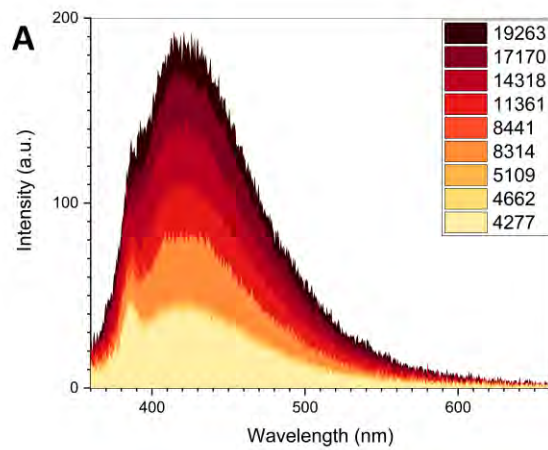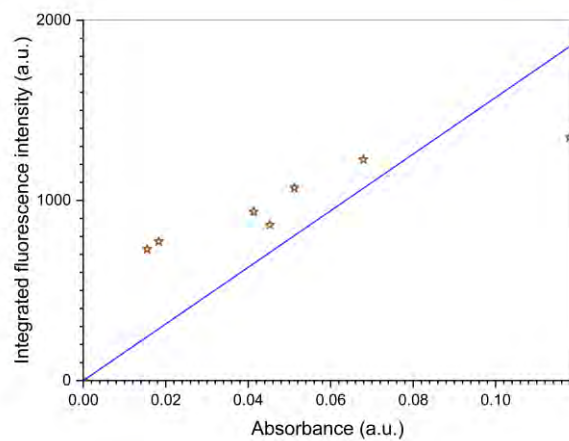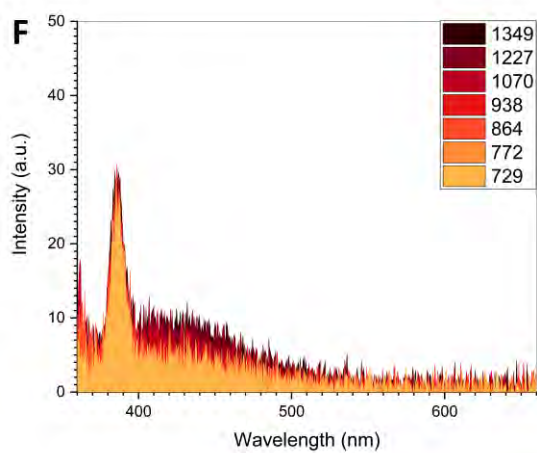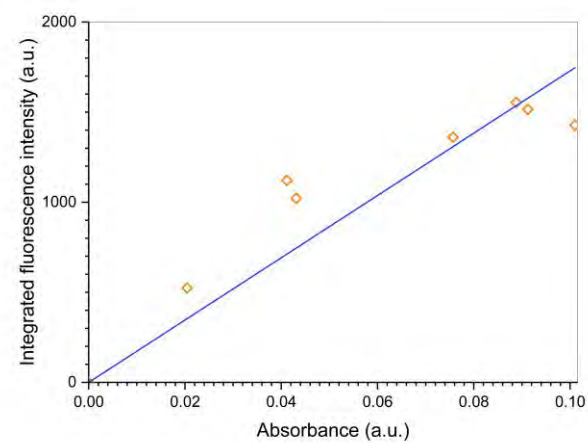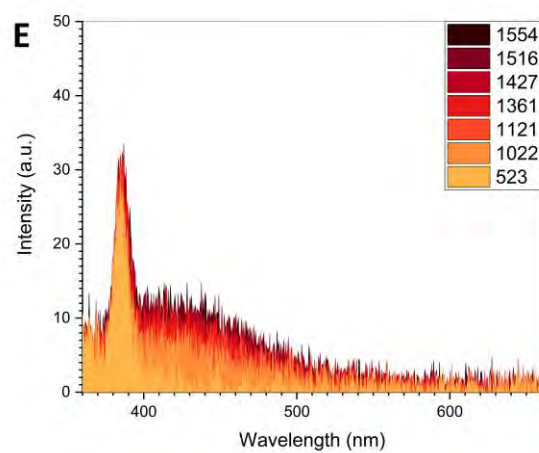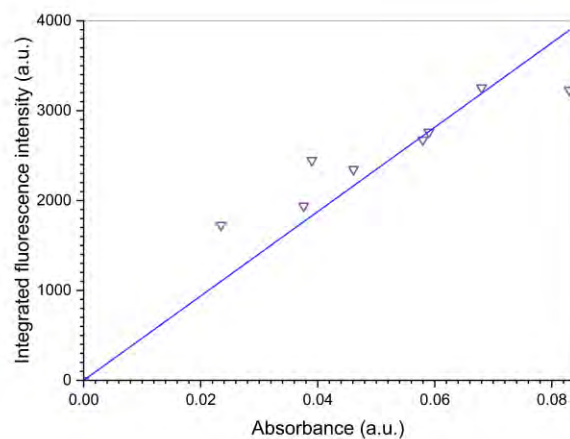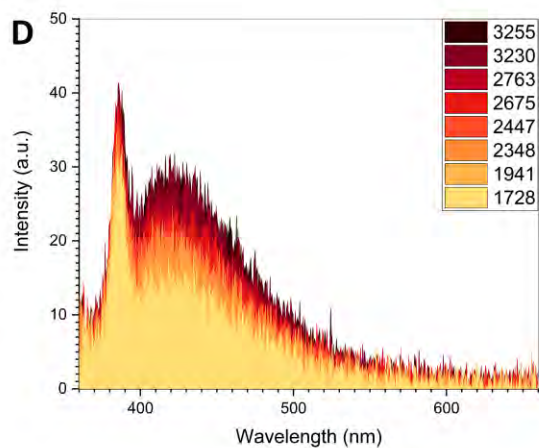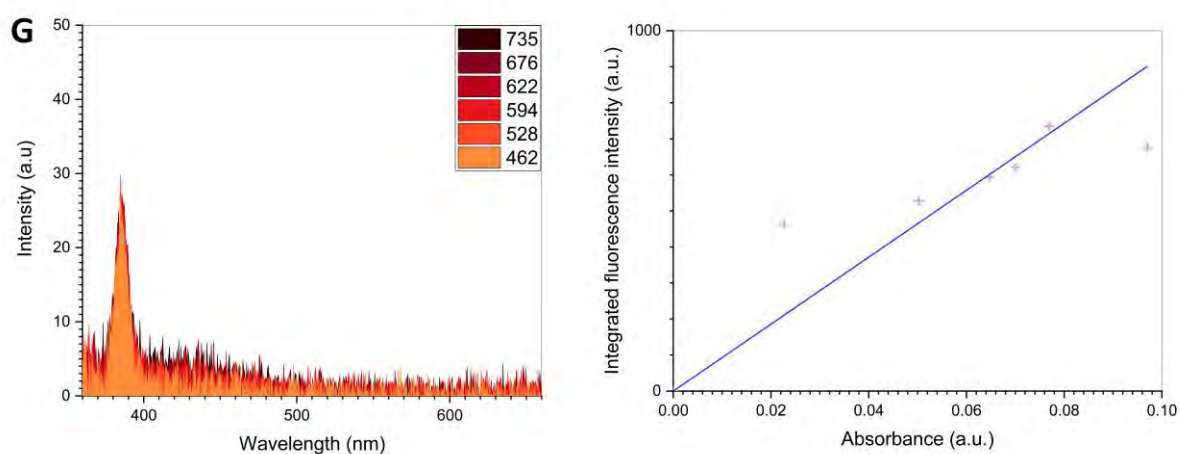
Figure 5.8. Integrated fluorescence intensities of quinine sulphate and (A-G) N-CD samples calculated and plotted against their corresponding absorbance.
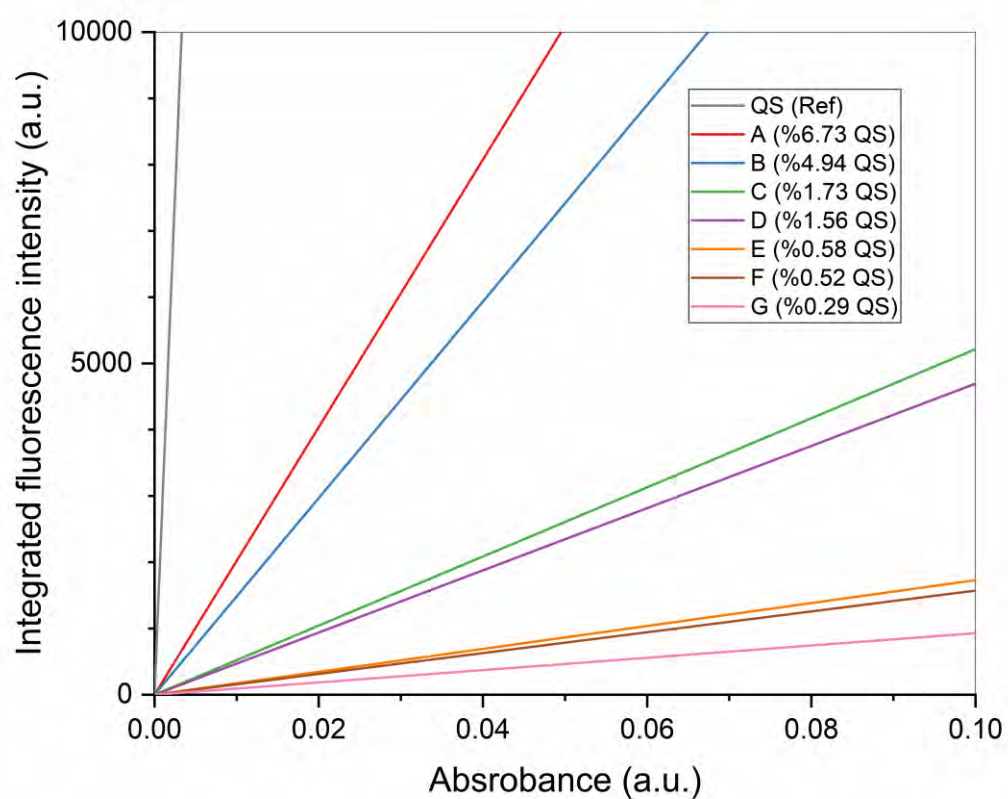
Figure 5.9. Interpolated lines for (A-G) N-CDs for quantum yield calculations.

Chapter 6 The effects of nitrogen doping on electronic properties of carbon dots

6. 1. Fluorescence lifetime measurement result of the N-CDs

To investigate the photoluminescence dynamics of N-CDs, seven samples with concentrations adjusted at the absorption maxima of 0.1 - the same ones used for absorption spectroscopy - underwent time correlated single photon counting measurements. These measurements were performed at the excitation and emission wavelengths of 367 and 450 nm, respectively. For interpretation of the data obtained here shown in Figure 6.1, each decay curve was fitted with a bi-exponential function. The instrument response function, decay curve and the fitted model for (A-G) N-CDs samples are shown in Figure 6.2(A-G). The fitted parameters are summarized in Table 6.1. This table shows the average relaxation time (τ_{av}) that comprises of long (τ_1) and short (τ_2) decays with their corresponding contribution in percentages. The average fluorescence lifetime has the maximum value in sample D, where both τ_1 and τ_2 are at their highest with 40.25% and 59.75% share of contribution, respectively. All the three values of delay time tend to reduce consistently from the optimum value of sample D as the nitrogen content increases or decreases in the system.
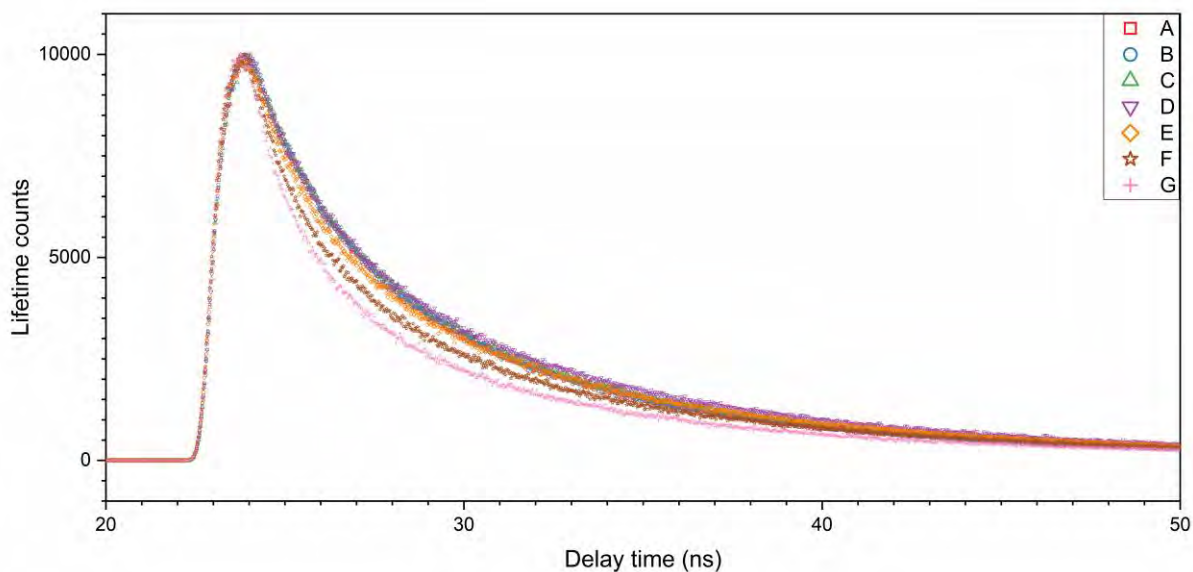
Figure 6.1. Fluorescence decay curves of (A-G) N-CDs samples.

Table 6.1. Summary of fluorescence lifetimes of (A-G) N-CDs samples

	τ_1 (ns)	P_1	τ_2 (ns)	P_2	τ_{av} (ns)
A	3.31	63.14%	0.79	36.86%	1.52
B	3.33	60.43%	0.82	39.57%	1.5
C	4.33	47.50%	1.13	52.50%	1.75
D	6.03	40.25%	1.29	59.75%	1.89
E	5.54	44.54%	1.1	55.46%	1.71
F	5.96	34.31%	1.05	65.69%	1.47
G	4.87	31.20%	0.9	68.80%	1.2

An interesting trend in this table is that from samples G to A, the contribution of slow relaxation (P_1) increases, and the share of fast relaxation (P_2) decreases consistently. In other words, the major contribution from the short decay component in samples with less doped nitrogen whose core is more naked strongly suggests this fast relaxation belongs to photogenerated carriers from the sp^2 domain. On the other hand, the major role of the slow relaxation in highly nitrogen-doped samples whose core is buried

under functional groups is attributed to recombination inside surface/edge states. The coexistence of both slow and fast decays is in agreement with the established core-surface model for the intrinsic-extrinsic origin of fluorescence [158]. The results of this section provide some evidence to respond to the question of either the core or edge/surface states possess the dominant role in the evolution of fluorescence in N-CDs. The short answer is that it depends on the degree of doping; in highly nitrogen-doped CDs it is the edge/surface which plays the more dominant role, but in CDs of low nitrogen doping, the carbon core may have a stronger influence on the fluorescence emission.
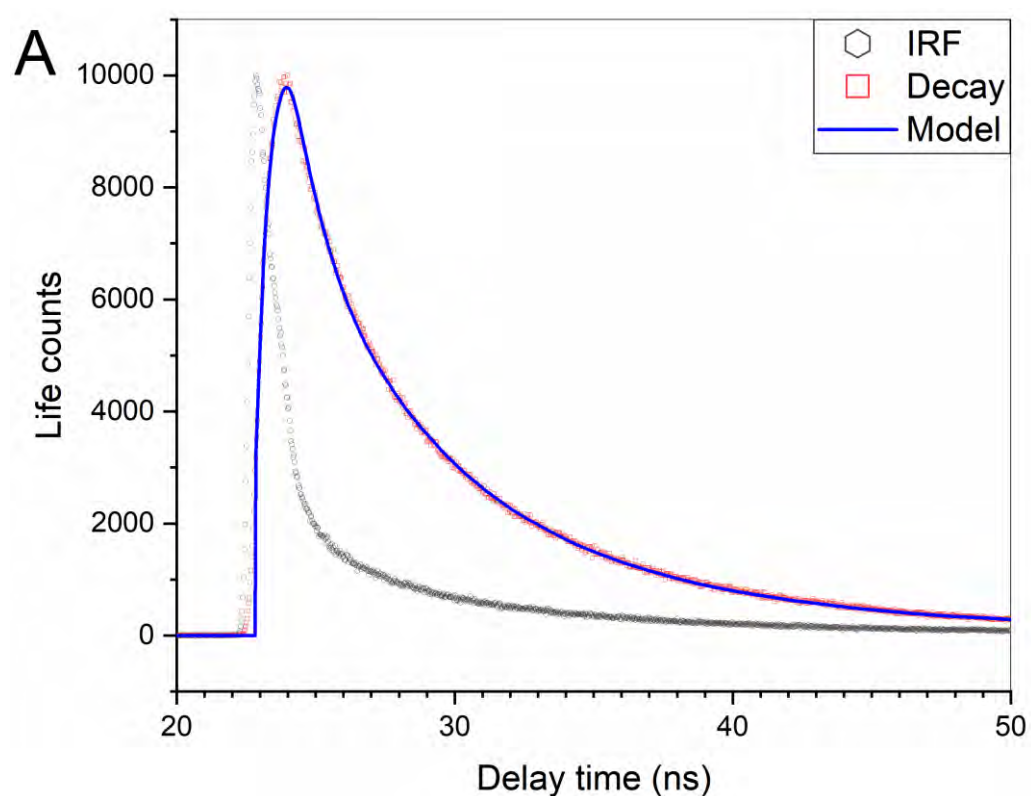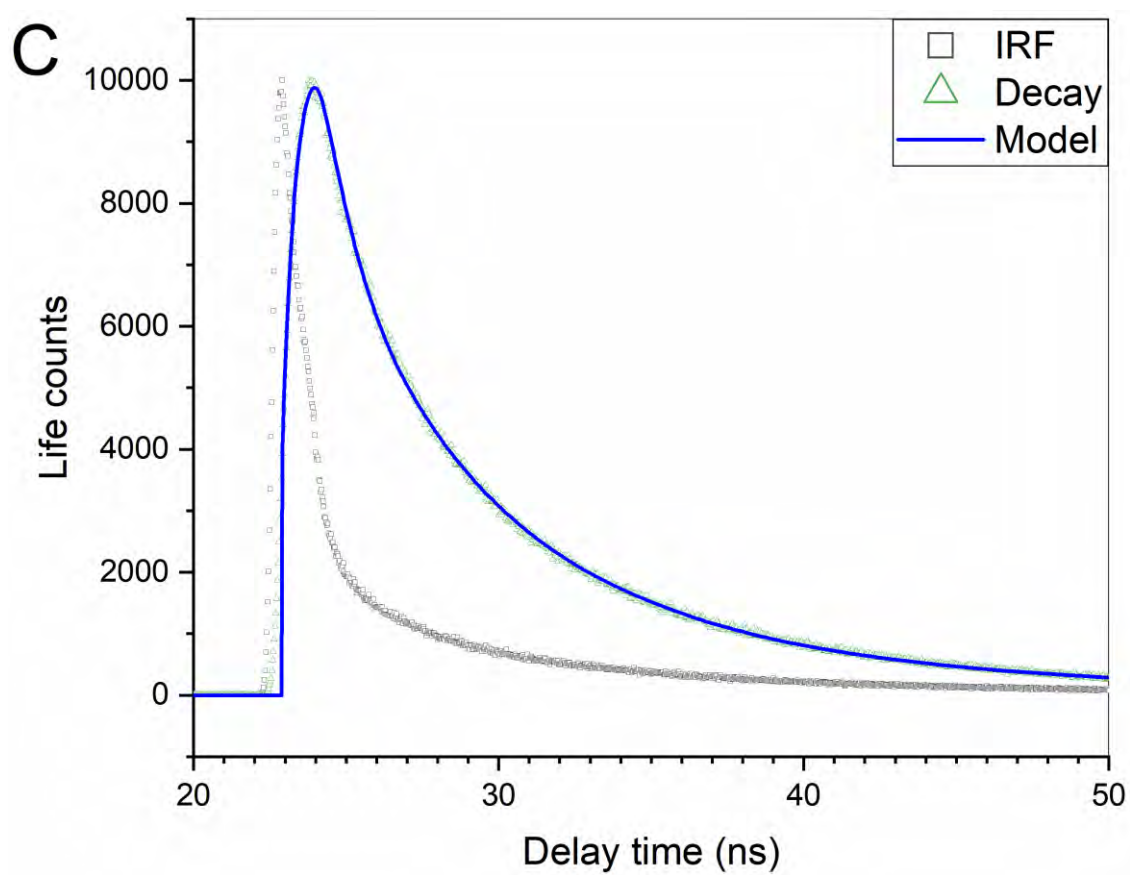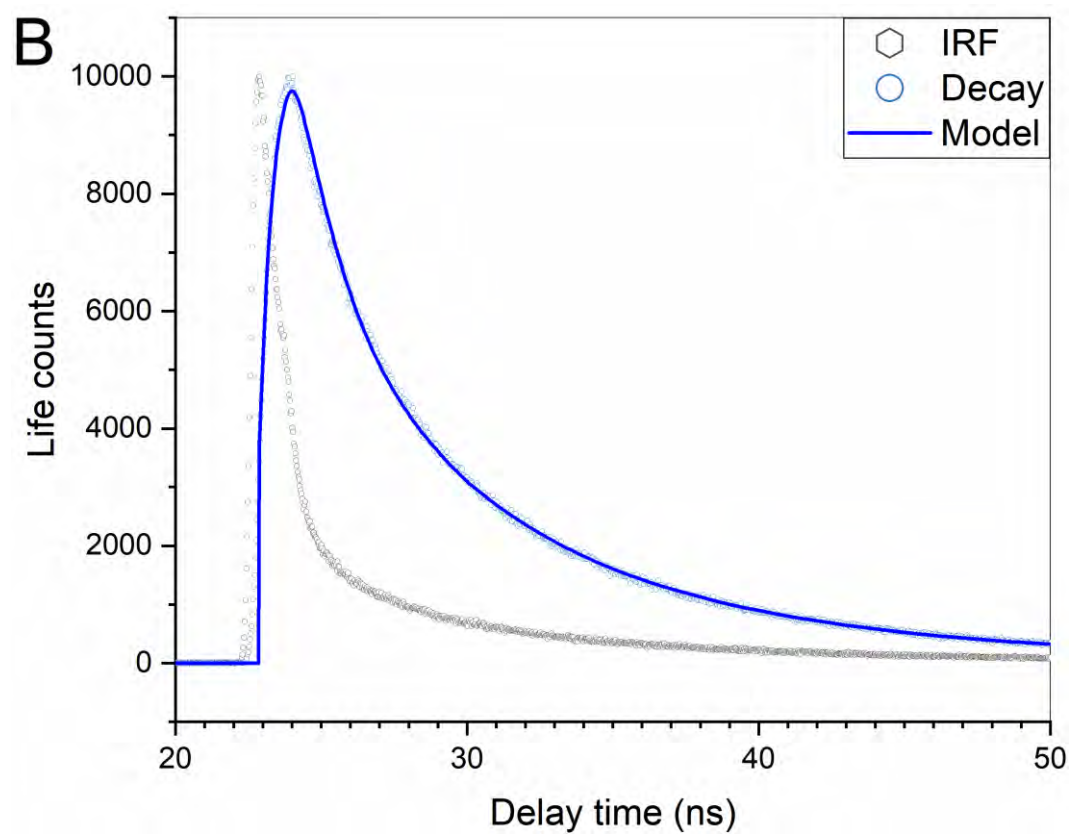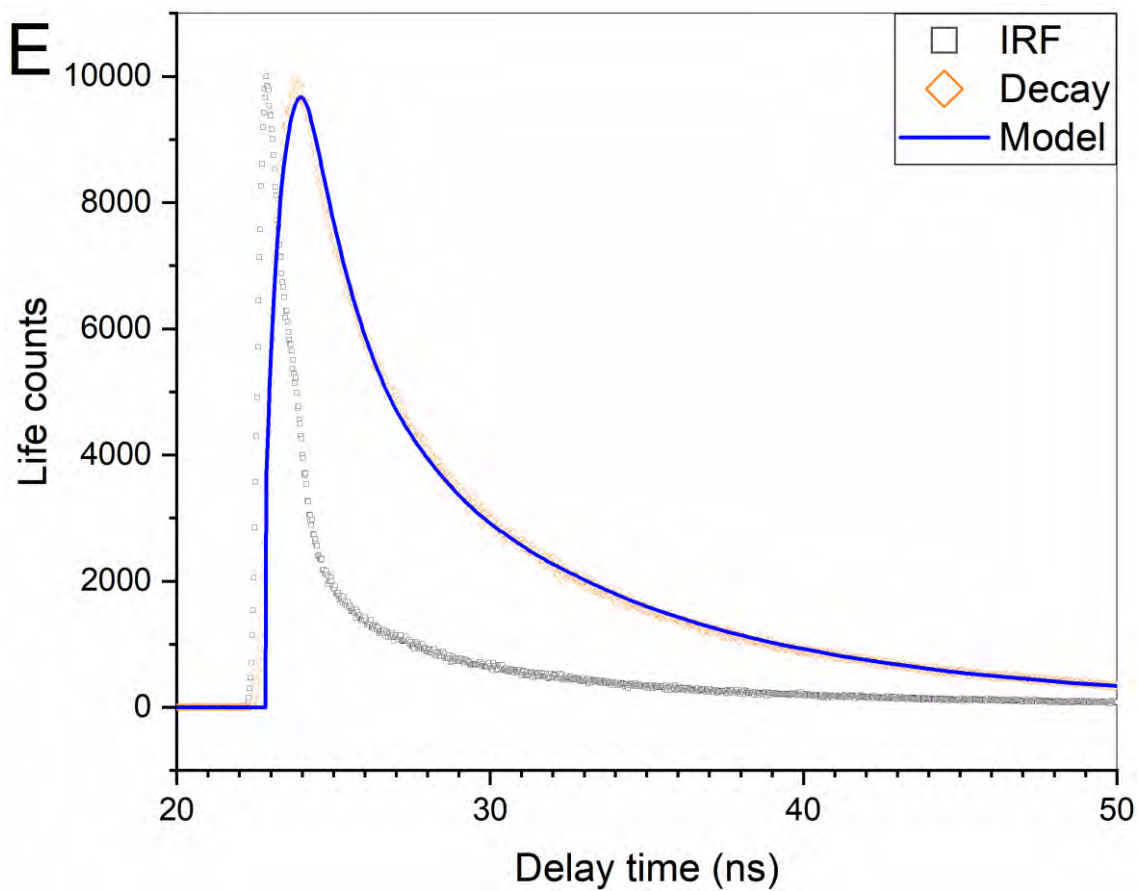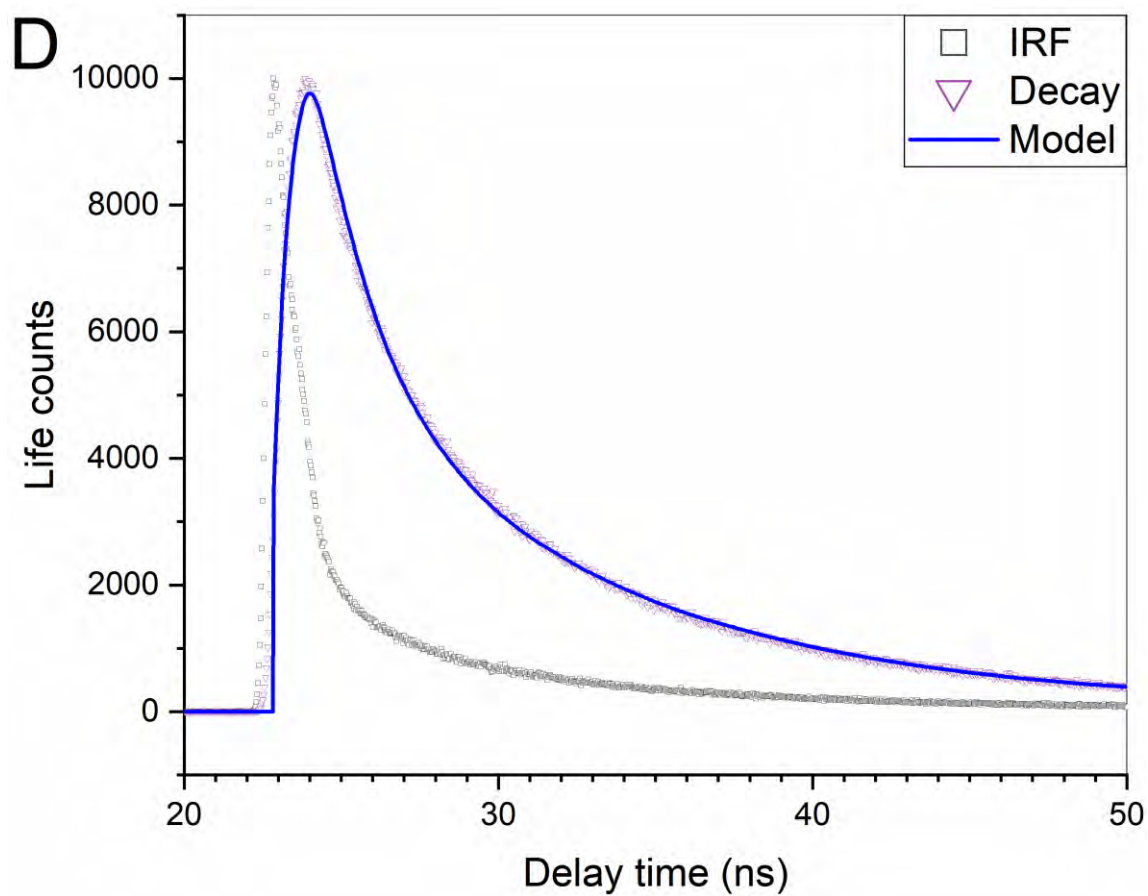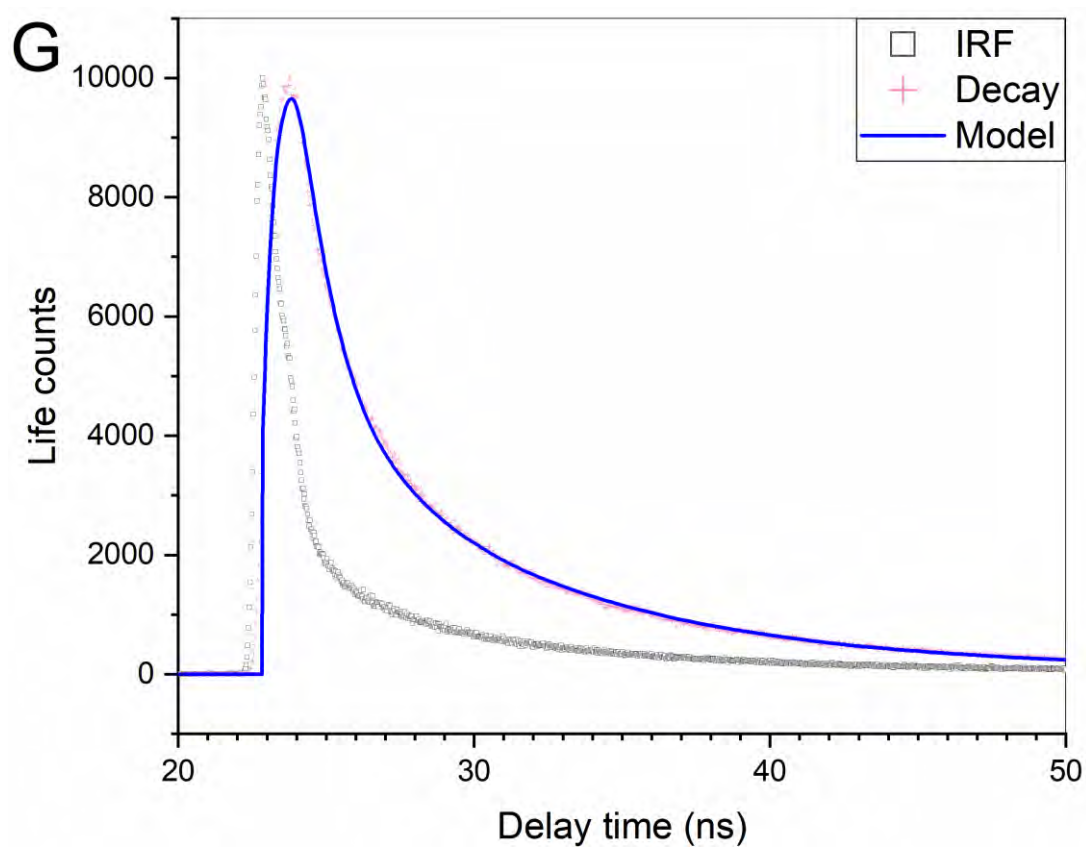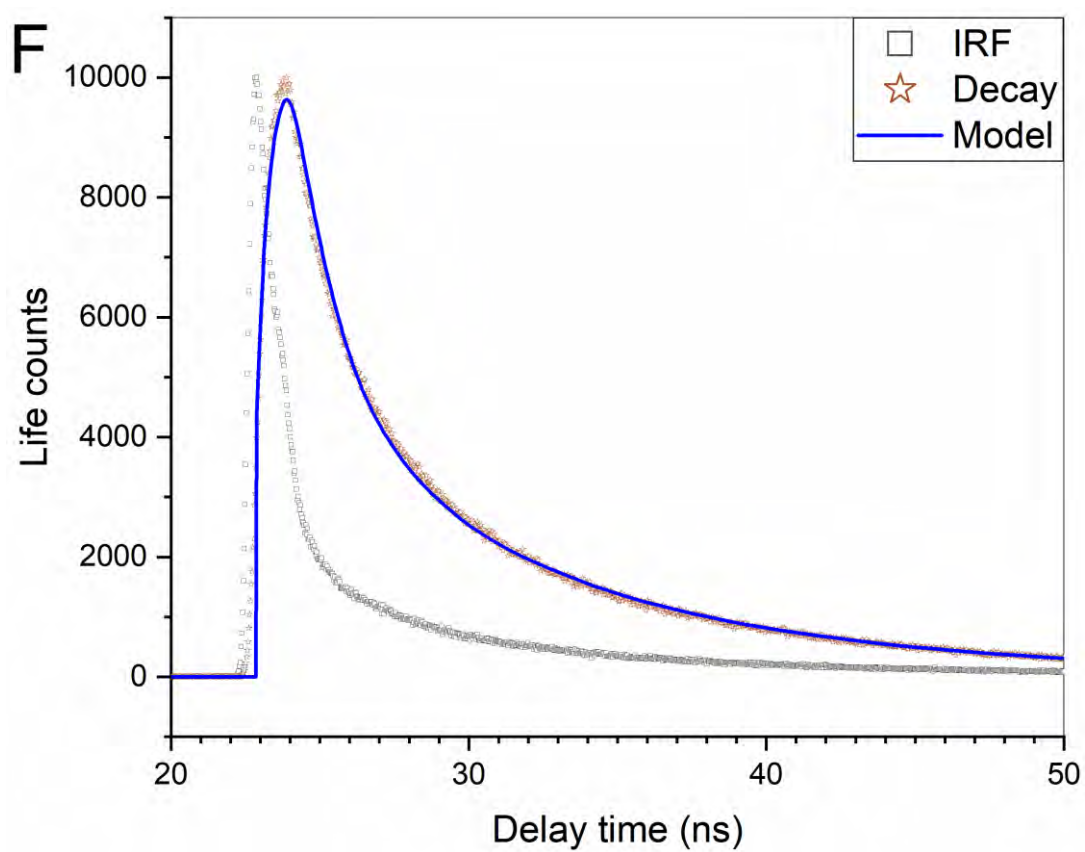
Figure 6.2. Instrument response function, decay, and the fitted model for (A-G) N-CDs samples.

6. 2. Hall effect measurement results of the freeze-dried N-CDs

The results from the Hall effect and resistivity measurements are summarized in Table 6.2. It is surprising to observe that in samples A and B the sign of Hall voltage is negative, whereas for the rest of N-CDs this sign is positive. The negativity of the Hall sign in highly nitrogen-doped samples of A and B indicates that electrons are the majority carriers responsible for the electronic transport in these N-CDs. This is with the argument that nitrogen provides excess electrons for CDs. A similar phenomenon has been observed in a comparative study of pristine and nitrogen-doped graphene sheets, as the pristine graphene with ambipolar transport behaviour shows n-type semiconducting characteristics when doped with nitrogen [159]. The positive sign of the Hall mobility for samples G to C is likely due to the increased oxygen content in the material when less doped with nitrogen. The values of Hall mobility and majority carrier density are in order of 30-470 ($cm^2V^{-1}s^{-1}$) and 1-5E11 (cm^{-3}) respectively, with no specific relation to the nitrogen content in the material. The large variability in these numbers may be due to the low conductivity and existence of the varied amounts of water in different samples after freeze-drying.

Table 6.2. Summary of parameters from Hall effect and resistivity measurements

	Hall mobility ($cm^2V^{-1}s^{-1}$)	Resistivity (Ohm cm)	Bulk carrier density (cm^{-3})
A	-303	9.884×10^4	2.07×10^{11}
B	-119	1.49×10^5	3.51×10^{11}
C	472	9.12×10^4	4.82×10^{11}
D	120	1.9×10^5	2.75×10^{11}
E	185	3.22×10^5	1.04×10^{11}
F	29	2.17×10^6	9.65×10^{10}
G	68	4.87×10^5	1.86×10^{11}

Chapter 7 Conclusion

In summary, concentration induced multi-colour CDs were synthesized by varying the degree of nitrogen doping via the change of citric acid to urea ratio in the precursors. The effects of nitrogen doping on chemical, optical and electronic properties of CDs were systematically characterized. The absorption spectra showed that nitrogen states are responsible for the reddest component of the emission. The excitation independency of the blue component in excitation-emission matrices evidenced for existence of molecular fluorescence. Three major fluorescence centres were identified in excitation-emission matrices of the seven samples. Based on the information from the analyses, a plausible mechanism for fluorescence emission in CDs were proposed in which the blue, green, and yellow centres were attributed to molecular fluorescence, core, and surface states emission, respectively. It is intriguing to observe that N-doping does not always result in n-type carbon dots-film. For the carbon dots synthesized in this study, there are considerable amount of oxygen element in the material, which may dominate the state of charge carriers at certain concentration ratio. The insights acquired here are instructive for designing carbon dots, and optical and electronic devices based on them.

Solvothermal method of synthesizing carbon dots is simple, cost effective, environment friendly, and scalable for mass production. A variety of precursors including waste and biowaste materials can be used in solvothermal synthesis of carbon dots. However, carbon dots synthesized with this method are not uniform in size and may have impurities.

References

1. Schneider, J., et al., *Molecular fluorescence in citric acid-based carbon dots.* The Journal of Physical Chemistry C, 2017. **121**(3): p. 2014-2022.
2. Sharma, A., et al., *Molecular origin and self-assembly of fluorescent carbon nanodots in polar solvents.* The journal of physical chemistry letters, 2017. **8**(5): p. 1044-1052.
3. Mintz, K.J., Y. Zhou, and R.M. Leblanc, *Recent development of carbon quantum dots regarding their optical properties, photoluminescence mechanism, and core structure.* Nanoscale, 2019. **11**(11): p. 4634-4652.
4. Alizadeh-Ghodsi, M., et al., *State-of-the-Art and Trends in Synthesis, Properties, and Application of Quantum Dots-Based Nanomaterials.* Particle & Particle Systems Characterization, 2019. **36**(2): p. 1800302.
5. Smyder, J.A. and T.D. Krauss, *Coming attractions for semiconductor quantum dots.* Materials Today, 2011. **14**(9): p. 382-387.
6. Zhang, Y.-Q., et al., *N-doped carbon quantum dots for TiO2-based photocatalysts and dye-sensitized solar cells.* Nano Energy, 2013. **2**(5): p. 545-552.
7. Essner, J.B. and G.A. Baker, *The emerging roles of carbon dots in solar photovoltaics: a critical review.* Environmental Science: Nano, 2017. **4**(6): p. 1216-1263.
8. Singh, A., et al., *Carbon dots derived from human hair for ppb level chloroform sensing in water.* Sustainable Materials and Technologies, 2020. **25**: p. e00159.
9. Pham, N.D., et al., *Self-assembled carbon dot-wrapped perovskites enable light trapping and defect passivation for efficient and stable perovskite solar cells.* Journal of Materials Chemistry A, 2021. **9**(12): p. 7508-7521.
10. Wang, X., et al., *Bandgap-Like strong fluorescence in functionalized carbon nanoparticles.* Angewandte Chemie International Edition, 2010. **49**(31): p. 5310-5314.
11. Yan, X., et al., *Independent tuning of the band gap and redox potential of graphene quantum dots.* The journal of physical chemistry letters, 2011. **2**(10): p. 1119-1124.
12. Park, Y., et al., *Biocompatible nitrogen-doped carbon dots: synthesis, characterization, and application.* Journal of Materials Chemistry B, 2020. **8**(39): p. 8935-8951.
13. Du, Y. and S. Guo, *Chemically doped fluorescent carbon and graphene quantum dots for bioimaging, sensor, catalytic and photoelectronic applications.* Nanoscale, 2016. **8**(5): p. 2532-2543.
14. Zhu, Z., et al., *Red carbon dots: Optical property regulations and applications.* Materials Today, 2019. **30**: p. 52-79.
15. Park, Y., et al., *Improving the functionality of carbon nanodots: doping and surface functionalization.* Journal of Materials Chemistry A, 2016. **4**(30): p. 11582-11603.
16. Zhang, Y.-Q., et al., *One-pot synthesis of N-doped carbon dots with tunable luminescence properties.* Journal of Materials Chemistry, 2012. **22**(33): p. 16714-16718.
17. Guo, L., et al., *Tunable multicolor carbon dots prepared from well-defined polythiophene derivatives and their emission mechanism.* Nanoscale, 2016. **8**(2): p. 729-734.
18. Green, R., *Hall effect measurements in materials characterization.* White paper, 2011(3111).
19. Scheele, M., *To be or not to be: Band-like transport in quantum dot solids.* Zeitschrift für Physikalische Chemie, 2015. **229**(1-2): p. 167-178.
20. Singh, A., et al., *Biowaste-Derived, Self-Organized Arrays of High-Performance 2D Carbon Emitters for Organic Light-Emitting Diodes.* Advanced Materials, 2020. **32**(10): p. 1906176.

21.   Jang, J., et al., *Temperature-dependent Hall and field-effect mobility in strongly coupled all-inorganic nanocrystal arrays.* Nano letters, 2014. **14**(2): p. 653-662.

22.   Yuan, F., et al., *Multicolor fluorescent graphene quantum dots colorimetrically responsive to all-pH and a wide temperature range.* Nanoscale, 2015. **7**(27): p. 11727-11733.

23.   Ding, H., et al., *Solvent-controlled synthesis of highly luminescent carbon dots with a wide color gamut and narrowed emission peak widths.* Small, 2018. **14**(22): p. 1800612.

24.   Miao, X., et al., *Synthesis of carbon dots with multiple color emission by controlled graphitization and surface functionalization.* Advanced materials, 2018. **30**(1): p. 1704740.

25.   Zhang, F., et al., *Effect of lateral size of graphene quantum dots on their properties and application.* ACS applied materials & interfaces, 2016. **8**(3): p. 2104-2110.

26.   Bao, L., et al., *Photoluminescence-tunable carbon nanodots: surface-state energy-gap tuning.* Advanced Materials, 2015. **27**(10): p. 1663-1667.

27.   Li, H., et al., *Water-soluble fluorescent carbon quantum dots and photocatalyst design.* Angewandte Chemie, 2010. **122**(26): p. 4532-4536.

28.   Mu, Y., et al., *Carbogenic nanodots derived from organo-templated zeolites with modulated full-color luminescence.* Chemical science, 2016. **7**(6): p. 3564-3568.

29.   Chen, Y.-C., et al., *Pseudo-multicolor carbon dots emission and the dilution-induced reversible fluorescence shift.* RSC advances, 2016. **6**(50): p. 44024-44028.

30.   Meng, X., et al., *Full-colour carbon dots: from energy-efficient synthesis to concentration-dependent photoluminescence properties.* Chemical communications, 2017. **53**(21): p. 3074-3077.

31.   Wang, C., et al., *Concentration-dependent color tunability of nitrogen-doped carbon dots and their application for iron (III) detection and multicolor bioimaging.* Journal of colloid and interface science, 2018. **521**: p. 33-41.

32.   Chen, Y., et al., *Concentration-induced multi-colored emissions in carbon dots: origination from triple fluorescent centers.* Nanoscale, 2018. **10**(14): p. 6734-6743.

33.   Wang, X., et al., *Concentration-tuned multicolor carbon dots: microwave-assisted synthesis, characterization, mechanism and applications.* New Journal of Chemistry, 2019. **43**(23): p. 8950-8957.

34.   Su, Y., Z. Xie, and M. Zheng, *Carbon dots with concentration-modulated fluorescence: Aggregation-induced multicolor emission.* Journal of Colloid and Interface Science, 2020.

35.   Lai, S., et al., *Mechanisms behind excitation-and concentration-dependent multicolor photoluminescence in graphene quantum dots.* Nanoscale, 2020. **12**(2): p. 591-601.

36.   Xu, X., et al., *Electrophoretic analysis and purification of fluorescent single-walled carbon nanotube fragments.* Journal of the American Chemical Society, 2004. **126**(40): p. 12736-12737.

37.   Essner, J.B. and G.A. Baker, *The emerging roles of carbon dots in solar photovoltaics: a critical review.* Environmental Science: Nano, 2017.

38.   Sun, Y.-P., et al., *Quantum-sized carbon dots for bright and colorful photoluminescence.* J. Am. Chem. Soc, 2006. **128**(24): p. 7756-7757.

39.   Zhou, J., et al., *An electrochemical avenue to blue luminescent nanocrystals from multiwalled carbon nanotubes (MWCNTs).* Journal of the American Chemical Society, 2007. **129**(4): p. 744-745.

40.   Essner, J.B., C.H. Laber, and G.A. Baker, *Carbon dot reduced bimetallic nanoparticles: size and surface plasmon resonance tunability for enhanced catalytic applications.* Journal of Materials Chemistry A, 2015. **3**(31): p. 16354-16360.

41.   Zhang, T., et al., *Facilely prepared carbon dots and rare earth ion doped hybrid composites for ratio-metric pH sensing and white-light emission.* RSC Advances, 2016. **6**(66): p. 61468-61472.

42.   Qu, S., et al., *A Biocompatible Fluorescent Ink Based on Water-Soluble Luminescent Carbon Nanodots.* Angewandte Chemie, 2012. **124**(49): p. 12381-12384.

43. Wang, X., et al., *Bandgap-Like Strong Fluorescence in Functionalized Carbon Nanoparticles.* Angewandte Chemie, 2010. **122**(31): p. 5438-5442.

44. Ye, R., et al., *Bandgap engineering of coal-derived graphene quantum dots.* ACS applied materials & interfaces, 2015. **7**(12): p. 7041-7048.

45. Jin, S.H., et al., *Tuning the photoluminescence of graphene quantum dots through the charge transfer effect of functional groups.* ACS nano, 2013. **7**(2): p. 1239-1245.

46. Ding, H., et al., *Full-color light-emitting carbon dots with a surface-state-controlled luminescence mechanism.* Acs Nano, 2015. **10**(1): p. 484-491.

47. Dong, Q.-R., *Electrical linear control of the electronic structure of graphene quantum dots.* Journal of Applied Physics, 2013. **113**(23): p. 234304.

48. Zhang, Z., K. Chang, and F. Peeters, *Tuning of energy levels and optical properties of graphene quantum dots.* Physical Review B, 2008. **77**(23): p. 235411.

49. Sheng, W.-d., et al., *Electronic and optical properties of semiconductor and graphene quantum dots.* Frontiers of Physics, 2012. **7**(3): p. 328-352.

50. Cayuela, A., et al., *Semiconductor and carbon-based fluorescent nanodots: the need for consistency.* Chemical Communications, 2016. **52**(7): p. 1311-1326.

51. Margraf, J., et al., *Using carbon nanodots as inexpensive and environmentally friendly sensitizers in mesoscopic solar cells.* Nanoscale Horizons, 2016. **1**(3): p. 220-226.

52. Yan, X., et al., *Large, solution-processable graphene quantum dots as light absorbers for photovoltaics.* Nano letters, 2010. **10**(5): p. 1869-1873.

53. Shalini, S., et al., *Status and outlook of sensitizers/dyes used in dye sensitized solar cells (DSSC): a review.* International Journal of Energy Research, 2016. **40**(10): p. 1303-1320.

54. Liu, J., et al., *Three dimensional carbogenic dots/TiO 2 nanoheterojunctions with enhanced visible light-driven photocatalytic activity.* Carbon, 2014. **79**: p. 369-379.

55. Wang, H.-X., et al., *Rational design of nitrogen and sulfur co-doped carbon dots for efficient photoelectrical conversion applications.* Journal of Materials Chemistry A, 2015. **3**(21): p. 11287-11293.

56. Wang, S., I.S. Cole, and Q. Li, *Quantum-confined bandgap narrowing of TiO 2 nanoparticles by graphene quantum dots for visible-light-driven applications.* Chemical Communications, 2016. **52**(59): p. 9208-9211.

57. Wang, F., et al., *Opto-electronic conversion logic behaviour through dynamic modulation of electron/energy transfer states at the TiO 2–carbon quantum dot interface.* Nanoscale, 2013. **5**(5): p. 1831-1835.

58. Nazeeruddin, M.K., E. Baranoff, and M. Grätzel, *Dye-sensitized solar cells: a brief overview.* Solar Energy, 2011. **85**(6): p. 1172-1178.

59. Mirtchev, P., et al., *Solution phase synthesis of carbon quantum dots as sensitizers for nanocrystalline TiO 2 solar cells.* Journal of Materials Chemistry, 2012. **22**(4): p. 1265-1269.

60. Zhang, H., et al., *A fluorescent quenching performance enhancing principle for carbon nanodot-sensitized aqueous solar cells.* Nano Energy, 2015. **13**: p. 124-130.

61. Fang, X., et al., *Graphene quantum dots optimization of dye-sensitized solar cells.* Electrochimica Acta, 2014. **137**: p. 634-638.

62. Mueller, M.L., et al., *Slow hot-carrier relaxation in colloidal graphene quantum dots.* Nano letters, 2010. **11**(1): p. 56-60.

63. Yu, P., et al., *Efficient electron transfer in carbon nanodot–graphene oxide nanocomposites.* Journal of Materials Chemistry C, 2014. **2**(16): p. 2894-2901.

64. Williams, K.J., et al., *Hot electron injection from graphene quantum dots to TiO2.* ACS nano, 2013. **7**(2): p. 1388-1394.

65. Chen, L., et al., *Graphene quantum-dot-doped polypyrrole counter electrode for high-performance dye-sensitized solar cells.* ACS applied materials & interfaces, 2013. **5**(6): p. 2047-2052.

66. Huang, Z., et al., *Facile synthesis of analogous graphene quantum dots with sp 2 hybridized carbon atom dominant structures and their photovoltaic application.* Nanoscale, 2014. **6**(21): p. 13043-13052.

67. Zhao, J., et al., *Fabrication and properties of a high-performance chlorine doped graphene quantum dot based photovoltaic detector.* RSC Advances, 2015. **5**(37): p. 29222-29229.

68. Zhao, J., et al., *Chlorine doped graphene quantum dots: Preparation, properties, and photovoltaic detectors.* Applied Physics Letters, 2014. **105**(11): p. 111116.

69. Privitera, A., et al., *Boosting carbon quantum dots/fullerene electron transfer via surface group engineering.* Physical Chemistry Chemical Physics, 2016. **18**(45): p. 31286-31295.

70. Feng, X., et al., *Low-Temperature Hydrothermal Synthesis of Green Luminescent Carbon Quantum Dots (CQD), and Optical Properties of Blends of the CQD with Poly (3-hexylthiophene).* Journal of Electronic Materials, 2015. **44**(10): p. 3436-3443.

71. Wang, D.H., et al., *Efficient solution-processed small-molecule solar cells by insertion of graphene quantum dots.* Nanoscale, 2014. **6**(24): p. 15175-15180.

72. Moon, B.J., et al., *Facile and purification-free synthesis of nitrogenated amphiphilic graphitic carbon dots.* Chemistry of Materials, 2016. **28**(5): p. 1481-1488.

73. Ding, Z., et al., *Few-layered graphene quantum dots as efficient hole-extraction layer for high-performance polymer solar cells.* Nano Energy, 2015. **15**: p. 186-192.

74. Li, M., et al., *Graphene quantum dots as the hole transport layer material for high-performance organic solar cells.* Physical Chemistry Chemical Physics, 2013. **15**(43): p. 18973-18978.

75. Lim, H.C., et al., *Self-assembled poly (3, 4-ethylene dioxythiophene): poly (styrenesulfonate)/graphene quantum dot organogels for efficient charge transport in photovoltaic devices.* ACS applied materials & interfaces, 2015. **7**(21): p. 11069-11073.

76. Yang, H.B., et al., *Graphene quantum dots-incorporated cathode buffer for improvement of inverted polymer solar cells.* Solar Energy Materials and Solar Cells, 2013. **117**: p. 214-218.

77. Qin, Y., et al., *Top-down strategy toward versatile graphene quantum dots for organic/inorganic hybrid solar cells.* ACS Sustainable Chemistry & Engineering, 2015. **3**(4): p. 637-644.

78. Dutta, M., et al., *ZnO/graphene quantum dot solid-state solar cell.* The Journal of Physical Chemistry C, 2012. **116**(38): p. 20127-20131.

79. Briscoe, J., et al., *Biomass-Derived Carbon Quantum Dot Sensitizers for Solid-State Nanostructured Solar Cells.* Angewandte Chemie International Edition, 2015. **54**(15): p. 4463-4468.

80. Gao, P., et al., *Crystalline Si/graphene quantum dots heterojunction solar cells.* The Journal of Physical Chemistry C, 2014. **118**(10): p. 5164-5171.

81. Xie, C., et al., *Core–shell heterojunction of silicon nanowire arrays and carbon quantum dots for photovoltaic devices and self-driven photodetectors.* Acs Nano, 2014. **8**(4): p. 4015-4022.

82. Lee, K.D., et al., *Graphene quantum dot layers with energy-down-shift effect on crystalline-silicon solar cells.* ACS applied materials & interfaces, 2015. **7**(34): p. 19043-19049.

83. Han, X., et al., *A simple strategy for synthesizing highly luminescent carbon nanodots and application as effective down-shifting layers.* Nanotechnology, 2015. **26**(6): p. 065402.

84. Pelayo, E., et al., *Silicon solar cell efficiency improvement employing the photoluminescent, down-shifting effects of carbon and CdTe quantum dots.* Materials for Renewable and Sustainable Energy, 2016. **5**(2): p. 5.

85. Zhu, Z., et al., *Efficiency enhancement of perovskite solar cells through fast electron extraction: the role of graphene quantum dots.* Journal of the American Chemical Society, 2014. **136**(10): p. 3760-3763.

86. Paulo, S., et al., *Carbon quantum dots as new hole transport material for perovskite solar cells.* Synthetic Metals, 2016. **222**: p. 17-22.

87.   Ekimov, A.I. and A.A. Onushchenko, *Quantum size effect in three-dimensional microscopic semiconductor crystals.* Jetp Lett, 1981. **34**(6): p. 345-349.

88.   Hetsch, F., et al., *Quantum dot field effect transistors.* Materials Today, 2013. **16**(9): p. 312-325.

89.   Talapin, D.V., et al., *Prospects of colloidal nanocrystals for electronic and optoelectronic applications.* Chem. Rev, 2010. **110**(1): p. 389-458.

90.   Talapin, D.V. and C.B. Murray, *PbSe nanocrystal solids for n-and p-channel thin film field-effect transistors.* Science, 2005. **310**(5745): p. 86-89.

91.   Geyer, S., et al., *Charge transport in mixed CdSe and CdTe colloidal nanocrystal films.* Physical Review B, 2010. **82**(15): p. 155201.

92.   Hanrath, T., *Colloidal nanocrystal quantum dot assemblies as artificial solids.* Journal of Vacuum Science & Technology A: Vacuum, Surfaces, and Films, 2012. **30**(3): p. 030802.

93.   Kwon, W., et al., *Carbon quantum dot-based field-effect transistors and their ligand length-dependent carrier mobility.* ACS applied materials & interfaces, 2013. **5**(3): p. 822-827.

94.   Zhu, H., et al., *Graphene quantum dots directly generated from graphite via magnetron sputtering and the application in thin-film transistors.* Carbon, 2015. **88**: p. 225-232.

95.   Kim, Y., et al., *Graphene quantum dot (GQD)-induced photovoltaic and photoelectric memory elements in a pentacene/GQD field effect transistor as a probe of functional interface.* Journal of Physics D: Applied Physics, 2017. **50**(36): p. 365303.

96.   Tada, Y., et al., *Organic thin-film transistor memory with nanocrystal carbon dots.* e-Journal of Surface Science and Nanotechnology, 2010. **8**: p. 250-253.

97.   Kim, Y.-H., et al., *Characteristics of reduced graphene oxide quantum dots for a flexible memory thin film transistor.* ACS applied materials & interfaces, 2017. **9**(19): p. 16375-16380.

98.   Gupta, V., et al., *Luminscent graphene quantum dots for organic photovoltaic devices.* Journal of the American Chemical Society, 2011. **133**(26): p. 9960-9963.

99.   Wang, F., et al., *White light-emitting devices based on carbon dots' electroluminescence.* Chemical Communications, 2011. **47**(12): p. 3502-3504.

100.   Kwon, W., et al., *Electroluminescence from graphene quantum dots prepared by amidative cutting of tattered graphite.* Nano letters, 2014. **14**(3): p. 1306-1311.

101.   Zhang, X., et al., *Color-switchable electroluminescence of carbon dot light-emitting diodes.* ACS nano, 2013. **7**(12): p. 11234-11241.

102.   Singh, A., et al., *Biowaste-Derived, Self-Organized Arrays of High-Performance 2D Carbon Emitters for Organic Light-Emitting Diodes.* Advanced Materials, 2020. **32**(10).

103.   Fan, Z., et al., *Surrounding media sensitive photoluminescence of boron-doped graphene quantum dots for highly fluorescent dyed crystals, chemical sensing and bioimaging.* Carbon, 2014. **70**: p. 149-156.

104.   Feng, X., et al., *Luminescent carbon quantum dots with high quantum yield as a single white converter for white light emitting diodes.* Applied Physics Letters, 2015. **107**(21): p. 213102.

105.   Mao, L.-H., et al., *Facile access to white fluorescent carbon dots toward light-emitting devices.* Industrial & Engineering Chemistry Research, 2014. **53**(15): p. 6417-6425.

106.   Shen, C., et al., *Facile access to B-doped solid-state fluorescent carbon dots toward light emitting devices and cell imaging agents.* Journal of Materials Chemistry C, 2015. **3**(26): p. 6668-6675.

107.   Sun, M., et al., *Towards efficient solid-state photoluminescence based on carbon-nanodots and starch composites.* Nanoscale, 2014. **6**(21): p. 13076-13081.

108.   Tetsuka, H., A. Nagoya, and R. Asahi, *Highly luminescent flexible amino-functionalized graphene quantum dots@ cellulose nanofiber–clay hybrids for white-light emitting diodes.* Journal of Materials Chemistry C, 2015. **3**(15): p. 3536-3541.

109.   Zhang, W., et al., *Large-area color controllable remote carbon white-light light-emitting diodes.* Carbon, 2015. **85**: p. 344-350.

110. Sarswat, P.K. and M.L. Free, *Light emitting diodes based on carbon dots derived from food, beverage, and combustion wastes.* Physical Chemistry Chemical Physics, 2015. **17**(41): p. 27642-27652.

111. Chen, L., et al., *Fabrication of Carboxyl Group-Functionalized Carbon Quantum Dots and Its Transparent and Luminescent Epoxy Matrix Nanocomposites for White LED Encapsulation.* Macromolecular Materials and Engineering, 2015. **300**(12): p. 1232-1237.

112. Ma, L., et al., *Carbon dot-doped sodium borosilicate gel glasses with emission tunability and their application in white light emitting diodes.* Journal of Materials Chemistry C, 2015. **3**(26): p. 6764-6770.

113. Kim, T.H., et al., *Salt-embedded carbon nanodots as a UV and thermal stable fluorophore for light-emitting diodes.* Journal of Luminescence, 2014. **154**: p. 1-7.

114. Tang, L., et al., *Deep ultraviolet photoluminescence of water-soluble self-passivated graphene quantum dots.* ACS nano, 2012. **6**(6): p. 5102-5110.

115. Kim, T.H., et al., *Yellow-emitting carbon nanodots and their flexible and transparent films for white LEDs.* ACS applied materials & interfaces, 2016. **8**(48): p. 33102-33111.

116. Guo, X., et al., *Facile access to versatile fluorescent carbon dots toward light-emitting diodes.* Chemical Communications, 2012. **48**(21): p. 2692-2694.

117. Kwon, W., et al., *Freestanding luminescent films of nitrogen-rich carbon nanodots toward large-scale phosphor-based white-light-emitting devices.* Chemistry of Materials, 2013. **25**(9): p. 1893-1899.

118. Sun, C., et al., *High color rendering index white light emitting diodes fabricated from a combination of carbon dots and zinc copper indium sulfide quantum dots.* Applied Physics Letters, 2014. **104**(26): p. 261106.

119. Li, X., et al., *Intercrossed Carbon Nanorings with Pure Surface States as Low-Cost and Environment-Friendly Phosphors for White-Light-Emitting Diodes.* Angewandte Chemie International Edition, 2015. **54**(6): p. 1759-1764.

120. Chen, Y., et al., *A Self-Quenching-Resistant Carbon-Dot Powder with Tunable Solid-State Fluorescence and Construction of Dual-Fluorescence Morphologies for White Light-Emission.* Advanced Materials, 2016. **28**(2): p. 312-318.

121. Kwon, W., et al., *Control of photoluminescence of carbon nanodots via surface functionalization using para-substituted anilines.* Scientific reports, 2015. **5**: p. 12604.

122. Lim, S.Y., W. Shen, and Z. Gao, *Carbon quantum dots and their applications.* Chemical Society Reviews, 2015. **44**(1): p. 362-381.

123. Zhang, X., et al., *Highly sensitive humidity sensing properties of carbon quantum dots films.* Materials Research Bulletin, 2013. **48**(2): p. 790-794.

124. Hosseini, Z., et al., *A new approach to flexible humidity sensors using graphene quantum dots.* Journal of Materials Chemistry C, 2017. **5**(35): p. 8966-8973.

125. Alizadeh, T., et al., *A new hydrogen cyanide chemiresistor gas sensor based on graphene quantum dots.* International Journal of Environmental Analytical Chemistry, 2016. **96**(8): p. 763-775.

126. Gavgani, J.N., et al., *A room temperature volatile organic compound sensor with enhanced performance, fast response and recovery based on N-doped graphene quantum dots and poly (3, 4-ethylenedioxythiophene)–poly (styrenesulfonate) nanocomposite.* RSC Advances, 2015. **5**(71): p. 57559-57567.

127. Fardindoost, S., Z.S. Hosseini, and S. Hatamie, *Detecting hydrogen using graphene quantum dots/WO3 thin films.* Materials Research Express, 2016. **3**(11): p. 116407.

128. Chu, X., et al., *Preparation and gas-sensing properties of SnO2/graphene quantum dots composites via solvothermal method.* Journal of Materials Science, 2017: p. 1-11.

129. Chu, X., et al., *The acetic acid gas sensing properties of graphene quantum dots (GQDs)–ZnO nanocomposites prepared by hydrothermal method.* Journal of Materials Science: Materials in Electronics, 2017. **28**(24): p. 19164-19173.

130. Hu, J., et al., *Enhanced NO 2 sensing performance of reduced graphene oxide by in situ anchoring carbon dots.* Journal of Materials Chemistry C, 2017. **5**(27): p. 6862-6871.

131. Tang, L., et al., *Deep ultraviolet to near-infrared emission and photoresponse in layered n-doped graphene quantum dots.* ACS nano, 2014. **8**(6): p. 6312-6320.

132. Cheng, S.-H., et al., *All Carbon-Based Photodetectors: An eminent integration of graphite quantum dots and two dimensional graphene.* Scientific reports, 2013. **3**: p. 2694.

133. Van Tam, T., et al., *Ultraviolet light sensor based on graphene quantum dots/reduced graphene oxide hybrid film.* Sensors and Actuators A: Physical, 2015. **233**: p. 368-373.

134. Kim, C.O., et al., *High-performance graphene-quantum-dot photodetectors.* Scientific reports, 2014. **4**: p. 5603.

135. Chao, D., et al., *Graphene quantum dots coated VO2 arrays for highly durable electrodes for Li and Na ion batteries.* Nano letters, 2014. **15**(1): p. 565-573.

136. Zhu, C., et al., *Enhanced lithium storage performance of CuO nanowires by coating of graphene quantum dots.* Advanced Materials Interfaces, 2015. **2**(2).

137. Jing, M., et al., *Carbon quantum dot coated Mn 3 O 4 with enhanced performances for lithium-ion batteries.* Journal of Materials Chemistry A, 2015. **3**(32): p. 16824-16830.

138. Yang, Y., et al., *Carbon dots supported upon N-doped TiO 2 nanorods applied into sodium and lithium ion batteries.* Journal of Materials Chemistry A, 2015. **3**(10): p. 5648-5655.

139. Chastain, J. and R.C. King Jr, *Handbook of X-ray photoelectron spectroscopy.* Perkin-Elmer Corporation, 1992. **40**: p. 221.

140. Inkson, B., *Scanning electron microscopy (SEM) and transmission electron microscopy (TEM) for materials characterization*, in *Materials characterization using nondestructive evaluation (NDE) methods*. 2016, Elsevier. p. 17-43.

141. Pavia, D.L., et al., *Infrared Spectroscopy.* Introduction to spectroscopy, 2016.

142. Ţucureanu, V., A. Matei, and A.M. Avram, *FTIR spectroscopy for carbon family study.* Critical reviews in analytical chemistry, 2016. **46**(6): p. 502-520.

143. Guerrero-Pérez, M.O. and G.S. Patience, *Experimental methods in chemical engineering: Fourier transform infrared spectroscopy—FTIR.* The Canadian Journal of Chemical Engineering, 2020. **98**(1): p. 25-33.

144. Berthomieu, C. and R. Hienerwadel, *Fourier transform infrared (FTIR) spectroscopy.* Photosynthesis research, 2009. **101**(2): p. 157-170.

145. Birkner, N. and Q. Wang, *How an FTIR Spectrometer Operates.* UC Davis ChemWiki, 2014.

146. Franken, L.E., et al., *A Technical Introduction to Transmission Electron Microscopy for Soft-Matter: Imaging, Possibilities, Choices, and Technical Developments.* Small, 2020. **16**(14): p. 1906198.

147. Kaech, A., *An introduction to electron microscopy instrumentation, imaging and preparation.* Center for Microscopy and Image Analysis, University of Zurich, 2013.

148. Albani, J.R., *Principles and applications of fluorescence spectroscopy*. 2008: John Wiley & Sons.

149. Jameson, D.M., *Introduction to fluorescence*. 2014: Taylor & Francis.

150. Valeur, B. and M.N. Berberan-Santos, *Molecular fluorescence: principles and applications*. 2012: John Wiley & Sons.

151. Lakowicz, J.R., *Principles of fluorescence spectroscopy*. 2013: Springer science & business media.

152. SEYBOLD, P.G., M. GOUTERMAN, and J. CALLIS, *Calorimetric, photometric and lifetime determinations of fluorescence yields of fluorescein dyes.* Photochemistry and photobiology, 1969. **9**(3): p. 229-242.

153. Wahl, M., *Technical Note on Time-Correlated Single Photon Counting.* PicoQuant GmbH, 2014.

154. Stojilovic, N., *Why can't we see hydrogen in X-ray photoelectron spectroscopy?* Journal of Chemical Education, 2012. **89**(10): p. 1331-1332.

155. Science, A., *CasaXPS User's Manual*. 2001, Casa Software Ltd.

156. Li, L. and T. Dong, *Photoluminescence tuning in carbon dots: Surface passivation or/and functionalization, heteroatom doping.* Journal of Materials Chemistry C, 2018. **6**(30): p. 7944-7970.

157. Wang, S., et al., *The dual roles of functional groups in the photoluminescence of graphene quantum dots.* Nanoscale, 2016. **8**(14): p. 7449-7458.

158. Wen, X., et al., *Intrinsic and Extrinsic Fluorescence in Carbon Nanodots: Ultrafast Time-Resolved Fluorescence and Carrier Dynamics.* Advanced Optical Materials, 2013. **1**(2): p. 173-178.

159. Jin, Z., et al., *Large-scale growth and characterizations of nitrogen-doped monolayer graphene sheets.* Acs Nano, 2011. **5**(5): p. 4112-4117.